AD-A202 998

④

RADC-TR-87-284
Interim Report
July 1988

SPECTRAL CHARACTERISTICS OF HIGH FREQUENCY (HF) BACKSCATTER FOR HIGH LATITUDE IONOSPHERIC IRREGULARITIES: PRELIMINARY ANALYSIS OF STATISTICAL PROPERTIES

Johns Hopkins University

K. B. Baker, R. A. Greenwald, J. P. Villain and S. Wing

APPROVED FOR PUBLIC RELEASE; DISTRIBUTION UNLIMITED.

ROME AIR DEVELOPMENT CENTER
Air Force Systems Command
Griffiss Air Force Base, NY 13441-5700

88 12 5 079

AD A202998

REPORT DOCUMENTATION PAGE

Form Approved
OMB No. 0704-0188

1a. REPORT SECURITY CLASSIFICATION	1b. RESTRICTIVE MARKINGS
UNCLASSIFIED	N/A

2a. SECURITY CLASSIFICATION AUTHORITY	3. DISTRIBUTION / AVAILABILITY OF REPORT
N/A	Approved for public release;
2b. DECLASSIFICATION / DOWNGRADING SCHEDULE	distribution unlimited.
N/A	

4. PERFORMING ORGANIZATION REPORT NUMBER(S)	5. MONITORING ORGANIZATION REPORT NUMBER(S)
N/A	RADC-TR-87-284

6a. NAME OF PERFORMING ORGANIZATION	6b. OFFICE SYMBOL (If applicable)	7a. NAME OF MONITORING ORGANIZATION
Johns Hopkins University		Rome Air Development Center (EECP)

6c. ADDRESS (City, State, and ZIP Code)	7b. ADDRESS (City, State, and ZIP Code)
Applied Physics Laboratory Laurel MD 20707	Hanscom AFB MA 01731-5000

8a. NAME OF FUNDING / SPONSORING ORGANIZATION	8b. OFFICE SYMBOL (If applicable)	9. PROCUREMENT INSTRUMENT IDENTIFICATION NUMBER
Rome Air Development Center	EECP	00039-87-C-5301 (MIPR to SPAWAR)

8c. ADDRESS (City, State, and ZIP Code)	10. SOURCE OF FUNDING NUMBERS			
	PROGRAM ELEMENT NO.	PROJECT NO.	TASK NO	WORK UNIT ACCESSION NO.
Hanscom AFB MA 01731-5000	12417F	4600	16	69

11. TITLE (Include Security Classification)
SPECTRAL CHARACTERISTICS OF HIGH FREQUENCY (HF) BACKSCATTER FOR HIGH
LATITUDE IONOSPHERIC IRREGULARITIES: PRELIMINARY ANALYSIS OF STATISTICAL PROPERTIES

12. PERSONAL AUTHOR(S)
K.B. Baker, R.A. Greenwald, J.P. Villain, S. Wing

13a. TYPE OF REPORT	13b. TIME COVERED	14. DATE OF REPORT (Year, Month, Day)	15. PAGE COUNT
Interim	FROM Jul 84 TO Aug 86	July 1988	104

16. SUPPLEMENTARY NOTATION
N/A

17.	COSATI CODES		18. SUBJECT TERMS (Continue on reverse if necessary and identify by block number)
FIELD	GROUP	SUB-GROUP	OTH Doppler spectral characteristics
20	14		Backscatter HF backscatter radar
17	09		Ionospheric clutter —

19. ABSTRACT (Continue on reverse if necessary and identify by block number)
OTH-B radar signals backscattered from ionospheric irregularities can be very intense, and
any effort to mitigate against their influence requires knowledge of at least the Doppler
shift and spread that they introduce in the backscattered signals. This report presents the
Doppler spectral characteristics of HF signals backscattered from F-region ionospheric
irregularities at high latitudes. The report will show that the variability in spread of the
Doppler returns make it difficult to discriminate against ionospheric clutter by Doppler
techniques alone.

The data presented have been obtained with the Johns Hopkins University/Applied Physics
Laboratory (APL) HF radar located at Goose Bay, Labrador. This is an auroral site and signals
from the radar are subjected to ionospheric clutter from magnetic-field-aligned irregularities
at high latitudes.

The report discusses the various procedures that may be used for spectral and/or (over)

20. DISTRIBUTION / AVAILABILITY OF ABSTRACT	21. ABSTRACT SECURITY CLASSIFICATION
☐ UNCLASSIFIED/UNLIMITED ☑ SAME AS RPT ☐ DTIC USERS	UNCLASSIFIED
22a. NAME OF RESPONSIBLE INDIVIDUAL	22b. TELEPHONE (Include Area Code)	22c. OFFICE SYMBOL
Bertus Weijers	(617) 377-2527	RADC (EECP)

DD Form 1473, JUN 86   Previous editions are obsolete.   SECURITY CLASSIFICATION OF THIS PAGE

Block 19. Abstract (Cont'd)

autocorrelation analysis of backscattered radar signals, the method by which these auto-
correlation functions are obtained to remove contributions from ground backscatter and
unwanted signal sources. The autocorrelation functions are analyzed to determine their
decorrelation time and finally, the parameters are converted to Doppler velocity width
and shift.

Accession For		
NTIS GRA&I	☒	
DTIC TAB	☐	
Unannounced	☐	
Justification		
By		
Distribution/		
Availability Codes		
Dist	Avail and/or Special	
A-1		

TABLE OF CONTENTS

1.0 INTRODUCTION

Long range target detection via ionospheric propagation modes --
commonly known as over-the-horizon (OTH) detection -- has long been considered
as a means of extending radar coverage to large distances. Many experimental
studies have been conducted over the years and at the present time operational
systems are under development. This mode of detection possesses several dis-
tinct advantages including an ability to detect targets to distances in excess
of 3000 km. However, it also suffers from shortcomings which have tended to
retard its development. Among these are the fact that ionospheric propagation
modes require the frequency of operation to be less than approximately three
times the ionospheric critical frequency -- ~ 10 MHz -- leading to a somewhat
complex propagation analysis for precise target location. The problem is
especially severe at high latitudes where the ionosphere is highly-variable as
a result of auroral particle precipitation. In addition, particle precipita-
tion may produce enhanced ionization of the D-region of the ionosphere which
can lead to severe absorption of the energy in ionospheric propagation modes
and an associated reduction in the radar sensitivity. Finally, radars utili-
zing ionospheric propagation paths are especially sensitive to ionospheric
clutter from magnetic-field-aligned electron density irregularities. Radar
signals backscattered from these irregularities can be very intense and any
effort to mitigate against their influence requires knowledge of at least the
Doppler shift and spread that they introduce in the backscattered signals.

In this report we concentrate on the third of these problems associ-
ated with OTH detection. Our knowledge of the Doppler spectral characteris-
tics of HF signals backscattered from ionospheric irregularities has, in
general, been quite poor. This has been especially true for backscatter from
F-region irregularities at high latitudes. While experimental studies at high

- 1 -

latitudes have been conducted the equipment has often been designed for OTH detection and not for an analysis of the spectral characteristics of ionospheric irregularities. Consequently, when Elkins (1980) produced a model for HF radar auroral clutter, he was forced to assume certain spectral properties for the signals backscattered from high latitude irregularities. We shall show in this report that these assumptions were of limited validity. In particular, we shall show that the variability in the magnitude and direction of the irregularity drift as well as the variability in spread of the Doppler returns make it difficult to discriminate against ionospheric clutter by Doppler techniques, alone.

The data presented in this report have been obtained with The Johns Hopkins University/Applied Physics Laboratory (APL) HF Radar located at the Air Force Geophysics Laboratory High Latitude Ionospheric Observatory in Goose Bay, Labrador. This is an auroral zone site and signals from the radar are subjected to all of the detrimental ionospheric effects described in the previous paragraphs. The radar was initially funded by the Atmospheric Sciences Division of the National Science Foundation and by the Atmospheric and Chemical Sciences Directorate of the Air Force Office of Scientific Research for the study of small-scale ionospheric irregularity structure. Subsequently, additional support, including a second receiving array for the antenna system, have been provided by the Electromagnetic Propagation Branch of Rome Air Development Center and by the Ionospheric Effects Division of the Defense Nuclear Agency. At the present time the radar is operating at a modest power level that is approximately 30 dB below that required for OTH detection. Improvements presently being made to the radar will increase the sensitivity by approximately 10 dB.

Since the APL radar was developed for the investigation of small-scale ionospheric structure, it has several capabilities that differentiate it from radar systems that have been utilized for OTH detection. Most notable of these is an unusual multipulse transmission pattern that yields unambiguous determinations of the autocorrelation functions of the backscattered signals as a function of range. The autocorrelation functions are calculated in real time by an on-line microcomputer and stored on digital tape. Subsequent processing at APL yields Doppler spectra of the backscattered signals. The approach as it is implemented on the radar provides for a Doppler bandwidth of 330 Hz about the transmitted frequency. At an operating frequency of 10 MHz, this bandwidth yields unambiguous line-of-sight velocity measurements up to nearly 2500 m/s.

In the following we present, first, a discussion of various procedures that one might use for spectral and/or autocorrelation analysis of backscattered radar signals. This discussion is derived from a similar analysis presented in an earlier RADC report (Greenwald, 1982). Next, we describe the method by which the autocorrelation functions obtained by the radar are processed at APL in order to remove contributions from ground backscatter and unwanted signal sources. The autocorrelation functions are then analyzed to determine their decorrelation time (inverse of the spectral bandwidth) and their period (inverse of the Doppler frequency). Finally, the parameters are converted to Doppler velocity width and shift through inversion and correction for frequency of operation. These values have been used in a statistical study of the occurrence and Doppler characteristics of backscatter from high latitude ionospheric irregularities. The results from this analysis are then discussed in terms of their implications on the operation of OTH radars in high latitude environments.

2.0 TECHNIQUES FOR DOPPLER ANALYSIS OF IONOSPHERIC CLUTTER

Small-scale ionospheric structure falls within a class of scatterer that is known as a distributed soft target. This type of scatterer often has a rather small volume scattering cross-section, often $10^{-10} - 10^{-14}$ m^2/m^3; however, as the total scattering volume may be quite large, for example 10^{13} m^3, the signals backscattered from the volume may be appreciable. The volume scattering cross-section associated with soft targets is determined from Fourier decomposition of the medium. Since the radar signals undergo Bragg scattering by the irregularities, the critical Fourier component is given by $k = k_{inc} - k_{scat}$. In the case of a backscatter radar, k_{inc} and k_{scat} are equal and oppositely directed; hence the Fourier component of interest has a wavelength that is equal to half the radar wavelength. The amplitude of this critical Fourier component is determined by the physical processes occurring in the medium. Examples of how it is obtained are given by Farley (1972) and in the case of HF backscatter by Walker et al. (1986). A detailed discussion of irregularity scattering cross-sections is beyond the scope of this report.

Let us now consider the phase variations of a signal backscattered from a given volume of ionospheric irregularities. If one compares the back-scattered signal with a reference oscillator operating at the frequency of the transmitted signal, the phase difference between the two signals will vary with time. This phase variation is the Doppler effect due to the bulk motion of the scattering volume. In addition, one will note that the difference signal randomizes or loses phase memory after a relatively short time. This time is the decorrelation time of the medium and it transforms to the width of the Doppler spectrum (see Section 3.2). Precisely stated, the decorrelation time is related to the decay of the two-point time-dependent cross-correlation function of the process producing the irregularity structures. Physically, it

may be thought of as due to the finite lifetimes of the individual irregularity structures and the random or turbulent velocities that exist in the scattering volume.

The question arises as to how one might analyze the signals returned from the scattering volume. In this report we consider four different approaches using pulsed transmissions (These as well as fm-cw transmissions have been discussed in an earlier report by Greenwald (1982)). The approaches have been selected so as to demonstrate that increasingly complex procedures will enable one to obtain unambiguous information from increasingly complex situations. The four approaches are:

1) long pulse,

2) repetitive pulse,

3) variable lag double pulse, and

4) multiple pulse.

We consider each of these pulse modes as they are implemented for HF radar systems. We shall assume that ionospheric backscatter may occur simultaneously over a range interval of 1500 km (10 ms in radar group delay), that it can exhibit Doppler shifts in excess of 1200 m/s (100 Hz at 12.5 MHz) and that it has a typical decorrelation time of 30 ms.

2.1   Long Pulse

Doppler analysis of the signals scattered from a single long transmitted pulse is performed as shown in Figure 1a. For this transmission mode the length of the transmitted pulse should approximate the decorrelation time of the medium. Hence we assume it to have a width of 30 ms. The signals

- 5 -

scattered by the ionospheric structure are assumed to be referenced to the transmission frequency by passing them through a phase coherent receiver. The quadrature outputs of the receiver contain the desired Doppler information. In order to obtain the desired spectral bandwidth the receiver must have a bandwidth of at least 100 Hz and its outputs must be sampled at twice that rate. The sampled data forms a time series which may be denoted as

$$C(j) = A(j) + iB(j) \qquad 1 \leq j \leq N \qquad (1)$$

where $A(j)$ and $B(j)$ represent the jth sample of the quadrature outputs of the receiver. This time series may be Fourier analyzed or it may be analyzed to yield the autocorrelation function of the backscattered signal. We shall determine the latter quantity to maintain uniformity between the various analysis procedures. It is given by

$$R(k) = \langle C(j)C^*(j+k) \rangle \qquad 1 \leq k \leq N-1 \qquad (2)$$

where the asterisk represents the complex conjugate. The Doppler spectrum associated with $R(k)$ may be obtained by Fourier transformation.

The disadvantage of the long pulse approach should be quite evident. Due to the length of the transmission, backscattered signals are received simultaneously from the entire 1500 km extent of the scattering region. Consequently, there is no way to resolve any range-dependent Doppler velocity structure that may be present.

2.2 Repetitive Pulse

In order to retain range-dependent Doppler information a somewhat more sophisticated pulse transmission technique is required. For example, it can be noted that the long pulse is transmitted for the entire length of the sampling sequence. This is not necessary and, in fact, one may replace the long transmission by a sequence of short transmitted pulses with one pulse preceding each sample of the received signal (See Figure 1b). With this pulse scheme, the bandwidth of the receiver is matched to the length of the transmitted pulse and the spatial resolution of the measurement is determined by the latter quantity. If the transmitted pulse were to have a typical length of 100 μs, then the range resolution would be 15 km.

With the repetitive pulse technique the sampled time series and the resulting autocorrelation function may be written as

$$C(t,j) = A(t,j) + iB(t,j) \qquad 1 < j < N \qquad (3)$$

and

$$R(t,k) = \langle C(t,j)C^*(t,j+k) \rangle \qquad 1 < k < N-1 \qquad (4)$$

respectively. Here, t represents the time delay between transmission of a pulse and sampling of the backscattered signal. Since the transmitted pulse length is short in comparison to the time between pulses (5 ms for a 200 Hz sampling frequency), it is entirely possible to analyze the backscattered signals from many different ranges, simultaneously.

Unfortunately, the repetitive pulse technique has a significant shortcoming. Initially, it had been assumed that the scattering region had a

range extent of 1500 km. For the present discussion we will assume it to extend from 1000 to 2500 km. If t is set so that the data is sampled at a range of 1000 km (t = 6.7 ms), then the sample will also be of signals back-scattered from the immediately preceding pulse due to ionospheric structure at a delay of 11.7 ms and a range of 1750 km. In fact, for every delay t that one might select there are two distinct ranges that can contribute to the backscattered signal. In practice the problem may be even more severe than demonstrated here since sampling frequencies in excess of 200 Hz may be required and scattering regions extended for more than 1500 km in range are entirely possible.

A particularly good example of the repetitive pulse technique as it is implemented at VHF frequencies for studies of the E-region radar aurora is given by Balsley and Ecklund (1972).

2.3   Variable-Lag Double Pulse

In order to avoid the problem of range ambiguity, while maintaining the requisite spectral bandwidth and resolution, it is necessary to utilize some non-repetitive multiple pulse technique. The simplest of these is the variable lag double pulse method (See Figure 1c). In this approach N pairs of pulses are transmitted with a spacing between pulses that is some multiple k of an elemental spacing T. The time between pulse pairs must be sufficiently long that no signals are received from the previous pulse pair while the data from the current pulse pair is being sampled. By referencing the time delay t to the time of the first pulse of a pulse pair, we can write the sampled returns from the transmissions as

$$C(t,j) = A(t,j) + iB(t,j) \qquad (5)$$

and

$$C(t+kT,j) = A(t+kT,j) + iB(t+kT,j) \qquad (6)$$

If we further allow the index k to be stepped through a range of values from 0 to M, we can write the autocorrelation function derived from this analysis procedure as

$$R(t,k) = <C(t,j)C^*(t+kT,j)> \qquad 0 \leq k \leq M \qquad (7)$$

Let us consider the application of the double pulse approach to backscatter from extended regions of ionospheric structure. If we denote the subscript 1 as indicating a response due to the first transmitted pulse and the subscript 2 as due to the second transmitted pulse, 7) can be rewritten as

$$R(t,k) = <(C_1(t,j)+C_2(t,j))(C_1^*(t+kT,j)+C_2^*(t+kT,j))> \qquad (8)$$

Now, by referencing the response of each transmitted pulse to the time of that pulse, explicitly noting the time delay between the two samples, and expanding the expectation value, (8) may be rewritten as

$$R(t,k) = <C_1(t,j,0)C_1^*(t+kT,j,k)>+<C_1(t,j,0)C_2^*(t,j,k)>$$

$$+ <C_2(t-kT,j,0)C_1^*(t+kT,j,k)>+<C_2(t-kT,j,0)C_2^*(t,j,k)>$$

$$0 \leq k \leq M \qquad (9)$$

Examination of (9) shows that only the second term on the right-hand-side involves a comparison of data from the same group delay. All other terms average to zero since the returns from two distinct ranges are uncorrelated. They contribute to the autocorrelation function only by raising the overall noise background of the measurement.

As in the case of the repetitive pulse, the variable lag double pulse method may be used for simultaneous examination of the Doppler characteristics of signals backscattered from many different ranges. Moveover, the elemental lag T and the number of lags M may be adjusted so that one can always perform a complete and correct Doppler analysis on the backscattered signals. Unfortunately, the method is very inefficient in terms of processing time. For the longer lags of the autocorrelation function one must wait for many tens of milliseconds to obtain the appropriate pulse separations. Since the lags are performed sequentially and N must be sufficiently large to obtain good statistics, it is highly questionable whether the high latitude ionosphere is sufficiently time stationary for this method to be used in the HF frequency regime. An example of its application to radar auroral backscatter at upper VHF frequencies is given by Nielsen et al.(1984).

2.4   Multipulse

It would be highly desirable to maintain the positive features of the double pulse technique while improving its efficiency. One might ask whether it is possible to transmit multiple pairs of double pulses with different lags in such a manner that the pulse pairs do not interfere with one another. This question has been answered in the affirmative and the solutions form the basis of multipulse transmission techniques (See Farley, 1972). With multipulse techniques one seeks to transmit a pattern of pulses such that the

pulse separations contain most or all of the lags necessary for determining the autocorrelation function of the backscattered signal and such that there is little or no ambiguity in the ranges that contribute to any given lag. In practice, a four pulse transmission pattern is the longest that can be used to obtain a full seven lag (counting the zero lag) autocorrelation function with no range ambiguity. Patterns with a greater number of pulses either have gaps in their associated autocorrelation patterns or they have range ambiguity for certain lags.

Farley (1972) has suggested several six-pulse patterns that might be used to determine fifteen lags of a 17-lag (counting the zero lag) autocorrelation function. For the Goose Bay radar, we have adopted a 7-pulse pattern, shown in Figure 1d, that is used to determine a full 17-lag autocorrelation function. This pattern exhibits range ambiguity for $k = 1, 2, 3,$ and 13; however, the large time separation between the two repetitions of $k = 1, 2,$ and 3, makes it extremely unlikely for two distinct range intervals to yield simultaneous backscattered signals. The remaining ambiguous lag is a problem. Either it can be dropped from the analysis or it can be ignored due to the small residual correlation that exists in the cross product analysis at these large lags.

In addition to retaining the benefits of the variable lag double pulse analysis, the multipulse technique is quite efficient from an analysis point of view. With it, the data for a full 17-lag autocorrelation function may be acquired in 16T. In contrast, at least 300T would be required to acquire the equivilent data using the variable lag double pulse technique. Thus, there is a speed enhancement of more than a factor of 18 in the data acquisition.

Some minor shortcomings of the multipulse approach are an increased noise background due to uncorrelated scatter from unwanted ranges and the occurrence of transmitter pulses at certain delays which affect the autocorrelation analysis. Fortunately, neither of these problems is particularly serious.

3.0   PROCESSING OF AUTOCORRELATION FUNCTIONS FROM THE GOOSE BAY RADAR

In the case of the APL Goose Bay radar, the analysis of the multipulse autocorrelation functions is carried out by a FORTRAN program, FITACF. This is a rather complex program, but its primary function is to fit a theoretical autocorrelation function to the observed data in order to determine the true backscattered power, the Doppler velocity, and the spectral width. Each 5 second integration is separately processed in two basic steps, Noise Reduction and Parameter fitting of each individual ACF.

3.1   Noise Reduction

There are several sources of noise which complicate the analysis of the radar data. The cosmic HF background noise is relatively constant in time but has a frequency dependence of the form $P \sim f^{(-5/2)}$. The multipulse technique, as noted above, causes strong scatter at some ranges to contribute to the noise level at other ranges. In addition, there are local sources of HF noise produced by nearby equipment, as well as the inherent noise of the receiver and digitizers. Finally, in the HF frequency band, there are nearly always remote radio transmitters that contribute to the noise background at varying intensity levels. Some of these transmitters are nearly CW sources while others are highly modulated or pulsed.

The first stage of the noise reduction process is the determination
of the basic noise level and the "noise ACF." An initial noise level is
determined from the average backscattered lag-0 power from the 10 weakest
ranges. An average noise ACF is then formed from all the autocorrelation
functions which have lag-0 power less than 1 dB above the initial estimate of
the noise level. In a typical case where there are no external transmitters
producing noise, the noise ACF will have a non-zero power at lag-0 and be
nearly zero for all other lags. If a CW transmitter is present, however, it
will be present at all range gates. In this case, the noise ACF will show a
clear non-zero frequency. In either case, the noise ACF is then subtracted
from the raw ACFs. This subtraction removes the excess lag-0 power due to
pure random noise and may also remove or substantially reduce the effect of
other coherent noise sources such as CW transmitters.

To see the effect of removing the noise ACF more clearly, let us
consider what the combination of two separate sources produces for an auto-
correlation function. For simplicity we shall assume each source is perfectly
correlated with itself, but is not correlated with the other source. This
will be the case when one source is an external transmitter and the other is a
backscattered ionospheric signal with a very narrow Doppler spectrum. In such
a case the autocorrelation function produced by a single transmission of the
multipulse sequence will be

$$A^2 e^{i\omega_1 t} + AB e^{i(\omega_1 - \omega_2)t} e^{i\phi} + B^2 e^{i\omega_2 t} \qquad (10)$$

where ϕ is an arbitrary phase. When many pulse sequences are added up, the
cross-term will tend to die out since the phase is different each time. The
expected result is

$$A^2 e^{i\omega_1 t} + B^2 e^{i\omega_2 t} + \frac{AB}{\sqrt{N}} e^{i(\omega_1 - \omega_2)t} e^{i\phi} \tag{11}$$

where N is the number of pulse sequences produced during the 5 second integration. The value of N is typically around 60 and hence the cross term is suppressed by a factor of 7.7. Let us assume that the A^2 term is a noise transmitter and the B^2 term is the ionospheric signal. If A > B then on subtracting the A^2 term (the noise ACF) from the total ACF we are left with

$$B^2 e^{i\omega_2 t} + \frac{AB}{\sqrt{N}} e^{i(\omega_1 - \omega_2)t} e^{i\phi} \tag{12}$$

If we are to be able to extract the true ionospheric ACF from the remaining noise we must have

$$B^2 > \frac{AB}{\sqrt{N}} \tag{13}$$

In terms of power this may be rewritten as

$$\frac{A^2}{B^2} < N \tag{14}$$

For our case, where N = 60 this implies that the ionospheric signal can be detected and extracted from the noise even when it is 17 dB below the noise. Of course this is an ideal case and still requires an ionospheric signal larger than the true random noise present which in actual practice limits the usefulness of this technique to cases where the noise source and the ionospheric signal are comparable.

3.2   Parameter Fitting

Once the noise ACF has been removed from the data, it is possible to fit an assumed functional form to each of the ACFs. We have looked at two possible functional forms, an exponential decorrelation with time and a Gaussian decorrelation. If we assume an exponential decorrelation we will have

$$R_\lambda(t) = C_\lambda \, e^{i\omega t} \, e^{-\lambda t} \tag{15}$$

where C_λ is the power, ω is the Doppler frequency and λ is the decorrelation parameter. The Fourier transform of R_λ gives a Doppler spectrum of the form

$$S_\lambda(\omega') = \frac{2\lambda}{\lambda^2 + (\omega-\omega')^2} \tag{16}$$

which peaks at $\omega' = \omega$ and has a full width at half-maximum of 2λ radians/s. Alternatively, if we assume a Gaussian decorrelation we will have

$$R_\sigma(t) = C_\sigma \, e^{i\omega t} \, e^{-\sigma^2 t^2} \tag{17}$$

and the Doppler spectrum will be

$$S_\sigma(\omega^1) = \frac{\sqrt{\pi}}{\sigma} C_\sigma \, e^{\frac{-(\omega-\omega')^2}{4\sigma^2}} \tag{18}$$

which again peaks at $\omega' = \omega$ and has a width of $4\,\sigma\,\sqrt{\ln(2)} = 2.76\,\sigma$. The parameters C_λ, λ, ω or C_σ, σ, ω are fitted using a power-weighted least-squares fit. Weighting by the power emphasizes the importance of the earlier lags where the power is greater and the errors and influence of noise are less. The Doppler frequency is found by doing a least-squares fit to the

observed phase at each lag (Hanuise et al., 1985), while the decorrelation parameter and power (C_λ and λ or C_σ and σ) are found by doing a fit to the logarithm of the magnitude of the observed ACF.

There are several complications in doing the fit that must be considered. The primary difficulty is the problem of "bad lags". Since some samples are taken at the same time that the transmitter is on and the receiver is off, a range which uses one of these samples in computing its ACF will have one or more lags which are bad and should not be used in the fitting process. In addition to lags which are bad because of transmitter pulses, lag-13 has multiple redundancy in the multipulse sequence and can lead to range-aliased results. Finally, pulsed signals from remote signal sources can cause sudden changes in the received signal which affect only a few samples. The noise from these pulsed sources cannot be removed by the method described in the previous section, and each lag which uses one of the affected samples will be a bad lag.

The first step in performing the fit to the observed data is therefore to detect bad lags and eliminate them from the data used for the fit. The samples which are taken during transmitter pulses are readily determined and removed from the autocorrelation function analysis. In addition, because of the range aliasing problem, lag-13 for all ranges is considered a bad lag. The remaining lags are scanned and any lag which shows a large increase in magnitude over the preceding lags is considered a bad lag.

Once the bad lags have been removed the remaining lags are used to determine the parameter fit. Although the determination of C and λ (or C and σ) is straightforward, there is one additional complication in determining the Doppler frequency. To do a straight line fit to the phase we assume that the phase is either monotonically increasing or decreasing (or approaching

receding Doppler velocities). The actual measured phase, however, is confined to the range $\pm \pi$. Multiples of 2π must therefore be added to the observed phase at the higher lags. The basic approach used is described by Hanuise, et al. (1985), but it has been modified to improve the determination of the 2π folding factor in cases where several lags are bad and cannot be used. In addition, the error in determining ω is estimated and used to determine the velocity error.

The question of which of the two functional forms for the ACF (Equations 15 and 17) is the more appropriate one to use is difficult to determine. If the decorrelation is due to the fact that we are observing multiple scatterers in the presence of velocity turbulence, then we would expect the Doppler spectrum to be Gaussian and Equations (17) and (18) to be the more appropriate ones. If, on the other hand, the decorrelation is due to the growth and decay of the plasma irregularity structures with little or no velocity turbulence, then the appropriate equations are (15) and (16).

To investigate this further, we have tried both fits on several different periods of data. An example is shown in Figure 2. The data were taken on January 6,1986 at 20:01:40 UT (Figure 2a) and 20:01:45 UT (Figure 2b) for the same range (1080 km). Table 1 gives the values of the parameter fit for the two methods and the power weighted error for each.

TABLE 1

	20:01:40	20:01:45
$\log(C_\lambda)$	11.71	11.51
λ	48.89	43.11
ε_λ	0.042	0.022
width (λ)	97.8 rad/s	86.2 rad/s
$\log(C_\sigma)$	11.48	11.25
σ	38.56	31.51
ε_σ	0.007	0.039
width (σ)	106.81 rad/s	87.3 rad/s

For the first case (Figure 2a), the Gaussian fit is clearly superior, but the physical results, power and width, are not markedly different. In the second case (Figure 2b), the exponential fit has the smaller error, but again, the physical results are very similar. Since these two examples are from the same range and are separated by only five seconds, it is unlikely that the physical process responsible for the decorrelation could have changed greatly. We conclude that from the data currently available, it is nearly impossible to determine which decorrelation model is the "correct" one and the power and spectral width determined by either method are very similar. For this statistical survey, we have used the exponential fit represented by Equation (15).

3.3   Separation of Ground Scatter and Ionospheric Scatter

Once the parameter fit has been performed on an ACF, it is possible to separate ground scatter from ionospheric scatter. Ground scatter is characterized by a very low Doppler frequency and a very small decorrelation

parameter (i.e. large decorrelation time). After analyzing several hundred ACFs from many different periods we have determined a reasonable set of limits which define the spectra of ground backscattered signals:

1) Ground backscattered signals typically have $|\omega| < 18.85$ radians/s (3 Hz).

2) Ground backscattered signals have small $|\lambda|$. The actual limit depends on the power (C). As can be seen in Figure 3, weak ground scatter signals tend to have larger values of λ than strong signals. The limits we have used here are

$$|\lambda| < \begin{cases} 5 \; s^{-1} & \text{for SNR} > 6 \text{ dB} \\ (12\text{-SNR}) \; s^{-1} & \text{for } 0 < \text{SNR} < 6 \text{ dB} \\ 12 \; s^{-1} & \text{for SNR} < 0 \text{ dB} \end{cases}$$

With these choices for the limits defining ground scatter we find that we misidentify approximately 5-10% of weak ground scatter signals as being true ionospheric signals. Also, a small percentage of weak ionospheric signals, which have very low velocities are misidentified as ground scatter, but it is difficult to determine exactly what this percentage is. Strong signals (> 10 dB) are almost never misidentified.

If the ACF has been identified as due to ground scatter, the ground scatter function defined by C, ω and λ is subtracted from the data and the residual is re-analyzed. If a reasonable fit is found for the parameters of the residual (i. e. $|\omega| > 18.85$ and relative error < 1) the ACF is identified as a mixture of ground scatter plus ionospheric scatter.

4.0   STATISTICAL METHOD

4.1   Selection of the Data

In order to insure an unbiased sampling of the radar data, all the data available from July 1, 1984 to August 30, 1985 were divided into 1-hour sections. A random sample without replacement was then done to select 177 1-hour periods of data. From July 1984 to March 1985 the radar was being oper-ated in a mode which allowed us to collect only 4 hours of data per day. During some of this 7 month period the 4 hours were spread evenly over the entire day, taking only 10 minutes of data each hour. At other times, the data were taken continuously for 4 hours and the radar was not operated for the remainder of the day. Thus, the available data from the first seven months of this study were not uniformly distributed and this must be taken into account when we analyze the statistics. Starting in March 1985, new software was installed which allowed the radar to operate 24 hours a day, and the data from the final 6 months of this study are nearly uniformly distributed.

Once the data had been selected, they were divided into two cate-gories, scatter and no-scatter. A 1-hour period was assigned to the scatter category provided that there was at least 1 10-minute period within the data for which backscattered power was clearly present with a signal-to-noise ratio of 3 dB or more. If no such 10-minute period could be found, the 1-hour period was assigned to the no-scatter category. The 10-minute limit was required for two reasons; firstly, to limit the total amount of data we would have to process and, secondly, because there were many 1-hour periods when only 10 minutes of data were actually taken. It should be stressed, however, that our definition of the probability of observing scatter within a given

- 20 -

hour means the probability of observing at least 10 minutes of backscattered power at or above 3 dB during that hour.

Having determined which of the 1-hour periods show good backscattered power, we then selected 10 minutes of data from each period for more detailed analysis. In order to explain the techniques used in the remainder of the data analysis, it is first necessary to describe how the radar operates. A full description of the Goose Bay HF-Radar can be found in Greenwald, et al. (1984). The radar is a phased-array system which is electronically steerable in 16 beam directions. Data are taken for a single beam for an integration period of 5 seconds. A full scan of 16 beams thus takes 80 seconds. There are 50 non-overlapping range-gates, each gate being 30 km wide. For each 5 second integration the autocorrelation functions are analyzed by FITACF. The combined results of FITACF for all the data may then be used for further statistical study.

4.2   Event Analysis

The data from FITACF are first analyzed in terms of the "events". By "event" we mean all the data from one 10-minute selection of data. The events are put into a 4-dimensional contingency table, which is defined in Table 2. Tables of reduced dimension are produced by summing over one or more of the dimensions. A description of the computer program used to generate these tables is given in the appendix. An event is considered to be ionospheric if 25% or more of the autocorrelation functions which had power greater than the noise level (hereafter simply referred to as ACFs) fulfilled the criteria in FITACF to be considered ionospheric scatter. Similarly, an event is considered to be ground scatter if 25% or more of the ACFs fulfilled

the criteria to be considered ground scatter. If both conditions are met the event is categorized as "both". A similar definition is used in determining the scatter region. If 25% or more of the ACFs come from ranges between 300 and 600 km the event is considered to be E-region scatter. If 25% or more of the ACFs come from ranges 900 to 2100 km the event is considered to be F-region, if both conditions are met the event is described as "both" and if neither condition is met (i.e. the ACFs were primarily from the ranges between 600 and 900 km) the region is "undetermined". Although such definitions are meaningless for the ground scatter events the use of the "region" category does not cause a problem since the events which are strictly ground scatter events can be ignored when looking at lower dimensional contingency tables. The Kp bins are in integral values of Kp and thus, for example, bin 3 included Kp of 3-,3,3+.

TABLE 2

Definition of the "Event" Table

Quantity	# of bins	bin ranges
Time (UT)	4	0-6,6-12,12-18,18-24
Scatter Type	3	ionospheric, ground, both
Region	4	E, F, both, undetermined
Kp	10	0,1,2,3,4,5,6,7,8,unknown

After examining the data in terms of "events" we turn to the individual ACFs. First, the ACFs are divided into three groups, those that have ionospheric backscattered power above the noise level, those that have ground scatter power above the noise level, and those which show no power above the noise level. We found a total of 42,852 ACFs which were ionospheric

- 22 -

and 24,159 ACFs which were due to ground scatter. Of the 42,852 ionospheric ACFs, we found only 32 which also had a ground scatter component above the noise level. The ionospheric data were then put into a 6-dimensional contingency table, which is defined in Table 3.

TABLE 3

Definition of the "ACF" Contingency Table

Quantity	# of Bins	Bin Definition
Time (UT)	4	0-6,6-12,12-18,18-24
Range (km)	3	300-900, 900-1200, 1200-2100
Power (dB)	3	0-6, 6-12, 12-40
Velocity (m/s)	8	± (0-300), (300-600), (600-900), (900-2000)
Lamda (s^{-1})	4	0-25, 25-50, 50-75, >75
Kp	10	0,1,2,3,4,5,6,7,8,unknown

As with the "event" table, additional tables of reduced dimension are produced by summing over one or more dimensions. In addition to the contingency tables for the ACFs, scatter plots and distribution plots have been made for a variety of parameters.

4.3   Statistical Distribution of Irregularity Observations

As described in Sections 4.1 and 4.2, the first step of our statistical analysis has been to determine the probability of observing appreciable backscattered power. The selected 1-hour periods were divided into scatter or no-scatter categories and were binned by time into four 6-hour intervals, 0 - 6 UT, 6 - 12 UT, 12 - 18 UT, and 18 - 24 UT. The magnetic local time at Goose Bay is approximately 3 hours earlier than UT and these four time bins are

therefore approximately centered around magnetic midnight, dawn, noon and dusk. The results are summarized in Table 4 and Figure 4. The rows in Table 4 labeled "obs." give the actual number of cases observed for each time period, the rows labeled "expect" give the expectation values based on the marginal probabilities. The sum of (expected-observed)^2 /expected is the chi-square statistic. The value of $\chi^2/4$ (4 is the number of degrees of freedom) strongly indicates that there is a statistically significant time dependence. Overall, the probability of observing some kind of scatter (ionospheric or ground) is approximately 58% with the highest probability (84%) occurring in the local midnight sector and the smallest (29%) in the local noon sector. We next turn to the "event" statistics. In order to improve the statistics for the event table and ACF table we randomly selected an additional 23 periods of data that had some sort of backscattered power, thus bringing the total number of events to 125. The first table to consider is the 2-d table of scatter type vs time. Table 5 and Figure 5 show the distribution and chi-square test for this table. Although there was a strong time dependence on the overall probability of seeing some kind of scatter (Fig. 4), there is little dependence of the type of scatter on time. The chi-square test shows no significant deviation of the number of observed events from the expectation values.

If we look at the type of scatter as a function of Kp, however, quite a different picture emerges. Table 6 and Figure 6 show the distribution of events by scatter type and Kp. Clearly, ionospheric scatter as opposed to ground scatter increases as Kp increases. The chi-square test confirms the statistical significance of this result with over 99% confidence.

The next question is how the ionospheric scattering region is affected by time and Kp. Table 7 and Figure 7 show the distribution of the

events by region and time. Note that the events where the region could not be determined have been ignored. We find that ionospheric scatter from the F-region is much more likely in the time range from 12 to 24 UT (i.e. the local noon and dusk sectors). Conversely, E-region scatter is significantly more likely during the dawn (6-12 UT) sector. Table 8 and Figure 8 show the distribution of the events by region and Kp. Although Figure 8 seems to indicate a trend of increasing probability of E-region scatter with increasing Kp, this cannot be confirmed by the chi-square test. However, the chi-square test is not particularly sensitive to trends when there are many degrees of freedom. The probability of short wavelength E-region irregularities being formed is known to be related to the strength of the auroral electrojets which in turn are related (albeit weakly) to Kp. Thus, although the chi-square test cannot confirm the trend shown in Figure 7, the increase in the percent of E-region scatter with increasing Kp is not unexpected.

4.4 Statistical Distribution of Spectral Observations

We turn now to the results obtained from the individual spectra. First, as a check on the validity of the data analysis procedure of FITACF, we can compare the observed lag-0 backscattered power with the value obtained from the fit to the full autocorrelation function. When the backscattered power is due to ionospheric scatter these two quantities should be highly correlated. At low powers, however, we would expect the lag-0 power to be greater than the fitted power since the lag-0 power includes some residual noise as well as the ionospheric signal. As Figure 9 shows, the results are as expected. The points used are all the ACFs above 0 dB which were identified as ionospheric scatter, a total of 42,852 points. The analysis procedure of FITACF includes an error estimate in the velocity obtained from

the least-squares fit to the observed phase angle. Figure 10 shows the variation of the velocity error as a function of the lag-0 power (10a) and as a function of the fitted power (10b). We would expect larger velocity errors to occur at lower powers and this is indeed what we find when plotting the error vs the fitted power. However, the scatter plot obtained by plotting the error vs the lag-0 power shows a clear deviation from the expected distribution. Presumably, this is due to noise which increases both the lag-0 power and the velocity error. The consistency of the results using the fitted power leads us to conclude that the fitted power is the proper parameter to use in the remainder of our statistical analysis. The mean value of the Doppler velocity error for the data shown in Figure 10b is Δv = 104 m/s, while the standard deviation is $\sigma_{\Delta v}$ = 141 m/s. This provides a reasonable criterion for rejecting data based on the velocity error. A velocity error greater than 250 m/s is slightly more than 1-σ greater than the mean error and on a number of our scatter plots as well as the 6-dimensional contingency table, we have restricted the data to those points with velocity error less than 250 m/s. It would be improper to use a more restrictive limit on the velocity error because the error is correlated to the Doppler spectral width. Figure 11 shows a scatter plot of velocity error vs spectral width. It is clear that wide spectra tend to give rise to larger errors in estimating the mean Doppler velocity, but that is to be expected and the wide spectra are perfectly valid data. Thus, using too stringent a velocity error criterion for accepting data would result in the rejection of an excessive number of valid data having wide spectral characteristics.

In Figure 12 we plot the spectral width as a function of fitted power. The relation between the power and the velocity error (Figure 10) and the relation between spectral width and velocity error (Figure 11) necessarily

implies there should be a tendency to observe larger spectral widths at lower powers. Essentially, the increase in spectral width with the decrease in backscattered power is due to the increasing effect of noise in the analysis of the autocorrelation functions at lower powers. The expected inverse correlation between spectral width and power is clear in Figure 12, but the distribution shows the existence of larger spectral widths at all powers than the velocity error distribution in Figure 10b. The partial cut-off in the density of points in Figure 11 at low power and low width is due to the classification of many of these low power ACFs as coming from ground scatter.

We next turn to the question of the relation between ionospheric backscattered power and range. Walker, et al. (1986) have shown that the intensity of the backscattered power received by the Goose Bay radar is expected to be inversely proportional to the square of the distance for F-region scatter. For E-region scatter, the irregularities probably do not fill the beam and the backscattered power is expected to be more closely proportional to the cube of the distance. It must be noted, however, that these relations are complicated by a number of additional factors, most notably the vertical beam pattern of the antenna array. Figure 13 is a scatter plot of the backscattered power (i.e. fitted power from the ACFs) vs range. It is clear that the density of points shows a dependence on range and that the average power decreases with increasing range. For reference purposes we have also plotted an $1/r^3$ curve for the range 300 -600 km (where we expect the scatter to come from the E-region) and a $1/r^2$ curve for the range 1000 - 2100 km (where we expect the scatter to come from the F-region). The distribution of points in both regions is reasonably consistent with the expected dependence on distance. The region between 600 and 1000 km shows an unexpected excess of points with high power, but there are more

points at all powers for this region and it contains scatter from both the E-region and the F-region, which makes it difficult to interpret the density of points in this region. The excess of points at high power for the closest ranges (300 - 400 km) is probably due to the effects of the antenna beam pattern.

We now turn to the distributions involving the Doppler velocity. Figure 14a is a scatter plot of the velocity vs range for all the ACFs with errors below 250 m/s (and power > 0 dB). The most obvious feature is the enhanced density of points at 0 velocity. The most likely cause for this feature is weak groundscatter which, because the power was low, had larger than normal spectral widths and therefore were not identified as ground-scatter. Figure 14b shows the distribution for only the higher power ACFs (SNR > 10 dB). The enhanced density at 0 velocity is no longer present, but the rest of the distribution is qualitatively the same as Figure 13a, which strongly supports the speculation that the enhancement at 0 velocity was due to weak ground scatter.

In Figure 15a,b we again show the distribution of velocity vs range but now separated in terms of magnetic activity. The distribution for magnetically quiet times (Kp < 2-) clearly shows fewer high velocities than the distribution for magnetically active times (Kp > = 4-). This is particularly true at the closer ranges and indicates that this Kp dependence is significantly more important in the E-region than in the F-region.

Since the velocity distribution depends on the high-latitude convection patterns we expect the range vs velocity plots to vary with local time. Before examining this relationship, however, we must first consider how the geographic orientation of the Goose Bay radar affects the observations. The bore-sight of the radar points approximately 5 degrees east of geographic

north rather than toward the invariant pole or the magnetic pole. It is not entirely clear which pole best describes the plasma convection pattern at high latitudes. If we use the invariant pole (78.5° N, 291.0° E) the direction of the pole is approximately 9° W of the radar bore-sight direction. If we use an eccentric dipole (81.7° N, 271.8° E) the direction of the pole is about 13° W and if we use the magnetic dipole (76° N, 259° E) the direction of the pole is 38.6° W.

Figure 16a shows one model of the high latitude convection pattern appropriate for a southward pointing interplanetary magnetic field (Heelis, et al. 1980). Superimposed on the convection pattern is the radar field of view at 0, 6, 12, and 18 UT. In this view, the angle at the radar between the geographic and geomagnetic poles is taken to be approximately 13°. In the dusk time sector the plasma flow is primiarily perpendicular to the radar line of sight, but with a component that is toward the radar for most azimuths. Only the western-most azimuth will see a negative component. Thus there should be a bias toward positive velocities for the 18-24 UT period. In the dawn sector the situation is reversed. In the noon and midnight sectors the rotation of the plasma convection from sunward to anti-sunward (and vice-versa) should produce a strong bias toward negative velocities in the noon sector or a bias toward positive velocities for the midnight sector. In both cases, the rotation of the radar with respect to the magnetic pole reduces the bias from what would be expected in the symmetric case.

Figures 17a-d show the range vs velocity distributions for the four time sectors. The dawn and dusk distributions (17b,d) show the expected negative and positive velocity biases. Figure 17a, the distribution for the midnight sector, shows a relatively symmetric pattern with no evidence of a bias toward positive velocities. The orientation of the radar would tend to

decrease the positive bias for material coming out of the polar cap, but that is insufficient to explain these observations. One possible explanation for this discrepancy is that the convection pattern shown in Figure 16a does not include the effect of the Harang discontinuity nor does it include the effect of the interplanetary magnetic field on the size and orientation of the convection cells. Figure 16b shows a pattern (Heelis, 1980) which may be more typical. Some convection models (e.g. Heppner, 1984; Friis-Christensen, et al., 1985) show a consistent clockwise shift (for all values of B_y) of the basic convection pattern. As can be seen in Figure 16b, this has little effect on what the radar would observe in the dawn and dusk sectors, but could strongly affect what is observed in the noon and midnight sectors. The pattern in Figure 16b would tend to show a much more symmetrical Doppler velocity pattern around midnight. In addition, B_y effects would tend to shift the pattern around the pole. The combined effects may be sufficient to reduce the expected positive velocity bias to the point where the bias is no longer observable. Figure 17c shows the expected bias toward negative velocities but there are fewer events represented in this figure compared to 17a. Thus, although the velocity pattern is consistent with either Figures 16a or 16b, it cannot be taken as definitive support for either model.

Finally, we consider the type of velocity spectra observed. For the purpose of this study the parameter which characterizes a spectrum is the spectral width. As was pointed out in the discussion of Figure 12, there is an inverse relationship between the backscattered power and the spectral width. This relationship, however, is primarily due to the increased influence of noise at low powers. There remains a question whether there is a real physical relationship between the two quantities. Since it is likely that different instability mechanisms operate in the E- and F-regions, any

physical dependence of the spectral width on the backscattered power (and therefore on the fluctuation level of the ionospheric irregularities) might be expected to be different. We therefore examine the distribution of spectral width vs power for the E-region and F-region separately (Figures 18a,b) and, as can be seen, the two distributions are virtually identical.

It is well known that at VHF frequencies, the width of the spectra tend to be larger when the Doppler velocity is nearly zero. We therefore look at the distribution of spectral width vs Doppler velocity. Figures 19a,b show this distribution for the E-region and F-region. The most obvious feature is the two concentrations of points around ± 450 m/s in the E-region distribution (Figure 19a). These clusters of points also show a limited range of spectral widths from about 30 m/s to 125m/s. If these two E-region clusters are ignored the E- and F-region distributions are quite similar. In particular, the E-region distribution does not show an enhancement in comparison to the F-region in the number of spectra with large widths at nearly zero velocity. Both distributions show a greater number of spectra with large widths occurring at low velocities, but this is probably due to the fact that there are a greater number of points total at low velocities.

We next examine the spectral width as a function of magnetic activity (Kp). Figure 20a,b show the distribution of points in spectral width and range for quiet conditions (a) and disturbed conditions (b). In order to limit the problem of noise broadening the spectra, we have plotted only those points with power above 6 dB. At the higher ranges (F-region) the distributions for quiet and disturbed conditions are very similar, but at the low ranges (E-region) they are radically different. The E-region spectra under quiet conditions show very narrow Doppler spectra, with most of the points having spectral widths of less than 60 m/s. Conversely, under

disturbed conditions virtually all the spectra have widths in excess of 60m/s.

To get a clearer picture of the spectral width distributions we have made histograms of the frequency of occurrence of spectral width for the E- and F-regions (300-600 km, 900-2100 km) for quiet and disturbed periods. These distributions are shown in Figures 21a-d. As can be clearly seen, the E-region distributions are nearly complementary. A comparison of the E-region and F-region distributions for disturbed conditions shows a marked similarity between the two, although on average the F-region spectra are somewhat wider than the E-region spectra. In comparing the F-region distributions for quiet and disturbed conditions, we note that the quiet period distribution appears to consist of two components, a narrow component similar to the E-region distribution plus a broad spectrum component similar to the disturbed period distribution. One might speculate that in the F-region there are two different irregularity producing processes, one of which operates under all magnetic conditions and another which operates only under quiet conditions.

Another question that must be considered is whether or not the spectral widths vary as a function of local time. Since the results of the width variation with Kp showed distinct differences between the E-region and F-region behaviors, we will continue to separate the distributions by region. Figure 22a-d show the spectral width distributions for the 4 time sectors: midnight, dawn, noon, and dusk, in the E-region. There is no marked difference in these distributions. The 12-18 UT (noon) sector looks different, but there are very few points and they come primarily from a single event so the apparent difference is not statistically meaningful. Figure 23a-d show the spectral width distributions for the 4 time sectors in the F-region. Here there are very clear differences. In particular, the narrow spectra clearly come preferentially from the dusk and midnight sectors. In particular the

width distribution in the dusk sector (18-24 UT) shows a distinct absence of wide spectra compared to the other times. Combined with the results in Figures 21c,d this suggests that the narrow spectra are associated with the afternoon auroral zone F-region under quiet conditions. To further investigate this supposition we examine the F-region distributions for the 18-24 UT period separated into quiet and disturbed magnetic conditions. (Figure 24). The results are clear. The quiet period spectra are completely dominated by the narrow spectra while the disturbed period distribution shows very few narrow spectra. Indeed, the latter distributions are very similar to the results seen in the E-region distributions in Figure 21a,b.

5.0   DISCUSSION

5.1   High Latitude Convection Pattern

As was pointed out in section 4.3, the convection pattern in the dawn and dusk sectors are not highly sensitive to the IMF. However, the pattern at noon and midnight can depend very strongly on both the B_z and B_y components. For this reason a statistical survey, such as the one reported here, is much more likely to give coherent and consistent results for the dawn and dusk sectors than for the noon and midnight sectors. A great deal of modeling effort has been made to determine how the IMF affects the convection pattern (e.g. Heppner, 1977; Potemra et al., 1979; Heelis et al., 1980; Potemra et al., 1984; Zanetti et al., 1984; Heelis, 1984; Reiff and Burch, 1985; Friis-Christensen, 1985). The B_y component has two primary effects on the convection, a rotation about the magnetic pole and a change in the relative sizes of the two convection cells (e.g. Heelis et al., 1980, Potemra et al., 1979, Reiff and Burch, 1985). For some models the convection pattern

for negative B_y is the mirror image of the pattern for positive B_y (Burch et al. 1985; Reiff and Burch, 1985; Potemra et al., 1984; Zanetti et al., 1984). For others (Heppner, 1977; Friis-Christensen et al., 1985) this is not true. In addition, some models include a dependence on B_x (Heelis, 1984; Reiff and Burch, 1985). Recently, extensive efforts have been made using the Sondrestrom radar to observe the effects of the IMF on the high latitude convection pattern (de la Beaujardiere et al., 1985; de la Beaujardiere et al., 1986). They found that "the IMF B_y component strongly influences the night side polar convection" and that none of the models offer a very good match to the observations.

An additional complication results from what are known as UT effects. The precise details of the plasma convection depend not only on the magnetospheric processes which drive the convection, but on the ionospheric response as well. An important factor in the ionospheric response is the conductivity (both Hall and Pedersen), which is strongly influenced by the solar zenith angle and hence depend on season and local solar time (or UT) rather than the local magnetic time. Thus, the convection pattern seen at different geographic locations may show significant differences even when comparing identical magnetic local times and magnetic conditions.

The Goose Bay radar cannot usually see far enough into the polar cap to determine details about the convection across the cap. In particular, this means it is unlikely to be able to see the 3 or 4-cell patterns that have been suggested for northward B_z conditions. In general the Goose Bay radar results are compatible with the standard two-cell convection patterns. On a statistical basis the results near noon and midnight show less of the anti-sunward flow than might be expected, but when the complications of B_y effects and UT effects are included the results are not inconsistent with the various

convection models. Also specific event studies often yield Doppler measurements consistent with antisunward flow. A more detailed study will have to be made in the future in which the Goose Bay data can be separated by IMF conditions.

5.2   Spectral Characteristics

The observed Doppler spectra have a wide distribution of spectral widths. These widths range from nearly zero (i.e. no decorrelation of the ACF over the 50 ms multipulse duration) to over 1000 m/s. Overall there are no dramatic differences between the E-region and F-region spectra, but there are a few interesting differences. The E-region spectra appear to have a small additional population of spectra with velocities near the ion-acoustic velocity (~ $\pm$450 m/s). These spectra have widths from about 30 to 100 m/s. We also note that beyond Doppler velocities of about $\pm$ 500 m/s the number of E-region spectra decreases markedly, although spectra are observed with mean Doppler velocities as high as 2000 m/s. In contrast, the F-region distribution of the mean Doppler velocities shows a a more gradual decrease in occurrence at the higher velocities.

Another interesting class of spectra are found in the dusk sector during periods of low magnetic activity. These spectra have narrow widths (~ 50 m/s) and usually have Doppler velocities in the range from -300 to +300 m/s (although in some cases the velocities are over 500 m/s) They occur at ranges from 600 to 1800 km and are presumably from the F-region. Because of their similarity to the narrow spectra often observed in the E-region we must consider the possibility that these echoes come from a ground to F region to ground to E-region (and back) propagation mode and are in fact E-region irregularities. There is, however, no evidence in the cases studied for a

ground scatter signal equatorward of the ionospheric signal. In addition, it seems unlikely that such a complicated propagation mode would occur often. In this survey we have found these narrow spectra in 23 separate events, which supports the idea that these echoes are indeed from F-region irregularities. The limited range of Doppler velocities for these spectra is probably not significant, since these spectra occur only during quiet magnetic times when the ionospheric electric fields would tend to be low.

5.3 Implications for OTH Radar Systems

One thing that has become clear in this statistical survey is that nearly every variety of spectrum and Doppler velocity is possible. There is no single feature shared by all ionospheric clutter. Both very narrow and very wide spectra are found. Wide spectra can occur at high Doppler velocities as well as at very low Doppler velocities. In the latter case a single volume of space can simultaneously exhibit significant backscattered power at both positive and negative Doppler shifts. Thus an entire range of Doppler velocities from -500 to +500 m/s can be obscured by ionsopheric clutter. One cannot, however, avoid this problem simply by looking for targets with very narrow spectra, since ionospheric clutter with narrow spectra is also quite common.

Ionospheric clutter is particularly common during the late evening and night hours. Nevertheless, clutter may appear at any time. The best time for observing ground scatter is the period around local noon. However, even in the noon sector, over 80% of the scatter events we have observed were classified as ionospheric clutter or ionospheric clutter plus ground scatter. The probability of observing ionsopheric clutter is also dependent on magnetic activity and is much more likely to occur during disturbed

conditions. This also implies that ionospheric clutter will be more common during periods of high sunspot number. The present study only includes data taken near the sunspot minimum of the eleven year solar cycle. The amount of ionospheric clutter will probably be much greater near sunspot maximum.

6.0 REFERENCES

de la Beaujardiere, O., V. B. Wickwar and J. D. Kelly, Effect of the interplanetary magnetic field Y component on the high-latitude nightside convection, Geophys. Res. Lett., 12, 461, 1985.

de la Beaujardiere, O., V. B. Wickwar and J. H. King, Sondrestrom Radar observations of the effect of the IMF B_y component on polar cap convection, 1986.

Elkins, T. J., A model for high frequency radar auroral clutter, RADC-TR-80-122, 1980.

Farley, D. T., Multiple-pulse incoherent-scatter correlation function measurements, Radio Sci., 7, 661, 1972.

Friis-Christensen, E., Y. Kamide, A. D. Richmond, and S. Matsushita, Interplanetary magnetic field control of high-latitude electric fields and currents determined from Greenland magnetometer data, J. Geophys. Res., 90, 1325, 1985.

Greenwald, R. A., K. B. Baker, R. A. Hutchins, and C. Hanuise, An HF phased-array radar for studying small-scale structure in the high latitude ionosphere, Radio Sci., 20, 63, 1985.

Hanuise, C., R. A. Greenwald, and K. B. Baker, Drift motions of very high latitude F-region irregularities, J. Geophys. Res., 90, 9717, 1985.

Heelis, R. A. and W. B. Hanson, High-latitude ion convection in the nighttime F-region, J. Geophys. Res., 85, 1995, 1980.

Heelis, R. A., J. C. Foster, O. de la Beaujardiere and J. Holt, Multistation measurements of high-latitude ionospheric convection, J. Geophys. Res., 88, 10111, 1983.

Heppner, J. P., Empirical models of high-latitude electric fields, J. Geophys. Res., 82, 1115, 1977.

Heppner, J. P., Polar-cap electric field distributions related to the interplanetary magnetic field direction, J. Geophys. Res., 77, 4877, 1972.

Nielsen, E., C. I. Haldoupis, B. G. Fejer, and H. M. Ierkic, Dependence of auroral power spectra variations upon electron drift, J. Geophys. Res., 89, 253, 1984.

Potemra, T. A. ,L. J. Zanetti, P. F. Bythrow, and A. T. Y. Lui, B_y-dependent convection patterns during northward interplanetary magnetic field, J. Geophys. Res., 89, 9753, 1984.

Potemra, T. A., T. Iijima, and N. A. Saflekos, Large-scale characteristics of Birkeland currents, Dynamics of the Magnetosphere, 165, 1979.

Reiff, P. H. and J. L. Burch, IMF B_y-dependent plasma flow and Birkeland currents in the dayside magnetosphere. 2. A global model for northward and southward IMF, J. Geophys. Res., 90, 1595, 1985.

Walker, A. D. M., R. A. Greenwald, and K. B. Baker, Determination of the fluctuation level of ionospheric irregularities from radar backscatter measurements, Radio Sci., 1986.

FIGURE CAPTIONS

Figure 1.   A comparison of the different pulse techniques. (a) long pulse, (b) repetitive pulse, (c) variable lag double pulse, (d) multiple pulse.

Figure 2.   A comparison of the two types of least-squares fits to the power profile of the autocorrelation function (ACF). (a) An example in which the Gaussian fit is superior. (b) An example in which the exponential fit is superior. Note that (b) is the same range as (a) and only 5 seconds later in time.

Figure 3.   A comparison of the decorrelation parameter λ, for ionospheric backscatter and ground scatter.

Figure 4.   The probability of observing a backscattered signal 3 dB or more above the noise level for four time periods, 0-6 UT (local midnight sector), 6-12 UT (local dawn), 12-18 UT (local noon), and 18-24 (local dusk).

Figure 5.   Type of scatter as a function of time. For an event to be "ionospheric" at least 25% of the Doppler spectra (or ACFs) must be identified as ionospheric. For an event to be ground scatter at least 25% of the spectra must be identified as ground scatter.

Figure 6.   The type of scatter as a function of magnetic activity (as defined by the K_p index). Note that there are very few events with high K_p (> 4-).

Figure 7.   The probability of observing ionospheric scatter from the D-region and from the F-region as a function of time. An event is E-region scatter if at least 25% of the Doppler spectra came from ranges less than 600 km from the radar. An F-region event

is one in which at least 25% of the spectra come from ranges greater than 900 km. Events where the scatter cme primarily between 600 and 900 km could not be categorized.

Figure 8.   Probability of observing ionospheric scatter from the E-region and F-region as a function of K_p.

Figure 9.   Scatter plot of the fitted power (C) from the least-squares fit to the ACF vs. the lag-o power for the ACF.

Figure 10.   Scatter plot of the estimated error in the mean Doppler velocity vs. (a) the lag-o power of the ACF and (b) the fitted power.

Figure 11.   Scatter plot of the estimated error in the mean Doppler velocity vs. the spectral width (in m/s) as determined from the decorrelation parameter, λ.

Figure 12.   Scatter plot of the spectral width vs. the fitted power in the ACF. The sudden decrease in the density of points at low power and low width is due to the removal of spectra which were identified as ground scatter signals.

Figure 13.   Fitted power vs. range (in km) from the radar. For echoes from the thin E-region, the power should be inversely proportional to the cube of the distance. For the F-region, the power should be inversely proportional to the square of the distance.

Figure 14.   Scatter plot of the range (in km) vs. the mean Doppler velocity. (a) Scatter plot for all points with velocity error less than 250 m/s and signal-to-noise ration > 0 dB. (b) Scatter plot for only the points with velocity error < 250 m/s and SNR > 10 dB.

Figure 15.   Scatter plot of the Range vs. the mean Doppler velocity for (a) All points with velocity error < 250 m/s and K_p < 2- (magnetic quiet times) and (b) All points with velocity error < 250 m/s and $K_p \geq$ 4- (magnetically disturbed times).

Figure 16.   Examples of proposed convection patterns (Heelis and Hanson, 1980) in relation to the field-of-view of the Goose Bay radar. (a) Symmetric pattern for B_z < 0 and B_y = 0.   (b) Asymmetric pattern for B_z < 0 and $B_y \geq$ 0. Note that some convection models show a similar pattern independent of the sign of B_y.

Figure 17.   Range vs. velocity for all points with velocity error < 250 m/s and time in the (a) 0-6 UT range, (b) 6-12 UT range, (c) 12-18 UT range, and (d) 18-24 UT range.

Figure 18.   Spectral width vs. the fitted power for (a) The E-region (range 300-600 km) and (b) The F-region (range 900-2100 km).

Figure 19.   Spectral width vs. the mean Doppler velocity for (a) The E-region (300-600 km) and 9b) the F-region (900-2100 km).

Figure 20.   Spectral width vs. the Range for all spectra with signal-to-noise ration > 6 dB (to eliminate spectra which are broader than normal because the signal is weak) and velocity error < 250 m/s and (a) K_p < 2 (quiet periods) and (b) $K_p \geq$ 4- (disturbed periods).

Figure 21.   ~Spectral width distribution for all points with signal-to-noise ration > 6 dB and velocity error < 250 m/s and (a) E-region echoes (300-600 km) under quiet (K_p < 2-) conditions, (b) E-region echoes under disturbed ($K_p \geq$ 4-) conditions, (c) F-region echoes (900-2100 km) under quiet conditions, (d) F-region echoes under disturbed conditions.

Figure 22.   E-region spectral width distribution as a function of time. (a)
              0-6 UT (local midnight), (b) 6-12 (local dawn), (c) 12-18 UT
              (local noon), and (d) 18-24 UT (local dusk).

Figure 23.   F-region spectral width distribution as a function of time. (a)
              0-6 UT, (b) 6-12 UT, (c) 12-18 UT, and (d) 18-24 UT.

7.0   APPENDIX

The following is a brief description of the method to generate the 4 and 6 dimensional contingency tables described in sections 4.2 and 4.3.

In doing the statistical analysis of the radar data, it is necessary to write a computer program that will put n variables of the radar observations such as time, range, power, etc., into an n-dimensional histogram or array and then project this array to (n-1)-dimensional arrays and project the resulting arrays to (n-2)-dimensional arrays. This process will continue until everything is reduced to 1-dimensional array.

The program would be very simple and straight forward to write, if there were only 3 or fewer variables, thus using only arrays of 3-dimension or smaller. However, the program, if not carefully planned, could explode into pages and pages of do loops and write statements as more variables were added. This is because the number of arrays increases according to the recursive function numarray(n) = numarray(n-1) x 2 + 1, and numarray(1) = 1, where numarray is the number of arrays produced for an n-dimensional array. For example, in doing 4-dimensional array of time, region type, scatter type, and K_p (a magnetic disturbance index), we need the total of the following 15 arrays:

1   4-dimensional array of the above 4 variables

4   3-dimensional arrays (permutations of 3 out of the 4 variables)

6   2-dimensional arrays(permutations of 2 out of the 4 variables)

4   1-dimensional arrays

So, for 5-dimensional array, according to the formula there are 2(15)+1 = 31 arrays and for 6-dimensional array there are 2(31)+1 = 63 arrays.

Obviously it would be impractical to create 63 separate arrays for each of the permutations, sum them up and print them out. A clever algorithm

needs to be found for the program so that it is efficient, robust, concise and yet easy to change should there be a need to add or subtract variables/ dimension. The following describes such algorithm.

The above 4-dimensional array of time, region type, scatter type, and K_p, will serve as an example. These variables are called t, rt, st, and K_p respectively. Furthermore, the analysis calls for the time to be divided into 4 divisions, region type into 4, scatter type into 3, and K_p into 10. Thus, the histogram array could be declared in fortran as histo(4,4,3,10). The _simple_ method in getting all the 15 arrays would generate a fortran program that looks like the following:

```
    do t = 1,4
       do rt = 1,4
          do st = 1,3
             do kp = 1,10
c             begins listing the 15 histograms/arrays from
c             the fewest dimensions to the most dimension
              sum_t(t) = sum_t(t) + histo(t,rt,st,kp)
              sum_rt(t) = sum_rt(rt) + histo(t,rt,st,kp)
              sum_t_st(t,st) = sum_t_st(t,st) + histo(t,rt,st,kp)
              sum_t_rt_kp(t,rt,kp) = sum_t_rt_kp(t,rt,kp) + histo(t,rt,st,kp)
              <etc>
          end do
       end do
```

To print all the 15 histograms, the above codes will be repeated roughly 15 times and therefore will not be listed here.

The better alternative is to have one huge array which contains all the 15 arrays instead of 15 smaller ones. The idea is to have just one array that can be indexed properly such that it can be inserted in a few do-loops to give all the 15 arrays and therefore eliminates the need to enumerate explicitly each of the 15 individual arrays. (15 in this case, but it will grow to 63 for a 6 dimensional array and 127 for 7 dimensional array). This big array is declared as sum(0:4,0:4,0:10,15). Then,

sum_t(t) is replaced with sum(0,0,t,1).

sum_rt(rt) with sum(0,0,rt,2).

sum_t_st(t,st) with sum(0,t,st,7) etc.

Also, for reasons that will become clear later, t is equivalent to el(1), rt to el(2), st to el(3), kp to el(4), since t is the 1st element in the array histo, rt is 2nd etc. After doing all of the substitutions the listing of the above codes now looks like the following:

....

the first four do-loops of t,rt,st,and kp stay the same

......

sum(0,0,el(1),1) = sum(0,0,el(1),1) + histo(t,rt,st,kp) ....!sum_t

sum(0,0,el(2),2) = sum(0,0,el(2),2) + histo(t,rt,st,kp) ....!sum_rt

.

.

sum(0,el(1),el(3),7) = sum(0,el(1),el*3),7) + .histo(t,rt,st,kp) !sum_t_st

.

.

sum(el(1),el(2),el(4),15) = sum(el(1),el(2),el(4),15) + histo(t,rt,st,kp) !sum_t_rt_kp

The fourth index of the array sum is numbered from 1 to 15 for the 15 arrays so that each of the 15 has a unique number.

The next immediate step, which is the final step, is to find a way to generate the above list with do-loops. The key to doing that is to notice the first 3 indices of the array el go from 001, 002, 003, 004, 012, 013, all the way to 123, 124 and 234. The first index is always less than the second, and the second from the third, except when the index is zero. This pattern can be easily generated by 3 do loops as shown in the next few lines.

```
el(0) = 0
compindx = 0
do indx1 = 0,4
    do idx2 = indx1,4
        if(indx2.eq.0).or.(indx2.ne.indx1)) then
            do indx3 = indx2+1,4
             compindx = compindx + 1
             sum(el(indx1),el(indx2),el(indx3),compindx) =
             sum(el(indx1),el(indx2),el(indx3),compindx) +
             histo2(t,rt,st,kp)
            end do
        end if
    end do
end do
```

The algorithm to print the arrays looks similar to the above algorithm. It has the same number of do-loops and complexity. This algorithm will execute almost as fast as the simple algorithm. The only factor that can probably slow it down is the memory paging since the array sum can get big as

new variables are added. However, once the algorithm is understood, little modification to the algorithm will eliminate or reduce the problem, at the expense of the program being more difficult to follow. The complete listing of the subroutine output, which sums all the histograms and outputs them, is given below.

```
0001            subroutine output2
0002        c
0003        c   sum and output the 4-d histogram
0004        c   the histogram is located in the common block outdat
0005        c
0006            implicit none
0007            include 'outdat.par/list'
0008    1 c
0009    1 c   common for the output buffer and histogram
0010    1 c
0011    1       integer*2 histo1(10,4,3,8,3,4) !6d histogram containing
0012    1 c                 kp,w,p,v,r,t
0013    1       integer*2 histo2(4,4,3,10) ! 4d histogram
0014    1 c                 t,rt,st,kp
0015    1       integer*2 histognd(4,3,10)    ! ground scatter histogram
0016    1 c                 t,rt,kp
0017    1       equivalence (histo1,histo2)
0018    1       common/outdat/histo1,histognd
0019            integer*2 t,rt,st,kp ! indices of histo
0020            integer*2 indx1,indx2,indx3 ! indices to array el
0021            integer*2 el(0:4)/0,0,0,0,0/ ! indices to sum
0022            equivalence (el(1),t),(el(2),rt),(el(3),st),(el(4),kp)
0023            integer*2 sum(0:4,0:4,0:10,0:15) !the sum of all 15 histograms
0024            integer*2 compindx ! the 4th index of sum
0025            integer*2 nel(0:4)/1,4,4,3,10/ ! dimensions of histo(4,4,3,10)
0026            integer*2 i,j,k,l,m !
0027            character*5 col1(0:4)/' ','TIME','REGIO','SCATY','KP '/ ! label
0028            character*3 table(0:4)/' ','t-','rt-','st-','kp-'/ ! label for output
0029            character*8 col(0:10,4) ! more label
0030
0031        c   .
0032        c   initialize the labels
0033        c
0034        c
0035        c   used when index = 0 in array sum
0036        c
0037            col(0,1) = ' '
0038            col(0,2) = ' '
0039            col(0,3) = ' '
0040            col(0,4) = ' '
0041        c
0042        c   label for time
0043        c
0044            col(1,1) = '0-6'
0045            col(2,1) = '6-12'
0046            col(3,1) = '12-18'
0047            col(4,1) = '18-24'
0048        c
0049        c   label for region type
0050        c
0051            col(1,2) = 'E'
0052            col(2,2) = 'F'
0053            col(3,2) = 'E & F'
0054            col(4,2) = 'U'
0055        c
0056        c   label for scatter type
0057        c
```

```
0058                col(1,3) = 'IONOS'
0059                col(2,3) = 'GRND'
0060                col(3,3) = 'ION & GRND'
0061        c
0062        c       label for kp
0063        c
0064                col(1,4) = '0'
0065                col(2,4) = '1'
0066                col(3,4) = '2'
0067                col(4,4) = '3'
0068                col(5,4) = '4'
0069                col(6,4) = '5'
0070                col(7,4) = '6'
0071                col(8,4) = '7'
0072                col(9,4) = '8'
0073                col(10,4) = 'U'
0074
0075        c
0076        c       sum is initialized to 0 by default so there is no need to
0077        c       initialize it again
0078        c
0079        c
0080        c       sum the histogram
0081        c
0082                do t = 1,4
0083                   do rt = 1,4
0084                      do st = 1,3
0085                         do kp = 1,10
0086                            compindx = 0
0087                            do indx1 = 0,4
0088·                              do indx2 = indx1,4
0089                                  if((indx2.eq.0).or.(indx2.ne.indx1))then
0090                                     do indx3 = indx2+1,4
0091                                        compindx= compindx+1 ! increment index
0092        c
0093        c                             now do the summation
0094        c
0095                                        sum(el(indx1),el(indx2),el(indx3),
0096        #                               compindx) = sum(el(indx1),el(indx2),
0097        #                               el(indx3),compindx) + histo2(
0098        #                               t,rt,st,kp)
0099                                     end do
0100                                  end if
0101                               end do
0102                            end do
0103                         end do
0104                      end do
0105                   end do
0106                end do
0107        c
0108        c       print the sum histogram out
0109        c                  '
0110
0111                compindx = 0  ! initialize compindx to 0
0112                do indx1 = 0,4
0113                   do indx2 = indx1,4
0114                      if((indx2.eq.0).or.(indx2.ne.indx1)) then
```

```
0115                        do indx3 = indx2+1,4
0116                            compindx = compindx + 1 | increment the 4th index
0117    c
0118    c                     output what kind of histogram is being outputted
0119    c
0120                            write(2,90) table(indx1),table(indx2),table(indx3)
0121    90                      format('1',' histogram of',3a3)
0122                            do i = 1,nel(indx1)
0123                                if(indx1.ne.0)then
0124                                    el(indx1) = i
0125                                end if
0126    c
0127    c                         output the label of the outer index
0128    c
0129                                write(2,30) col1(indx1),col(el(indx1),indx1)
0130    30                          format('0',a5,a10)
0131    c
0132    c                         output the colum labels
0133    c
0134                                write(2,60) col1(indx3),(col(k,indx3),
0135         #                      k=1,nel(indx3))
0136    60                          format(t40,a5,/,t20,<nel(indx3)>a10)
0137                                do j = 1,nel(indx2)
0138                                    if(indx2.ne.0) then
0139                                        el(indx2) = j
0140                                    end if
0141    c
0142    c                             output the row labels and the content of histogram
0143    c
0144                                    write(2,10)col1(indx2),col(el(indx2),
0145         #                          indx2),(sum(el(indx1),el(indx2),k,compindx),
0146         #                          k = 1,nel(indx3))
0147    10                              format(1x,a5,a10,t18,<nel(indx3)>i10)
0148                                end do
0149                            end do
0150                        end do
0151                    end if
0152                end do
0153            end do
0154            return
0155            end
```
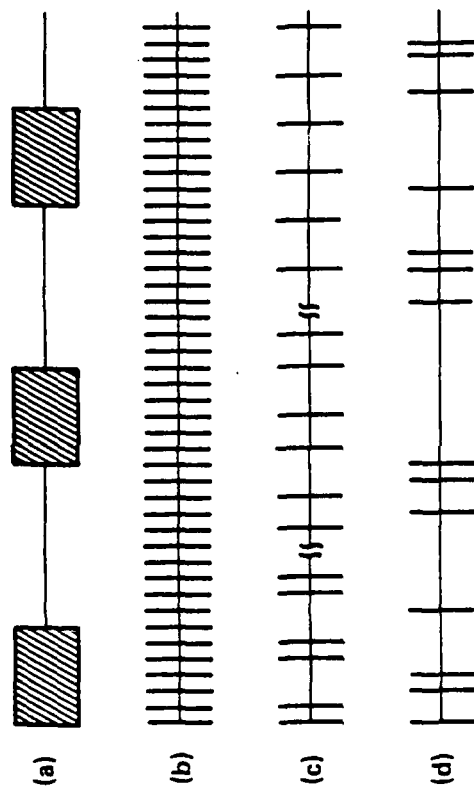
FIGURE 1

Comparison of Power Fits

1/6/86 20:01:40 range: 27

FIGURE 2a

Observed □   Exponential +   Gaussian ◇

Ln(power)

Lag Number
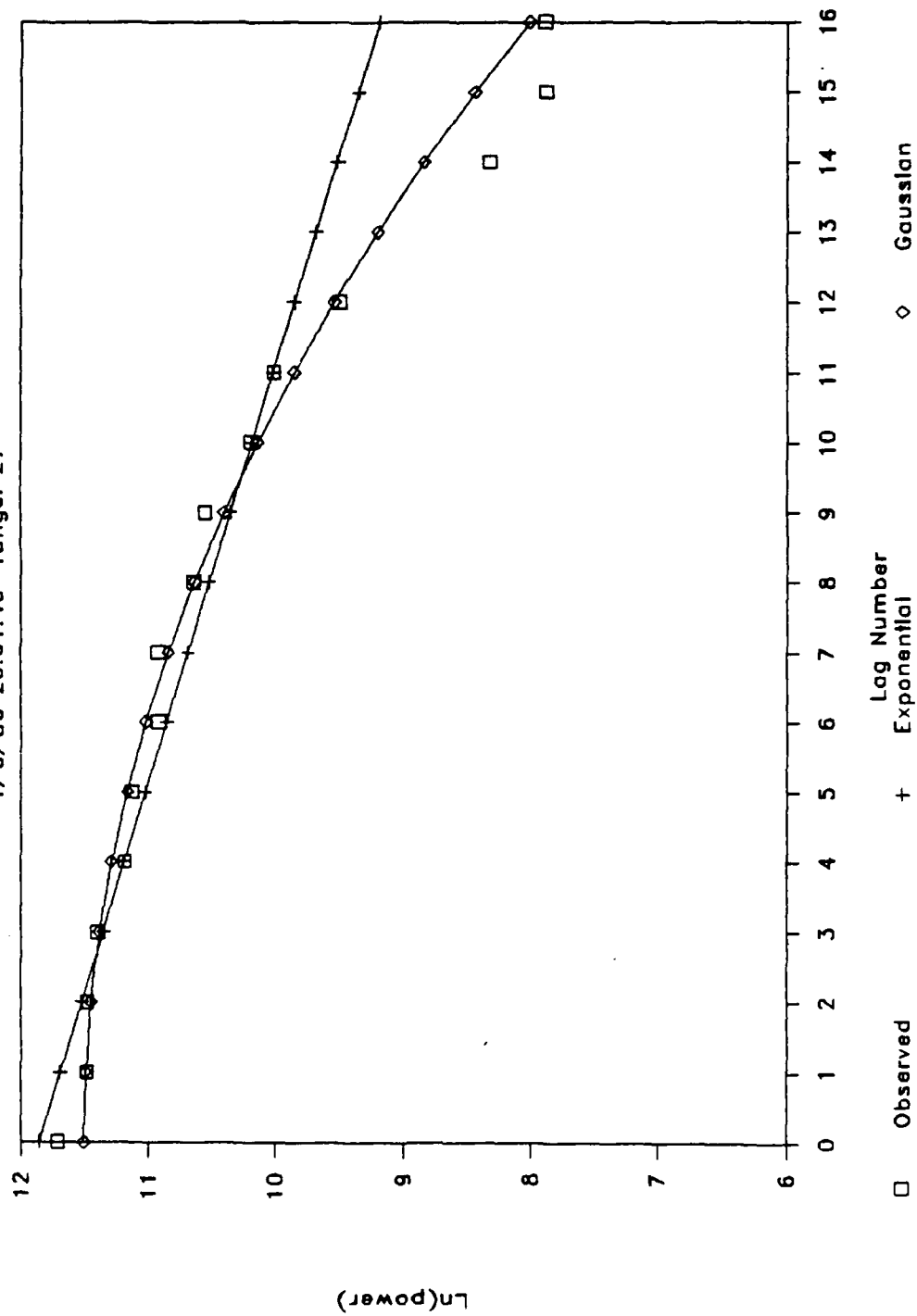
Comparison of Power Fits

1/6/86 20:01:45 range: 27

FIGURE 2b

□ Observed

Lag Number
+ Exponential

◇ Gaussian
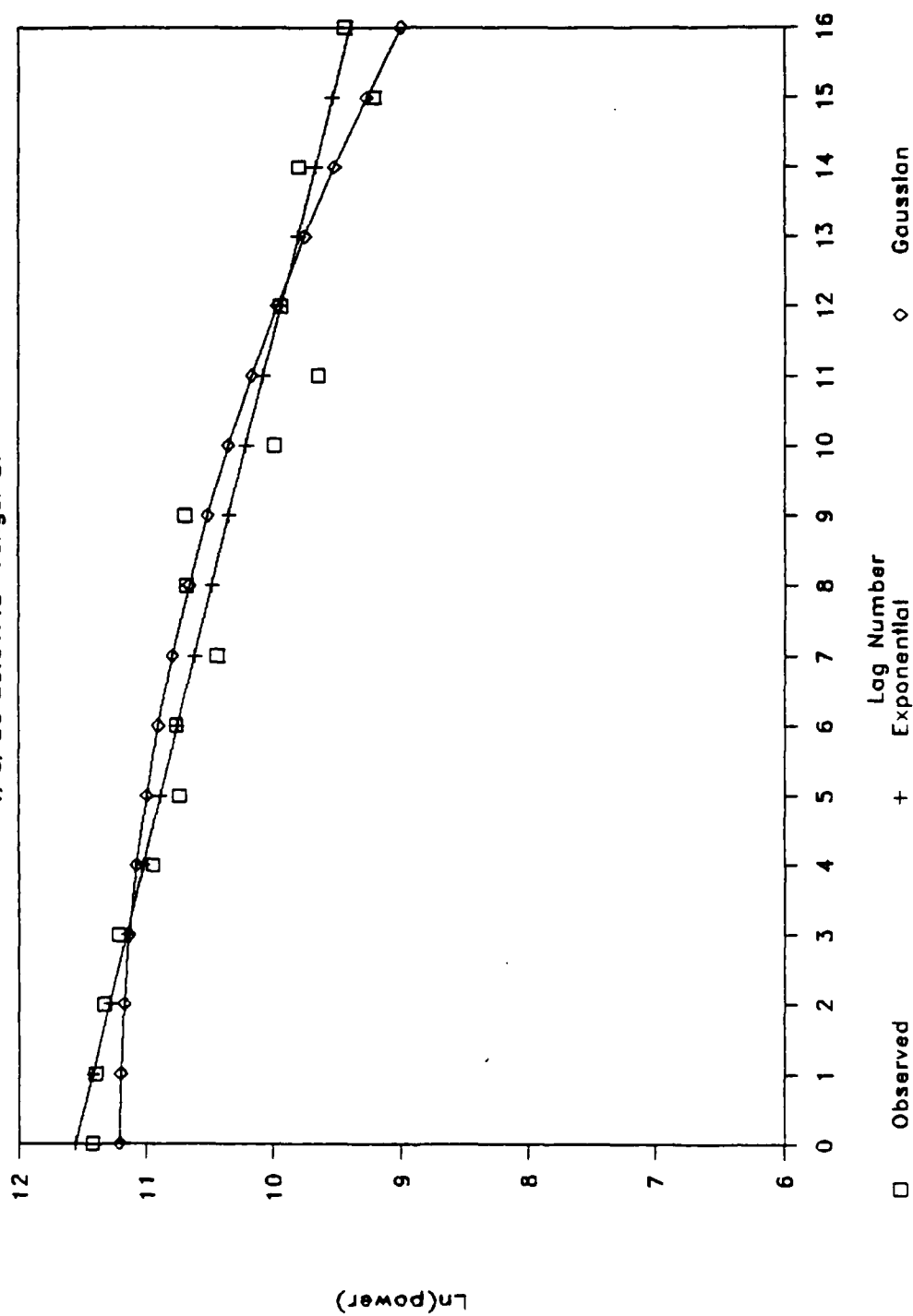
DECORRELATION TIME DISTRIBUTION
FOR TWO SPECIFIC EVENTS

IONOSPHERIC SCATTER 9/7/85 1820 – 2000 UT ━━━━━

GROUND SCATTER 4/16/85 2005 – 2150 UT ────

>6 dB

690 pts

727 pts

3 – 6 dB

909 pts

399 pts

0 – 3 dB

470 pts

1738 pts

PERCENT

DECORRELATION PARAMETER (1/T)
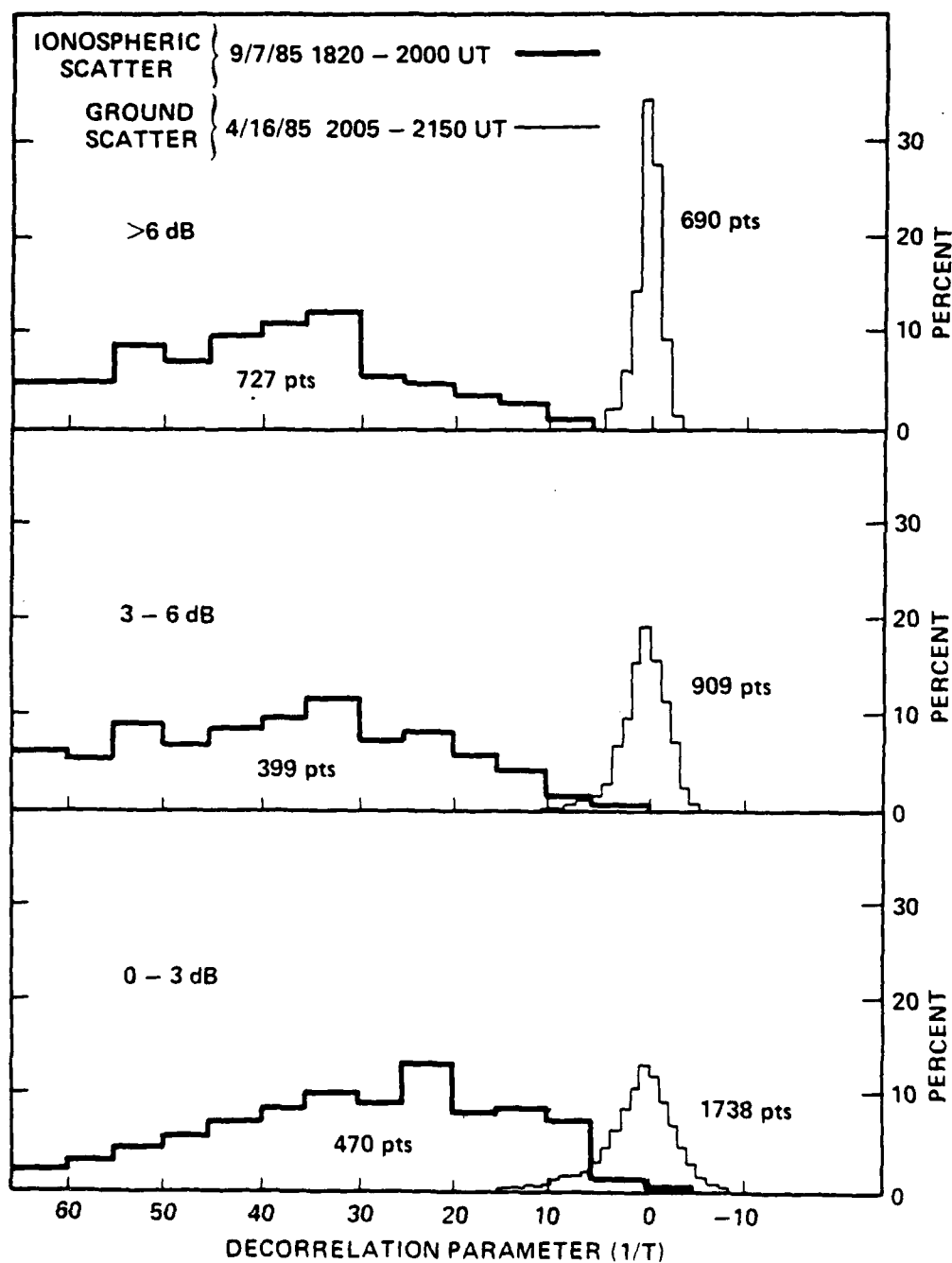
FIGURE 3

Probability of Seeing Scatter vs. No Scatter

		Time (UT)				
		0 - 6	6 - 12	12 - 18	18 - 24	sum
scatter						
	obs.	37	13	16	36	102
	expect	25	15	32	29	
	(e-o)^2/e	5.3	0.3	8.2	1.5	
no scatter						
	obs.	7	13	40	15	75
	expect	19	11	24	22	
	(e-o)^2/e	7.3	0.4	11.2	2.0	
sum		44	26	56	51	177
prob. of scatter		84	50	29	71	58

chi-sq = 36.1
chi-sq/deg-free 9.0

Probability of Scatter

Based on 177 randomly selected times
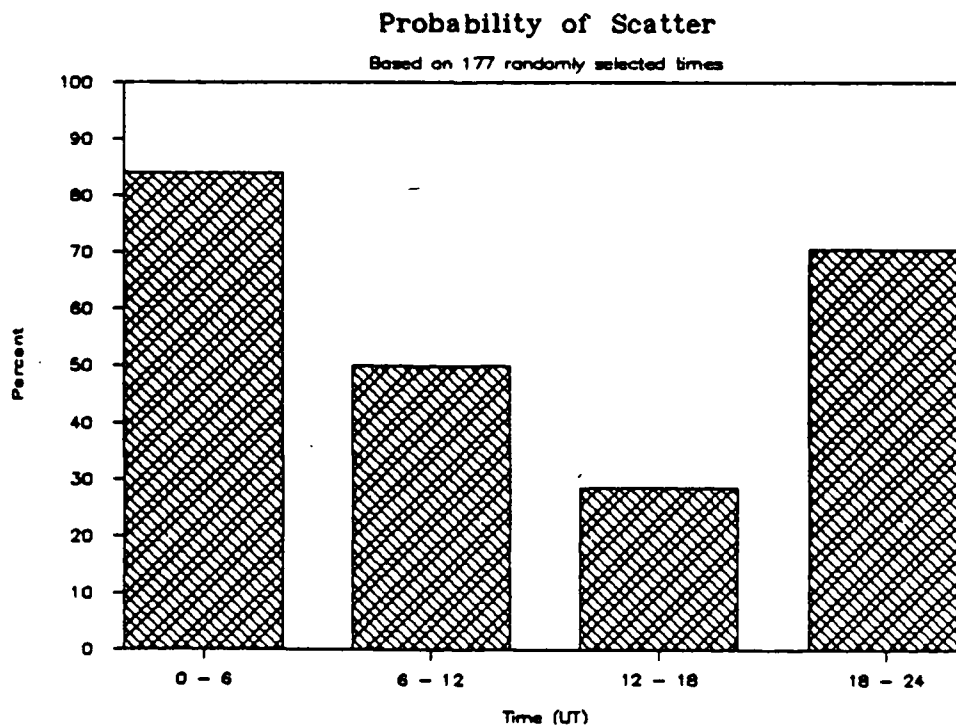
FIGURE 4

Scatter type	Time				sum
	6-12	12-18	18-24		
IONOSPHERIC					
obs	20	8	7	20	55
exp	18.5	7.0	9.2	20.2	
$(e-o)^2/e$	0.1	0.1	0.5	.0	
GROUND					
obs	8	1	4	8	21
exp	7.1	2.7	3.5	7.7	
$(e-o)^2/e$	0.1	1.1	0.1	.0	
BOTH					
obs	14	7	10	· 18	49
exp	16.5	6.3	8.2	18.0	
$(e-o)^2/e$	0.4	0.1	0.4	.0	
SUM	42	16	21	46	125
PROBABILITY					
Ionos.	48	50	33	43	44
Ground	19	6	19	17	17
Both	33	44	48	39	39

CHI-SQUARE

sum $(e-o)^2/e$	2.893881
degrees of freedom	6
sum/deg.of.free	0.482313

Type of Scatter vs Time
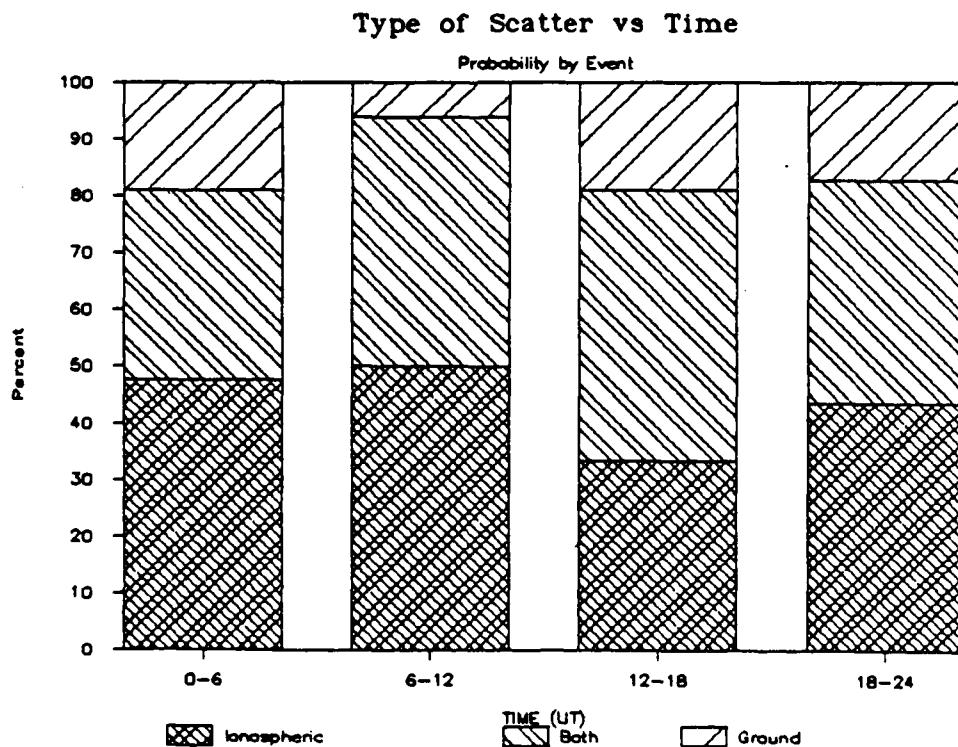
FIGURE 5

Scatter type	0	1	2	3	4	5	6	7	8	Unknwn		sum
IONOSPHERIC												
obs	6	5	9	15	7	6	3	0	1	3		55
exp	4.8	11.9	12.8	9.2	4.8	3.1	1.3	0.0	0.4	6.6		
$(e-o)^2/e$	0.3	4.0	1.1	3.6	1.0	2.8	2.1	0.0	0.7	2.0		
GROUND												
obs	3	8	4	1	0	0	0	0	0	5		21
exp	1.8	4.5	4.9	3.5	1.8	1.2	0.5	0.0	0.2	2.5		
$(e-o)^2/e$	0.7	2.6	0.2	1.8	1.8	1.2	0.5	0.0	0.2	2.4		
BOTH												
obs	2	14	16	5	4	1	0	0	0	7		49
exp	4.3	10.6	11.4	8.2	4.3	2.7	1.2	0.0	0.4	5.9		
$(e-o)^2/e$	1.2	1.1	1.9	1.3	.0	1.1	1.2	0.0	0.4	0.2		
SUM	11	27	29	21	11	7	3	0	1	15		125
PROBABILITY												
Ionos.	55	19	31	71	64	86	100	0	100	20		44
Ground	27	30	14	5	0	0	0	0	0	33		17
Both	18	52	55	24	36	14	0	0	0	47		39

CHI-SQUARE

sum $(e-o)^2/e$	37.38624
degrees of freedom	18
sum/deg.of.free	2.077013

Scatter Type vs Kp

Probability by Event
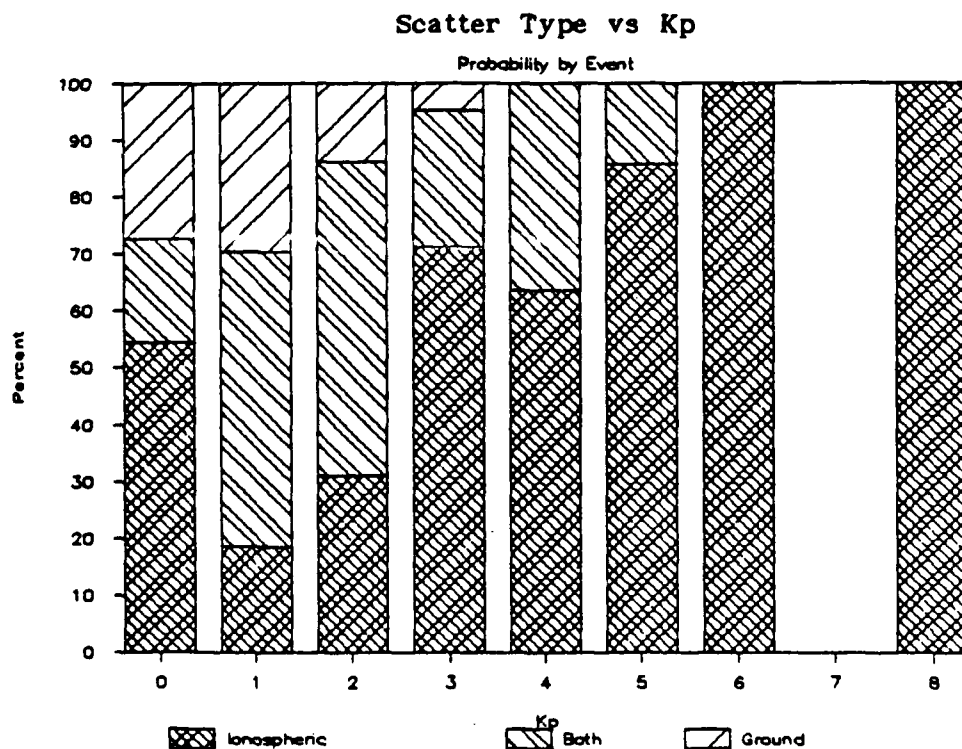
FIGURE 6

FIGURE 7

scatter region	TIME 0-6	6-12	12-18	18-24	sum
E-region					
obs	9	7	0	6	22
exp	6.3	3.0	3.8	8.9	
(e-o)^2/e	1.1	5.2	3.8	0.9	
F-region					
obs	10	4	14	28	56
exp	16.1	7.7	9.7	22.5	
(e-o)^2/e	2.3	1.8	2.0	1.3	
Both					
obs	6	1	1	1	9
exp	2.6	1.2	1.6	3.6	
(e-o)^2/e	4.5	.0	0.2	1.9	
Sum	25	12	15	35	87
PROBABILITY					
E	36	58	0	17	25
F	40	33	93	80	64
both	24	8	7	3	10

CHI-SQUARE
sum (e-o)^2/e   25.05989
degrees of freedom   6
sum/deg.of.free   4.176648

Scattering Region vs Time

Probability by Event
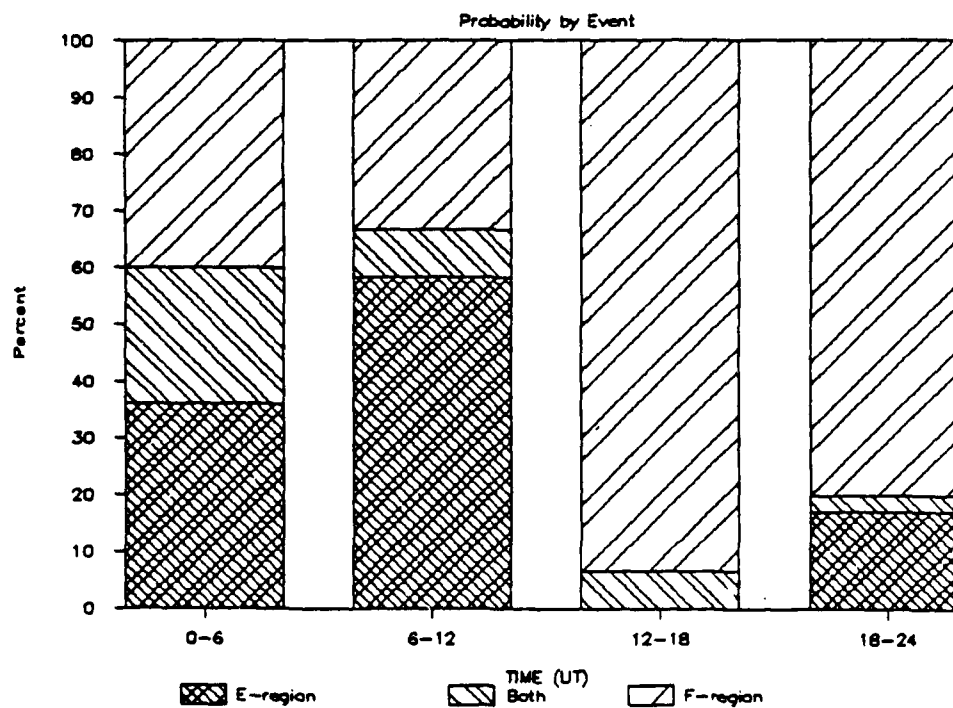
scatter region		0	1	2	3	4	5	6	7	8	Unknwn		sum
						Kp							
E-region													
obs		1	3	4	6	2	2	2	0	1	1		22
exp		2.1	3.4	5.2	4.1	2.6	1.6	0.8	0.0	0.3	2.1		
(e-o)^2/e		0.6	.0	0.3	0.8	0.1	0.1	1.9	0.0	2.1	0.6		
F-region													
obs		6	9	14	8	7	4	0	0	0	6		54
exp		5.1	8.3	12.7	10.2	6.4	3.8	1.9	0.0	0.6	5.1		
(e-o)^2/e		0.2	0.1	0.1	0.5	0.1	.0	1.9	0.0	0.6	0.2		
Both													
obs		1	1	2	2	1	0	1	0	0	1		9
exp		0.8	1.4	2.1	1.7	1.1	0.6	0.3	0.0	0.1	0.8		
(e-o)^2/a		.0	0.1	.0	0.1	.0	0.6	1.5	0.0	0.1	.0		
Sum		8	13	20	16	10	6	3	0	1	8		85
PROBABILITY													
E		13	23	20	38	20	33	67	0	100	13		26
F		75	69	70	50	70	67	0	0	0	75		64
both		13	8	10	13	10	0	33	0	0	13		11

CHI-SQUARE
sum (e-o)^2/e   12.59846
degrees of freedom   18
sum/deg.of.free   0.699914

Region of Scatter vs Kp

Probability by Event
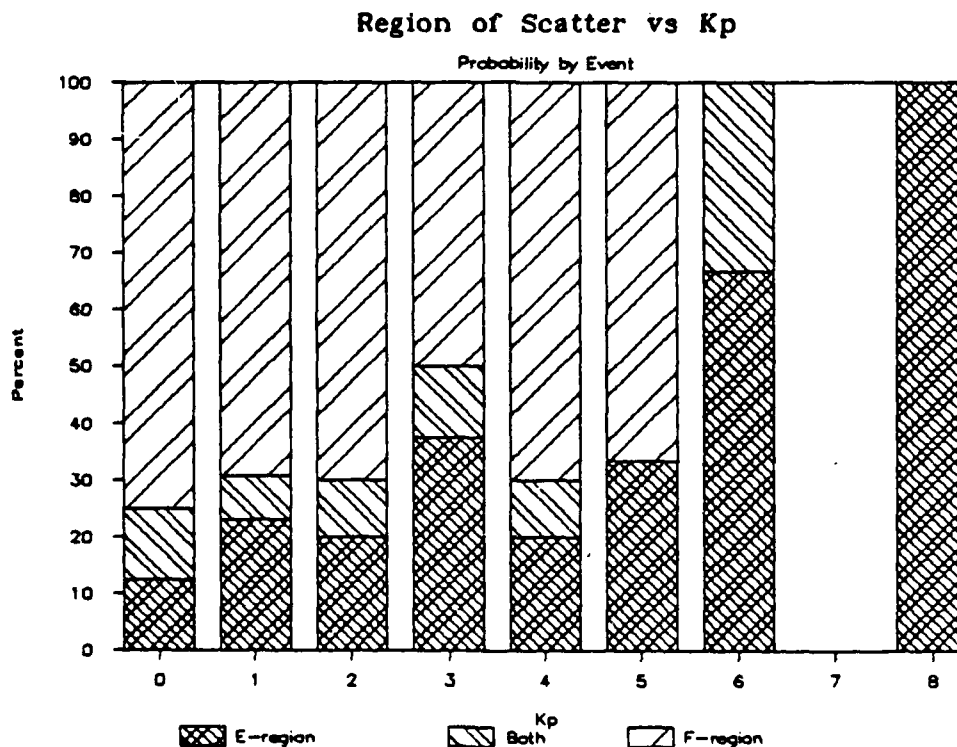
FIGURE 8

FITTED POWER VS LAG-0 POWER
all data
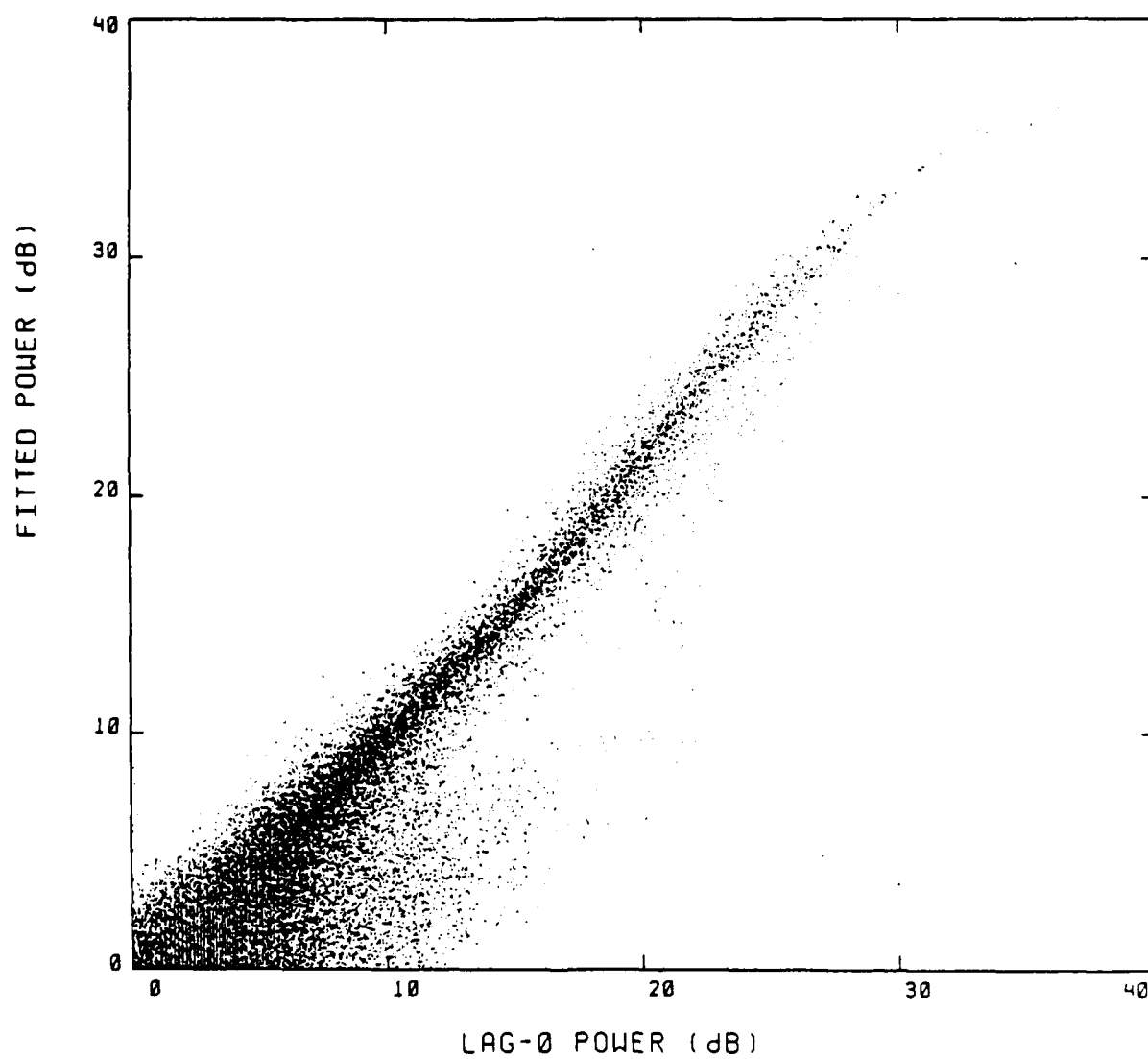
Figure 9

VELOCITY ERROR VS LAG-0 POWER
all data
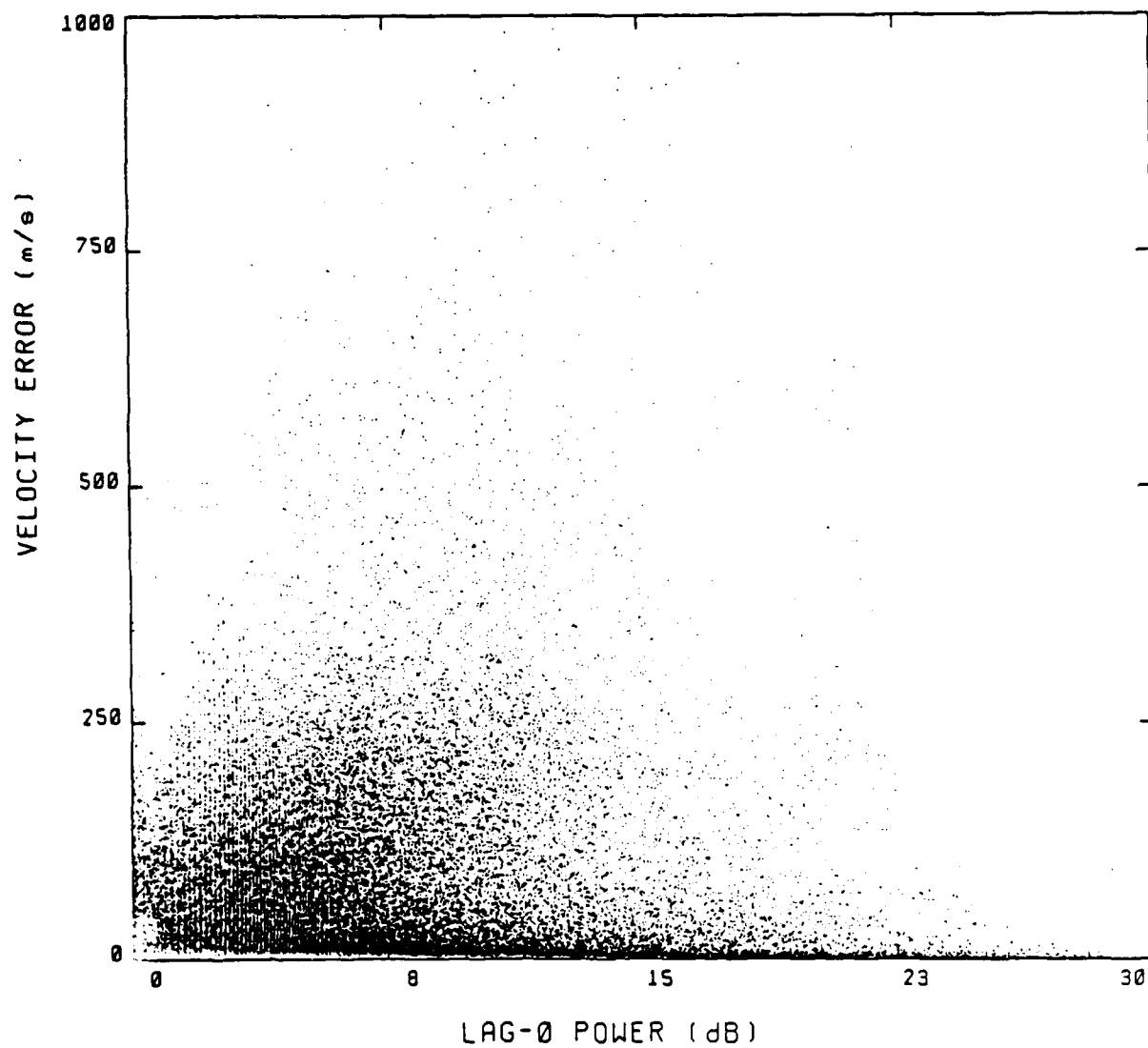
FIGURE 10a

VELOCITY ERROR VS FITTED POWER
all data
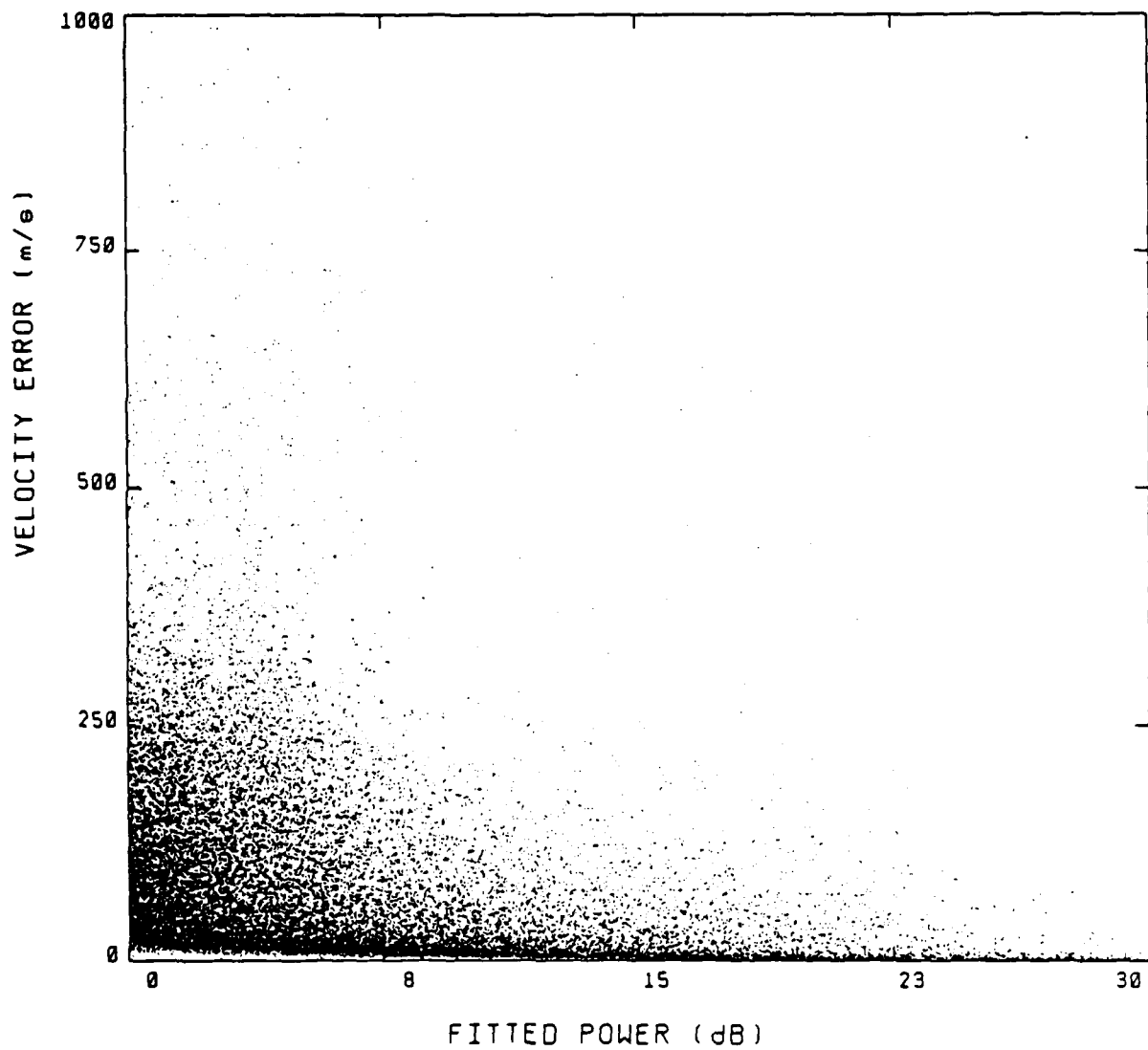
FIGURE 10b

VELOCITY ERROR VS SPECTRAL WIDTH
all data
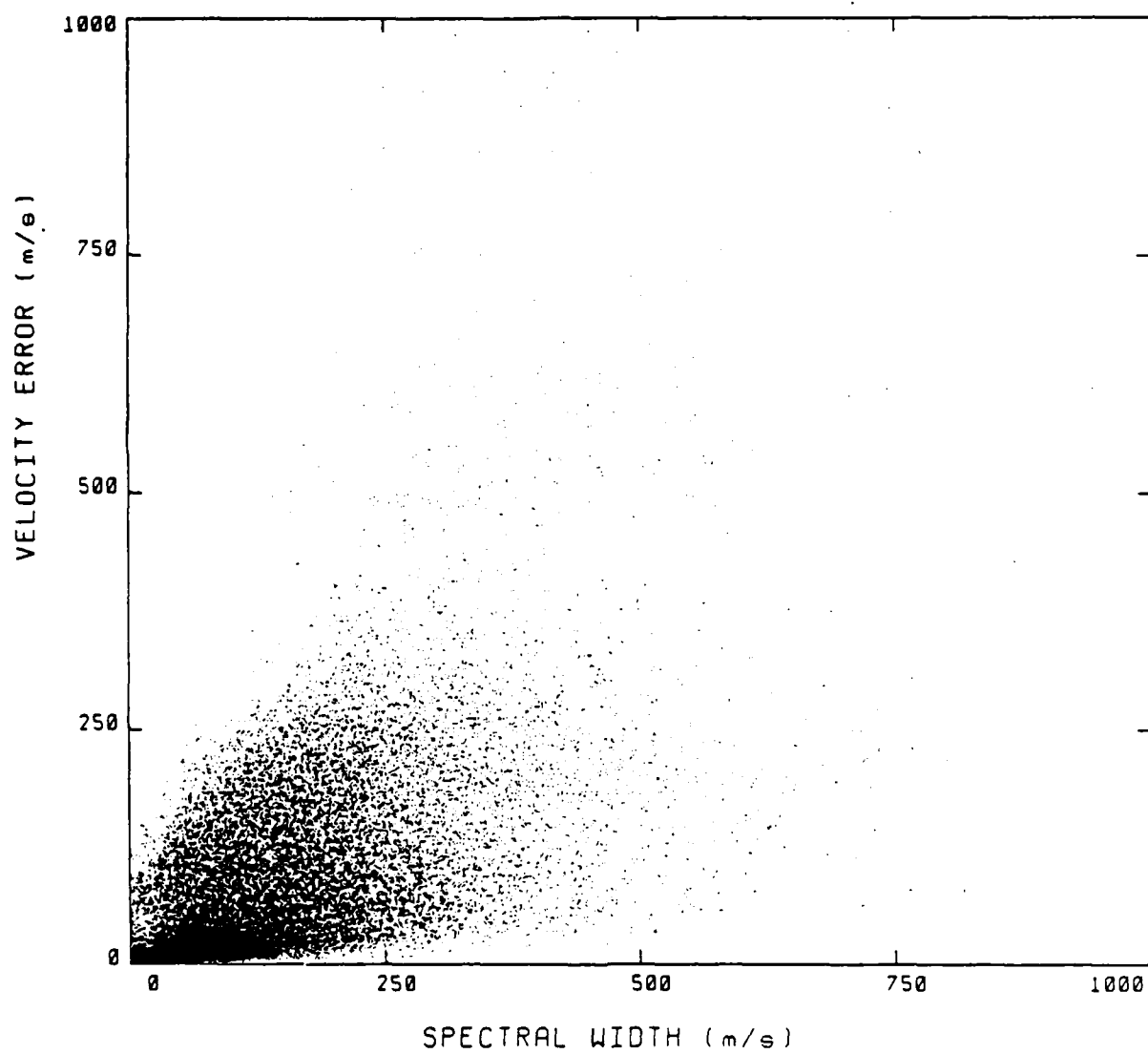
Figure 11

SPECTRAL WIDTH VS POWER
SNR > 0 dB
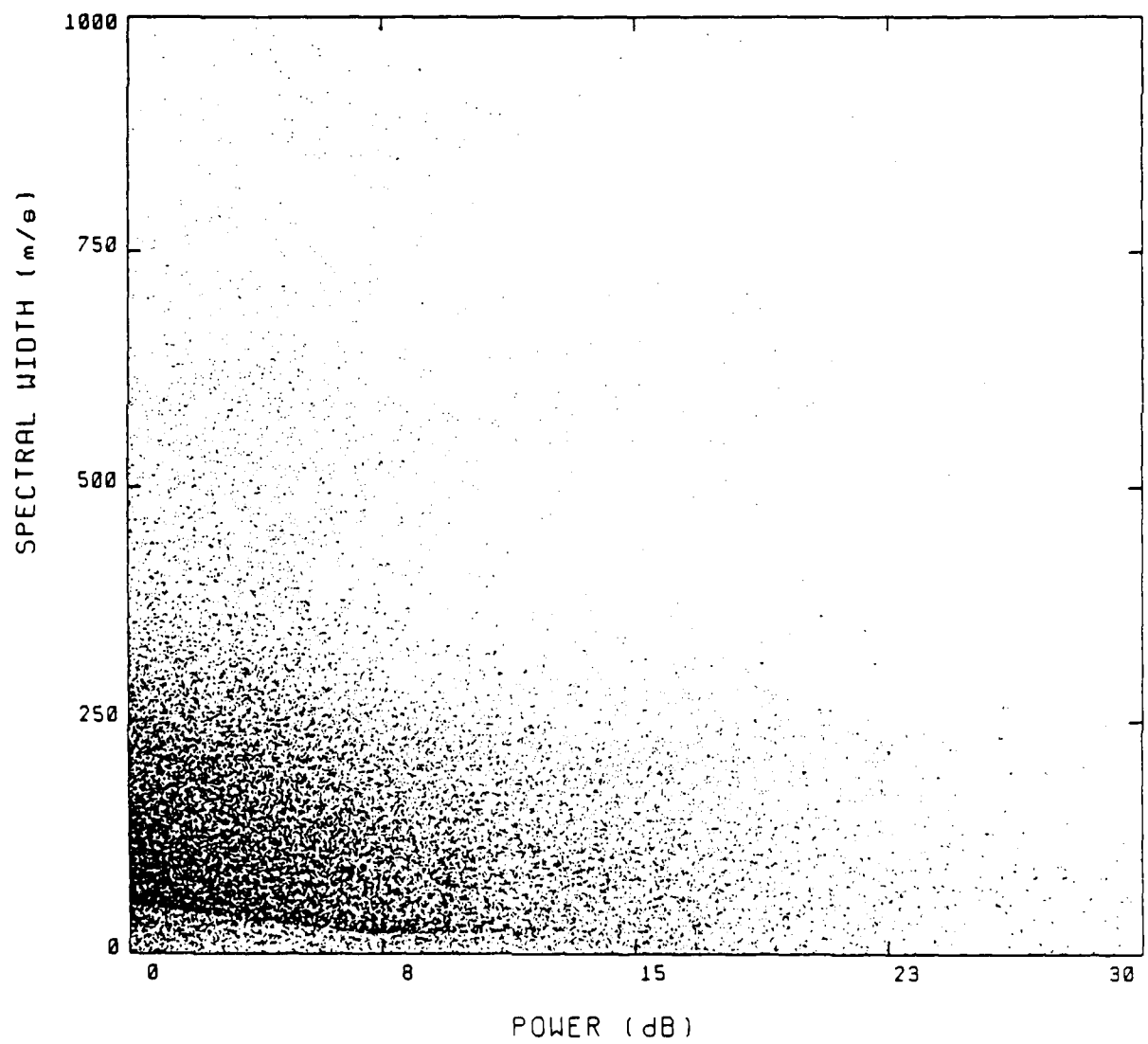
Figure 12

POWER VS RANGE

Verr < 250 m/s. SNR > 0 dB
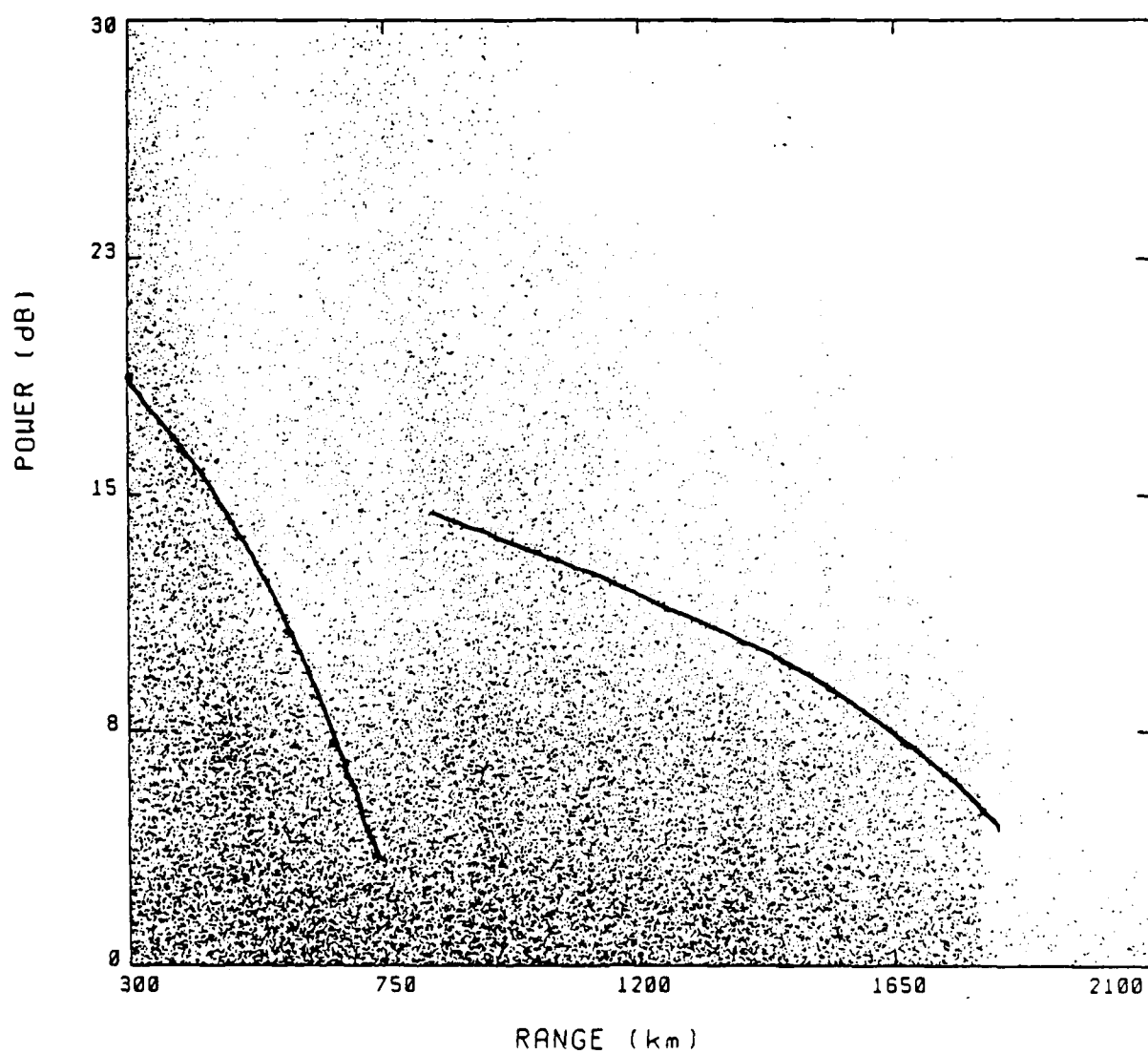
Figure 13

RANGE VS VELOCITY
Verr < 250 m/s. SNR > 0 dB
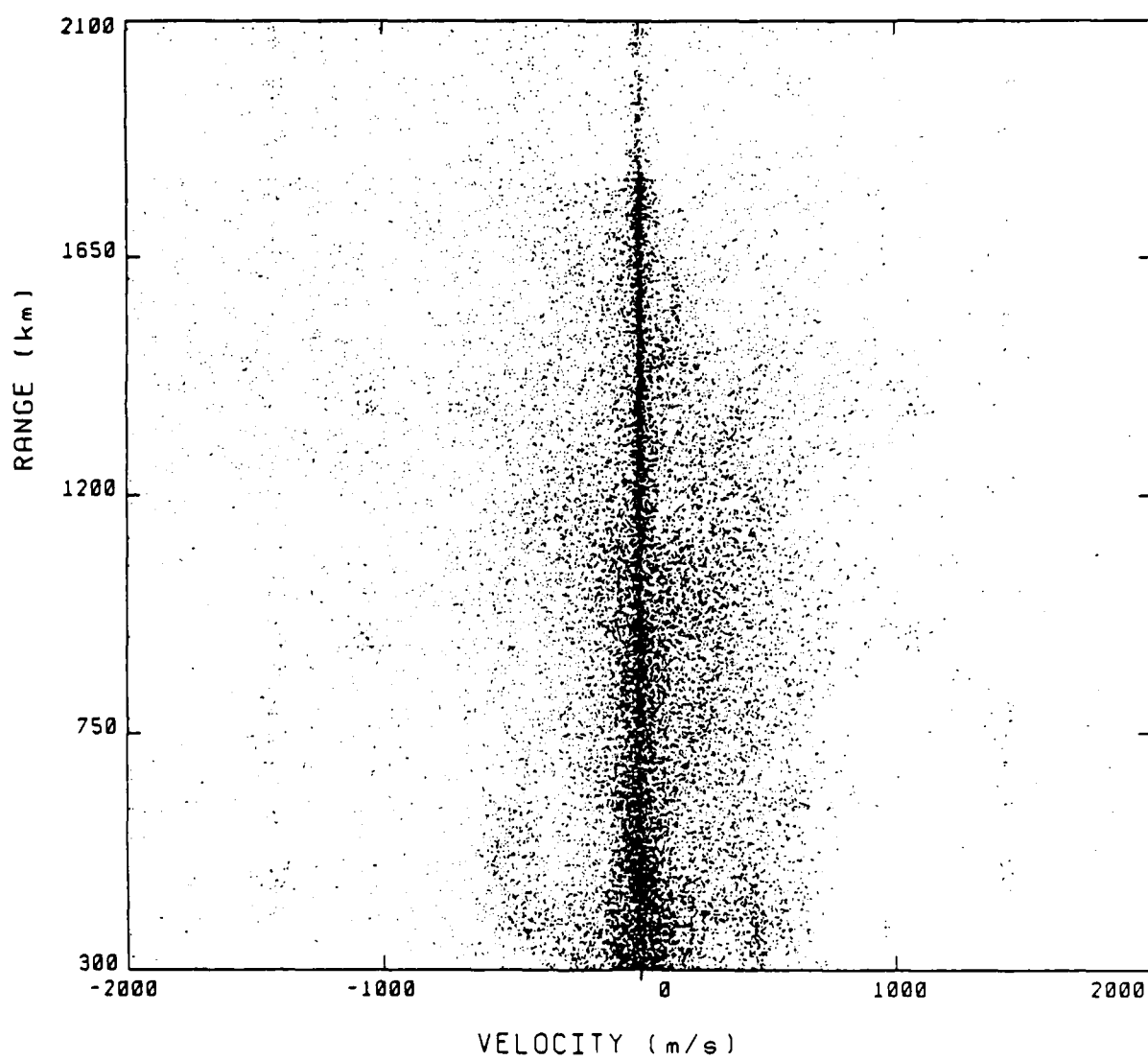
FIGURE 14a

RANGE VS VELOCITY
Verr < 250 m/s. SNR > 10 dB
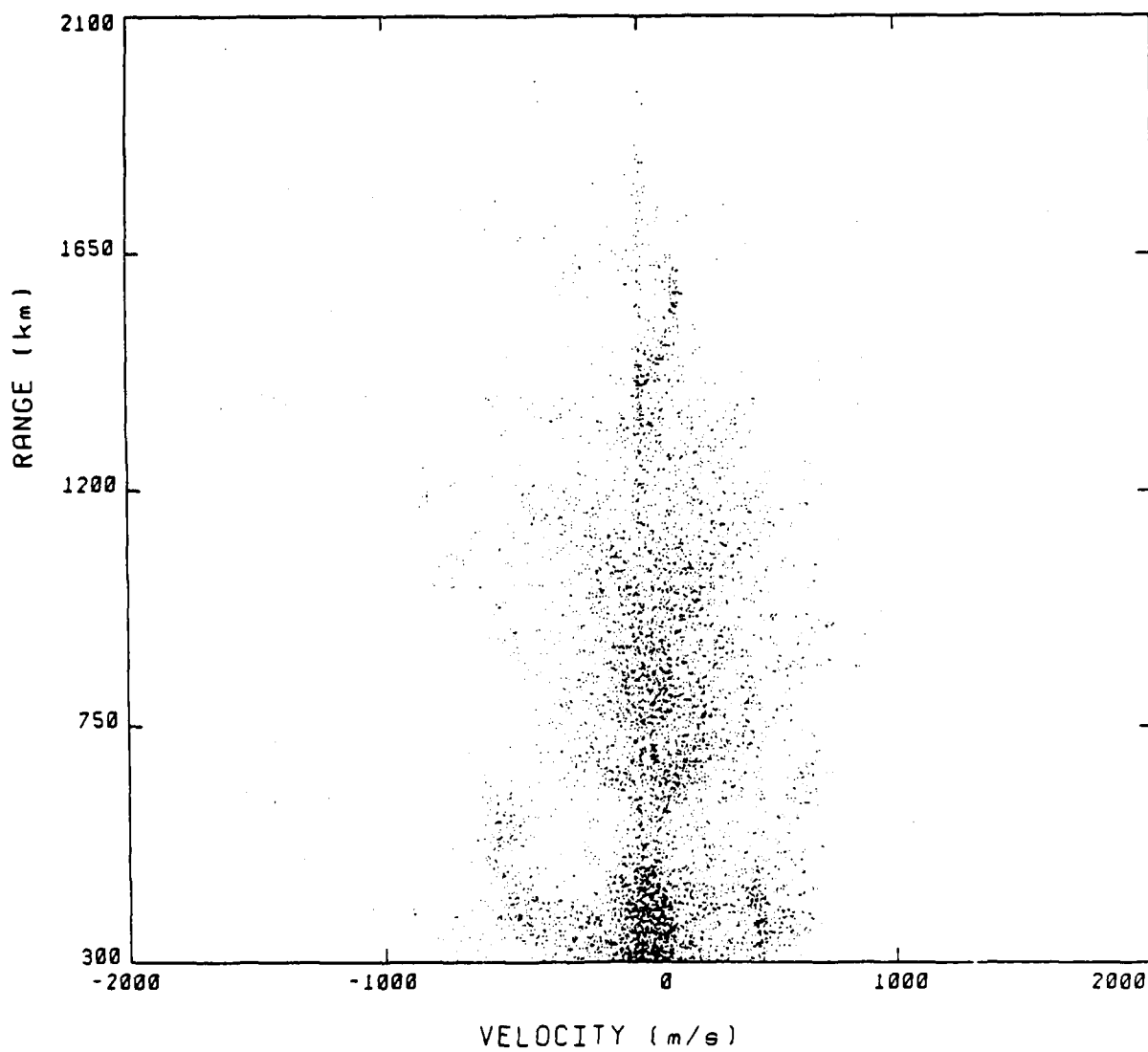
FIGURE 14b

RANGE VS VELOCITY
Verr < 250 m/s. SNR > 0 dB. Kp < 2-
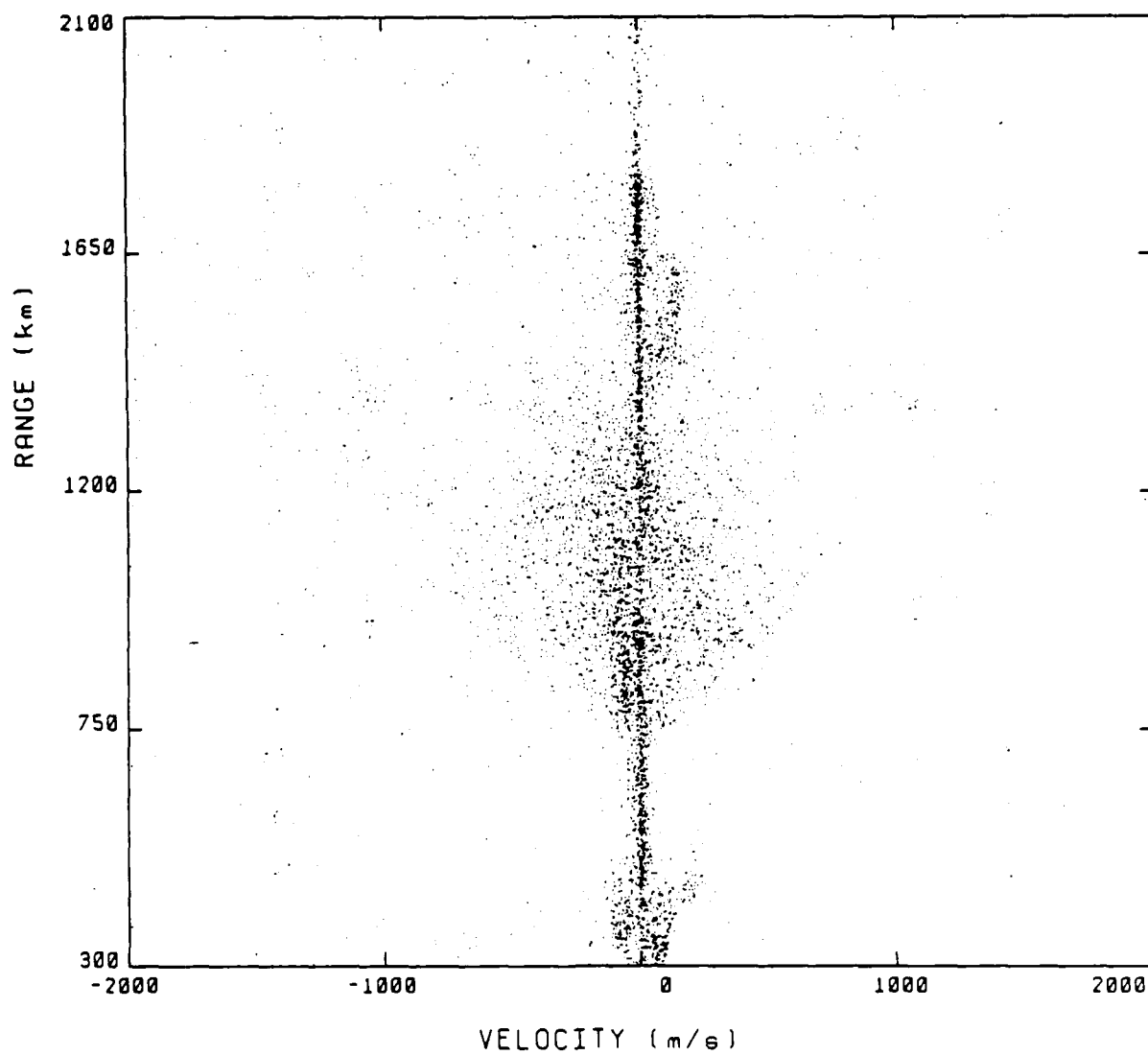
FIGURE 15a

RANGE VS VELOCITY
Verr < 250 m/s. SNR > 0 dB. Kp >= 4-

VELOCITY (m/s)

FIGURE 15b

(a)
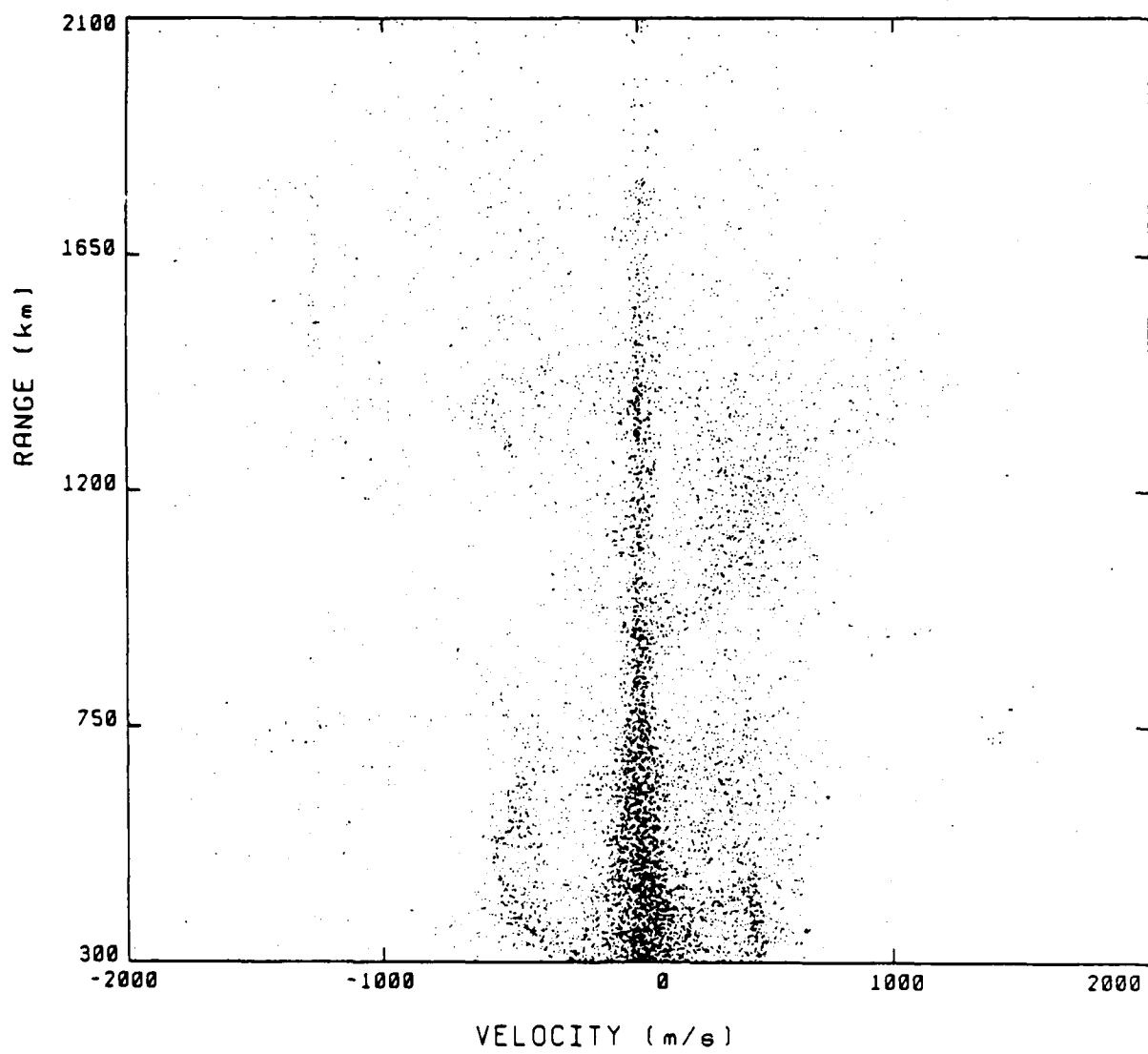
(b)
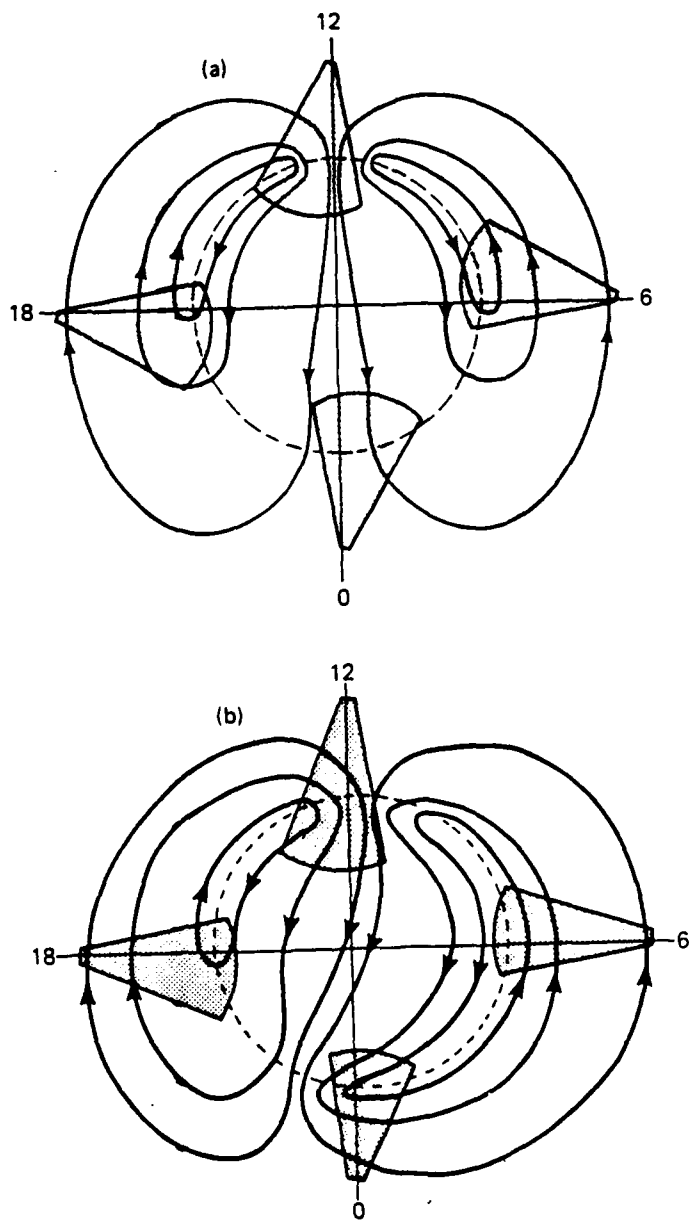
FIGURE 16

RANGE VS VELOCITY

Verr < 250 m/s. SNR > 0 dB. 0 - 6 UT
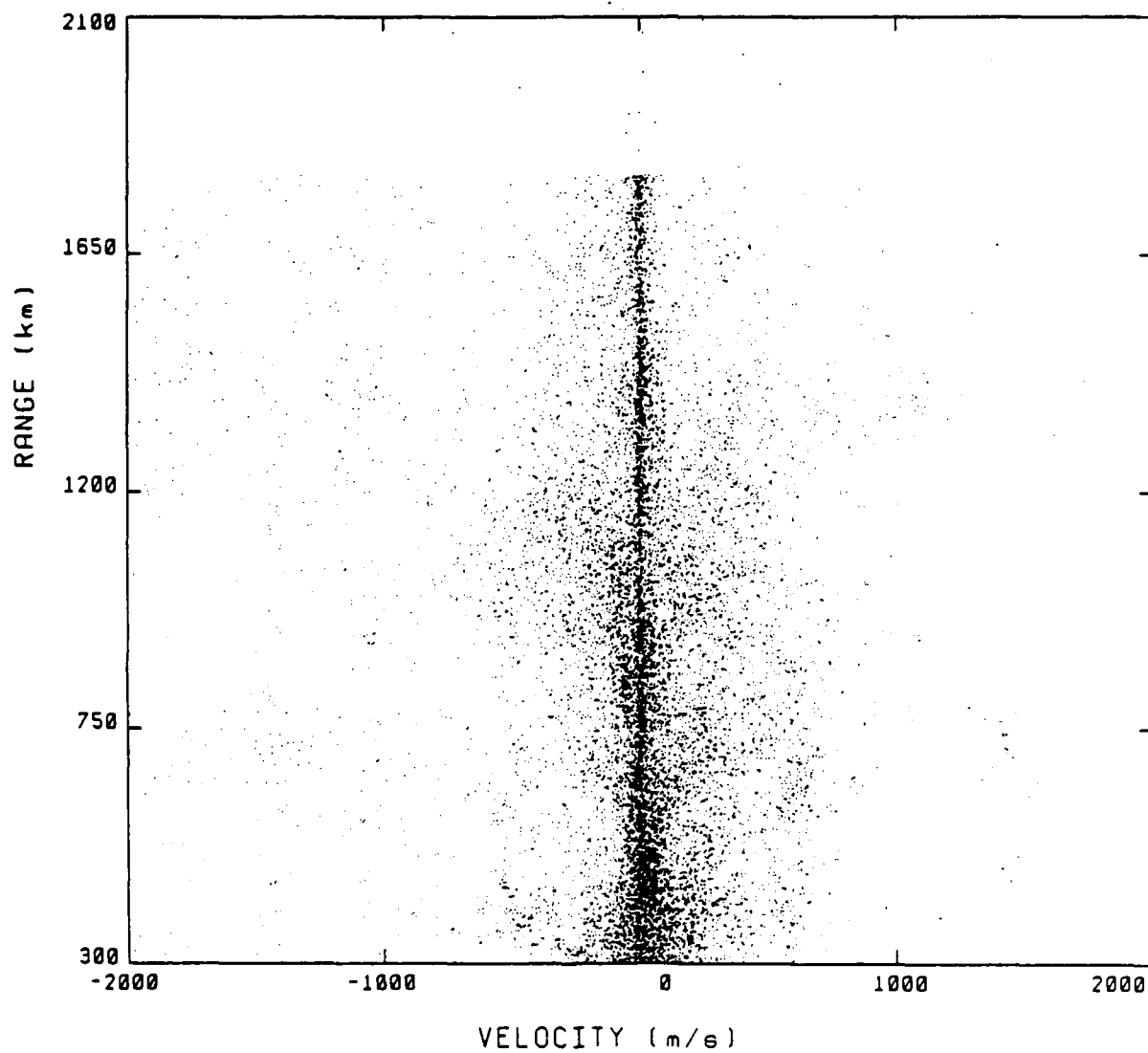
FIGURE 17a

RANGE VS VELOCITY
Verr < 250 m/s. SNR > 0 dB. 6 - 12 UT
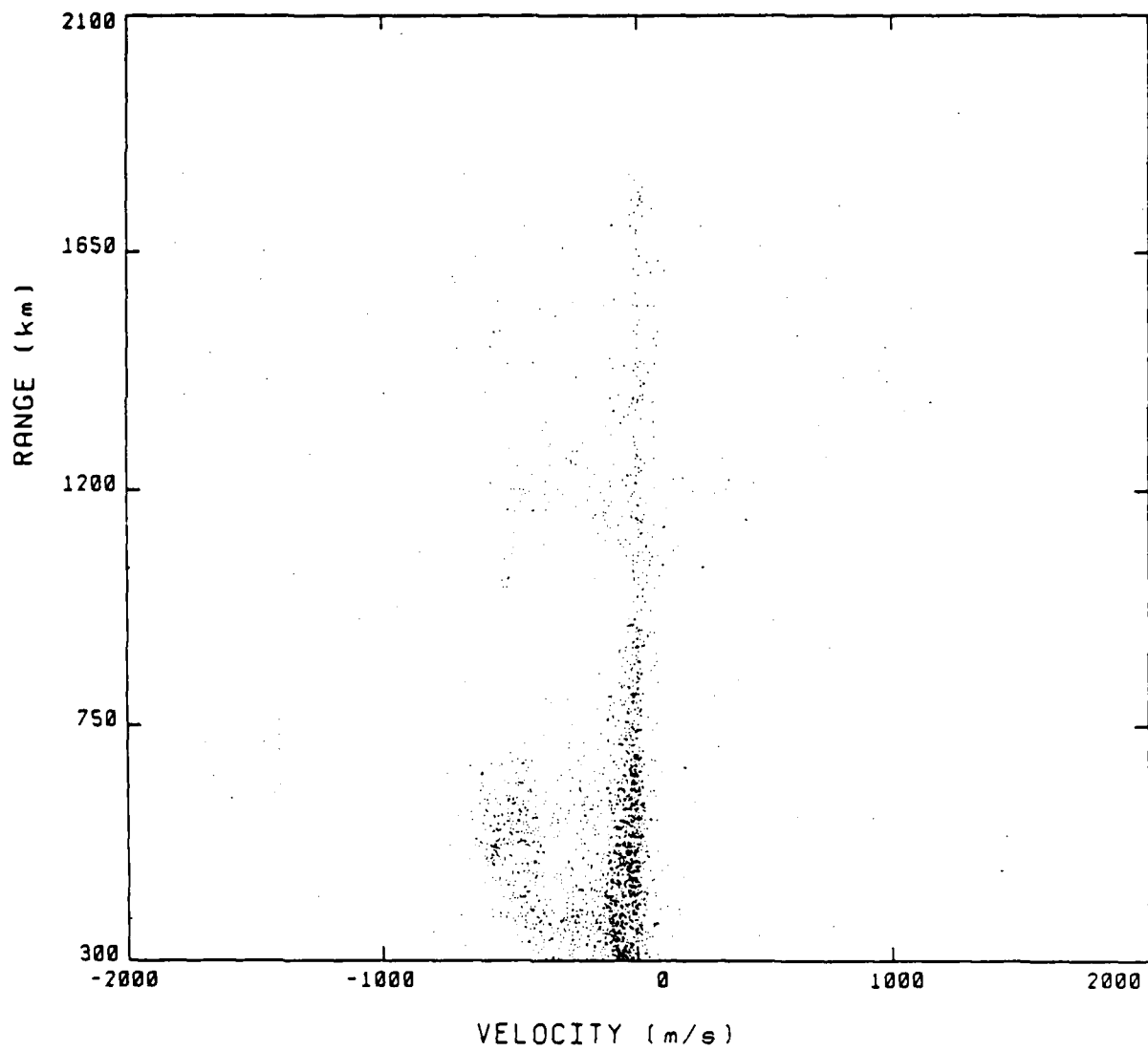
FIGURE 17b

RANGE VS VELOCITY

Verr < 250 m/s. SNR > 0 dB. 12 - 18 UT
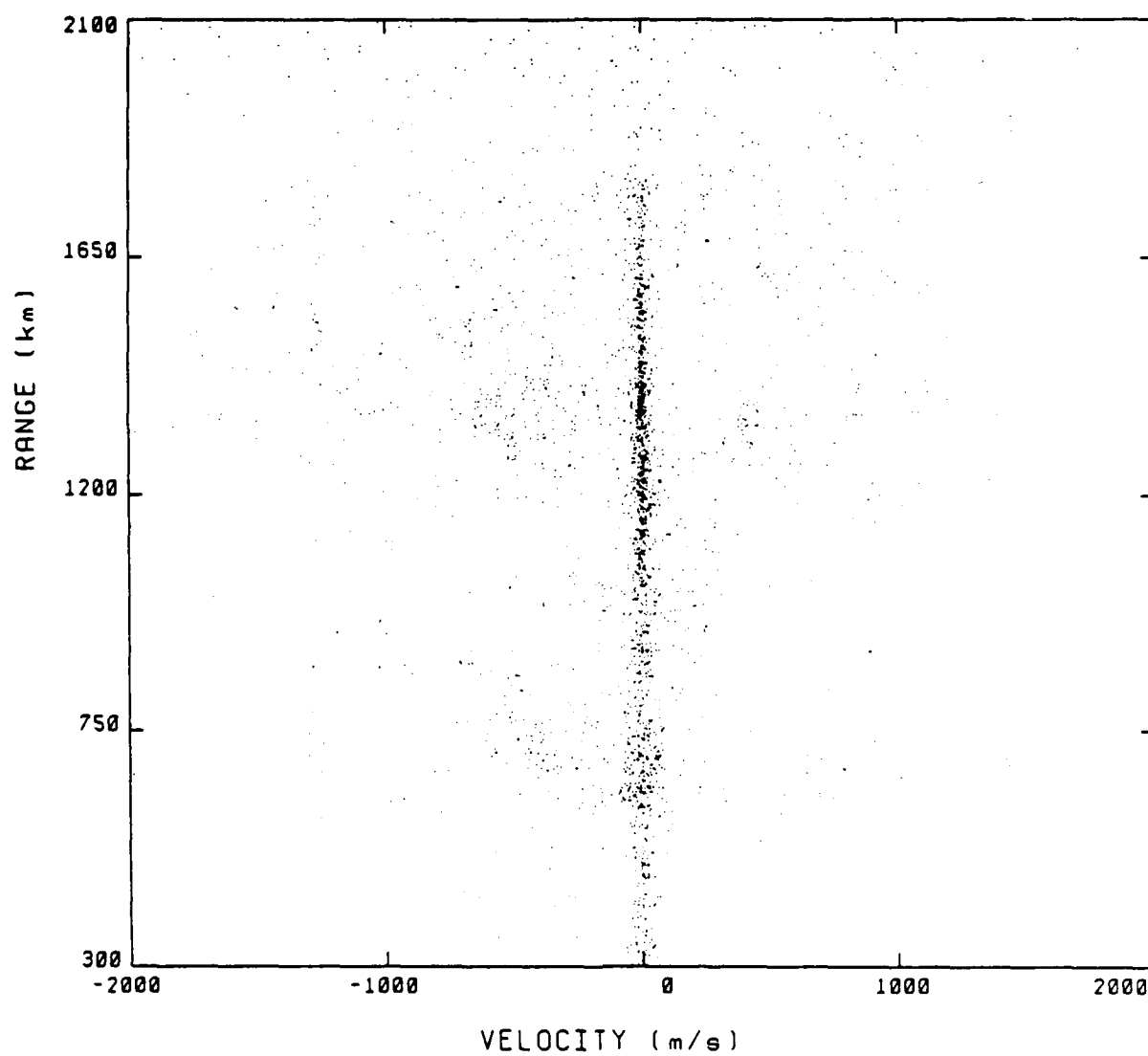
VELOCITY (m/s)

FIGURE 17c

RANGE VS VELOCITY

Verr < 250 m/s. SNR > 0 dB. 18 - 24 UT
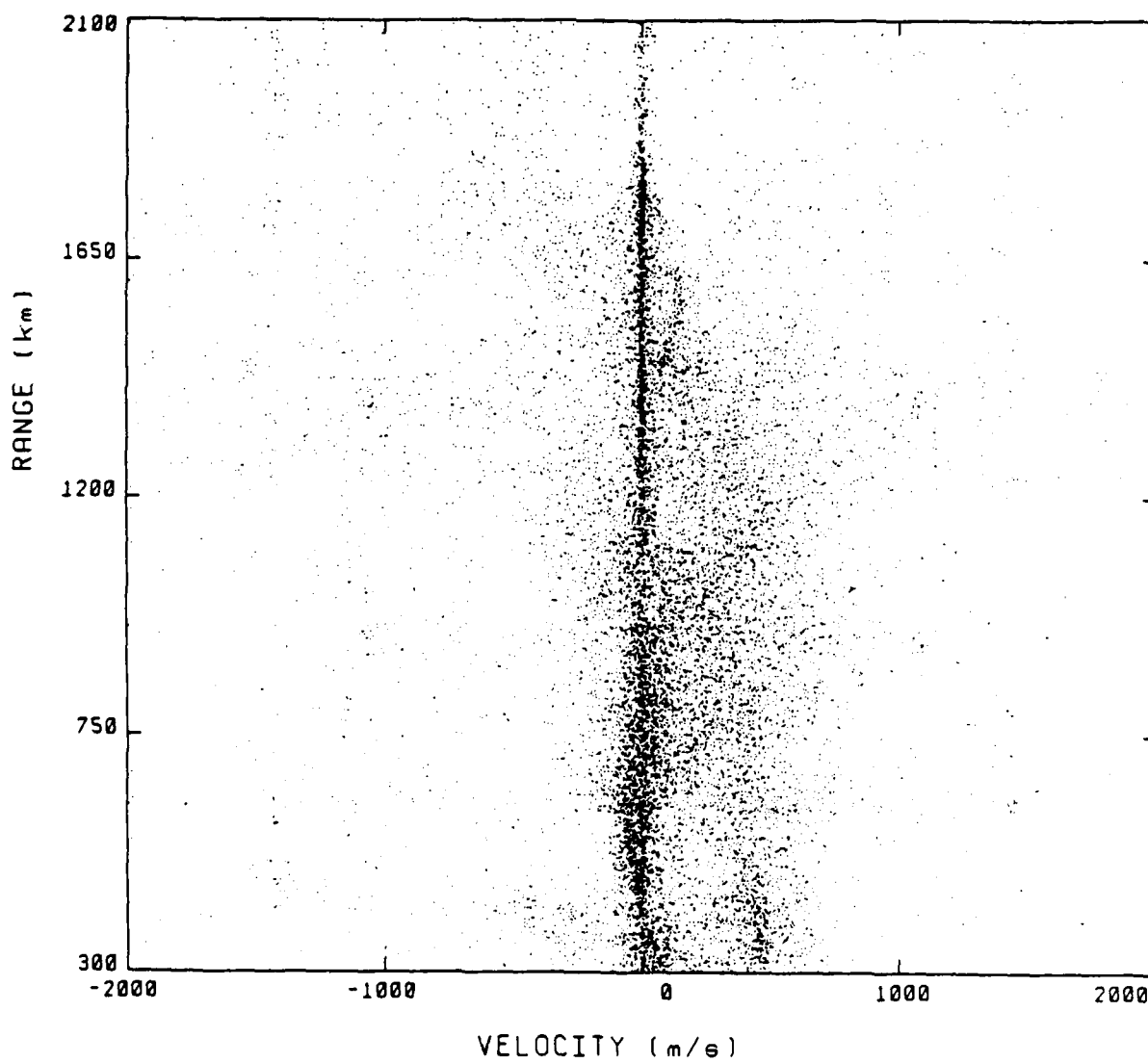
FIGURE 17d

SPECTRAL WIDTH VS POWER
300 - 600 km
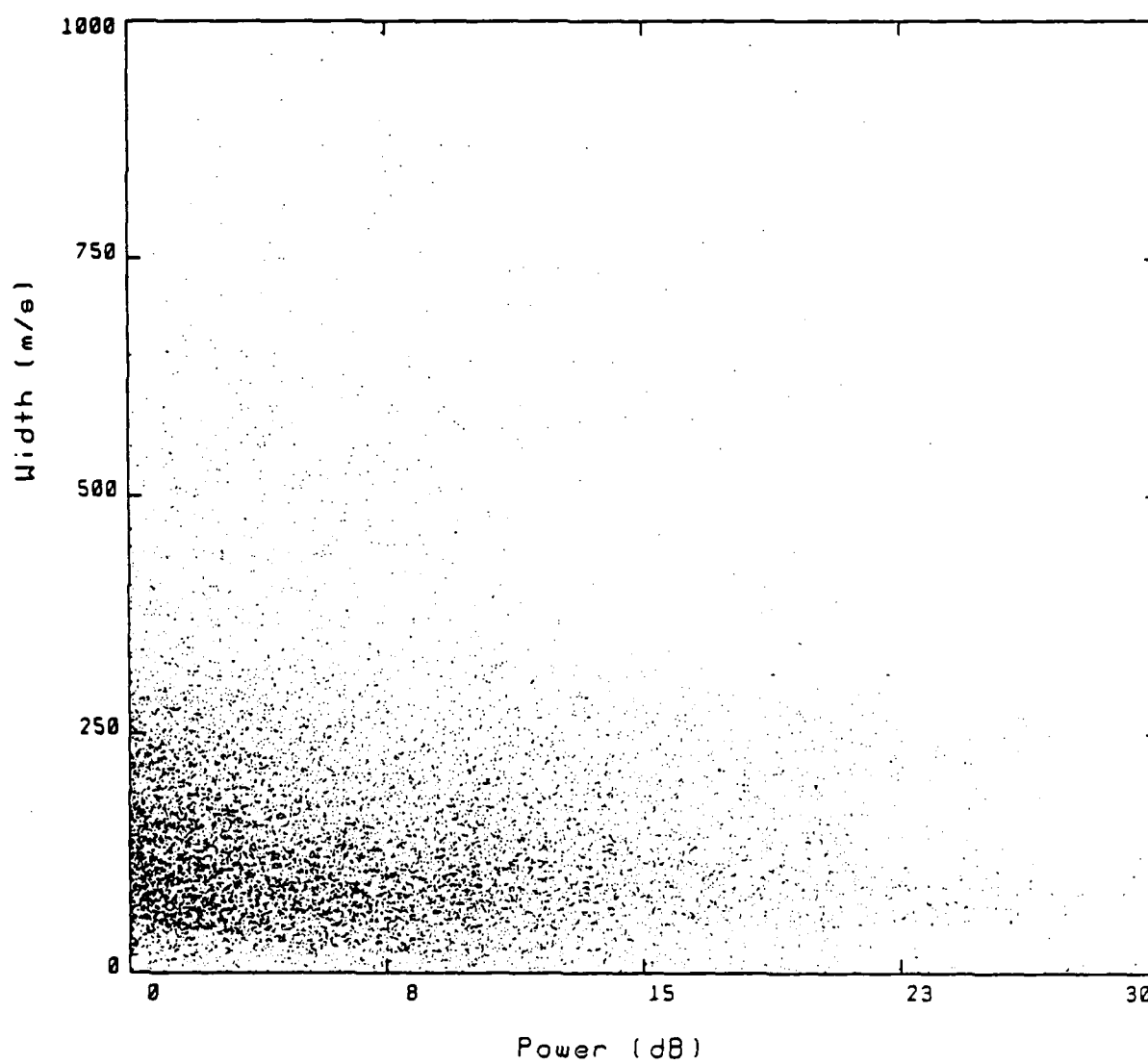
FIGURE 18a

SPECTRAL WIDTH VS POWER
900 - 2100 km
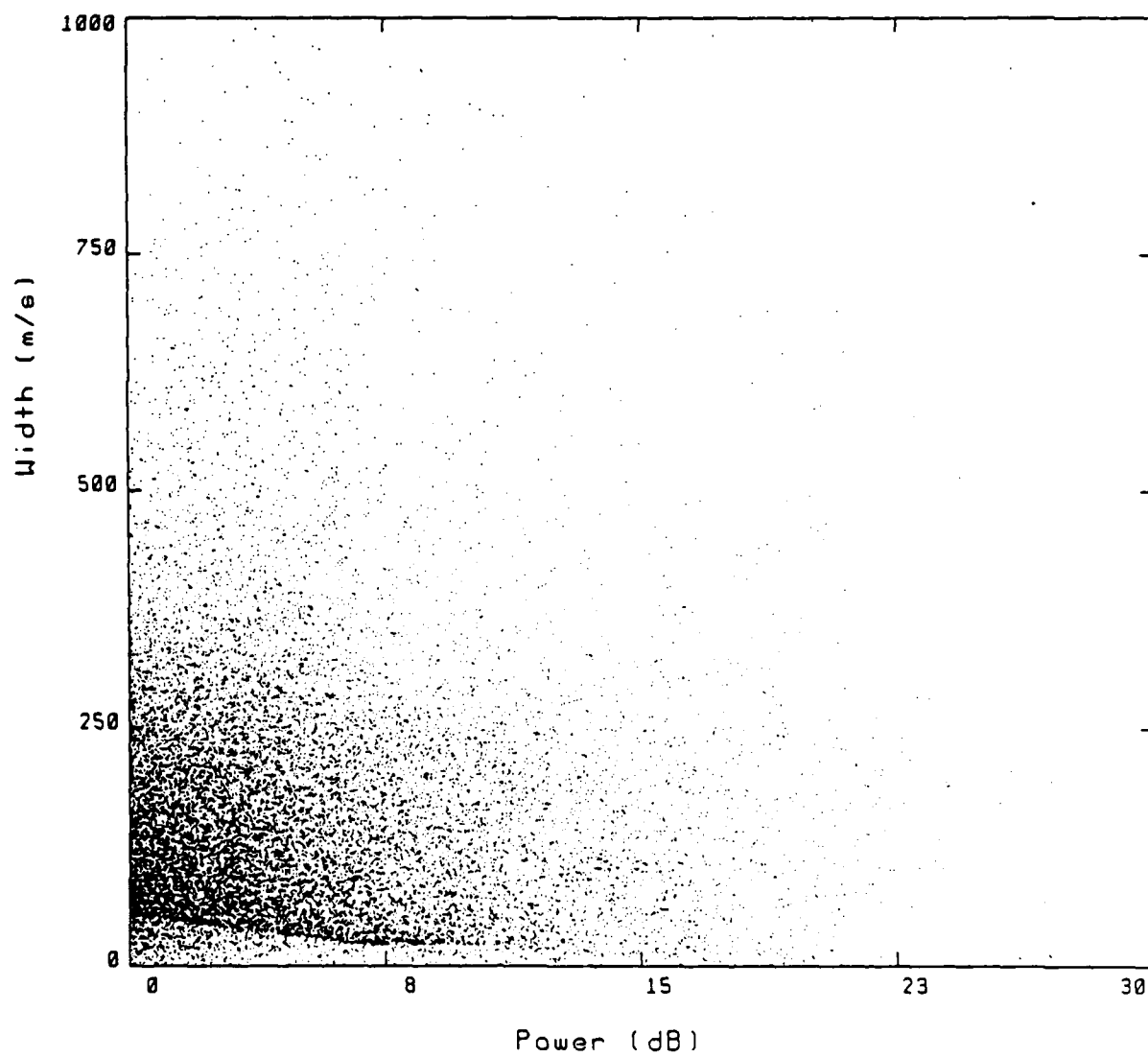
FIGURE 18b

SPECTRAL WIDTH VS VELOCITY
SNR > 0 dB. 300 - 600 km
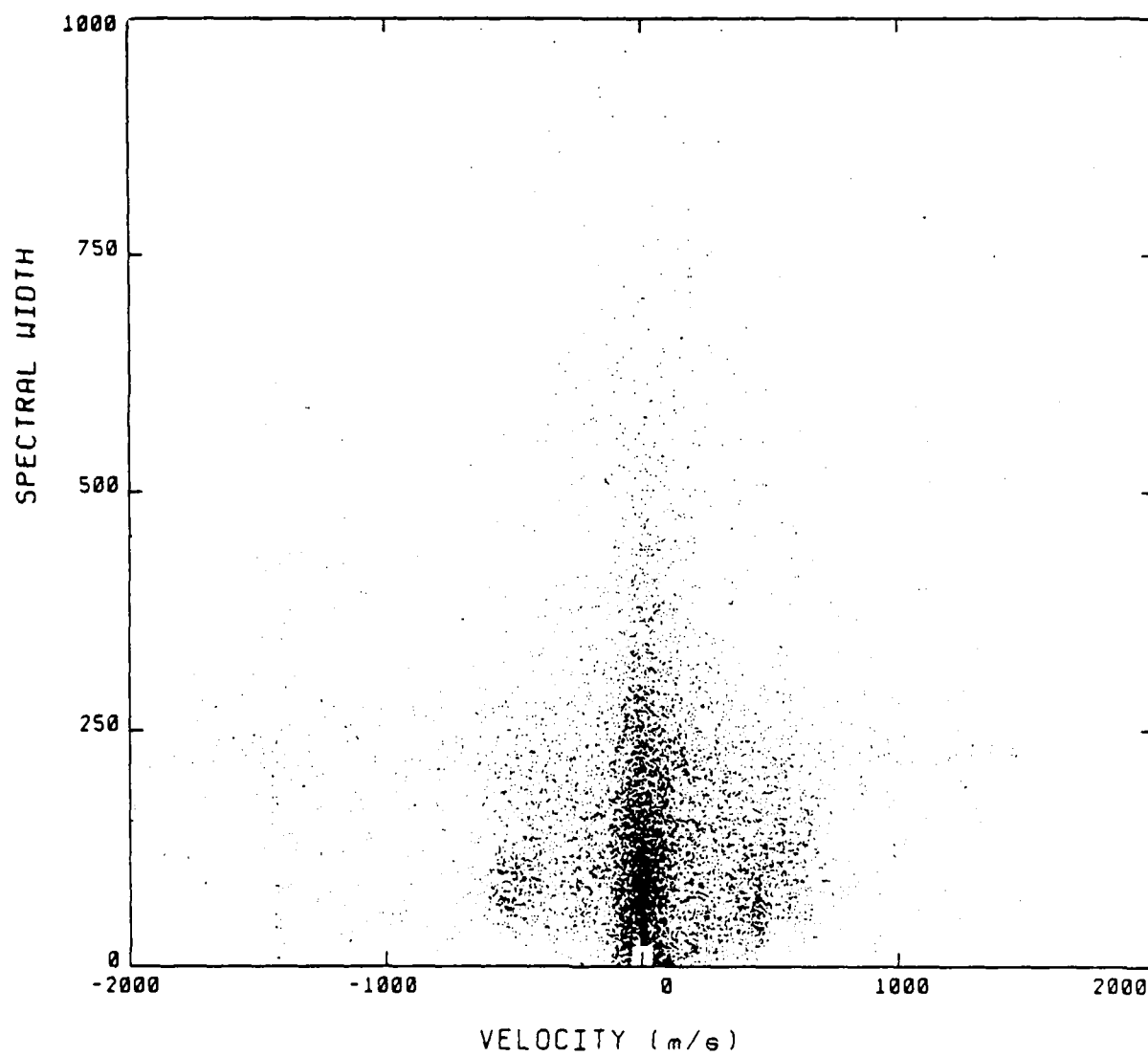
FIGURE 19a

SPECTRAL WIDTH VS VELOCITY
SNR > 0 dB. 900 - 2100 km
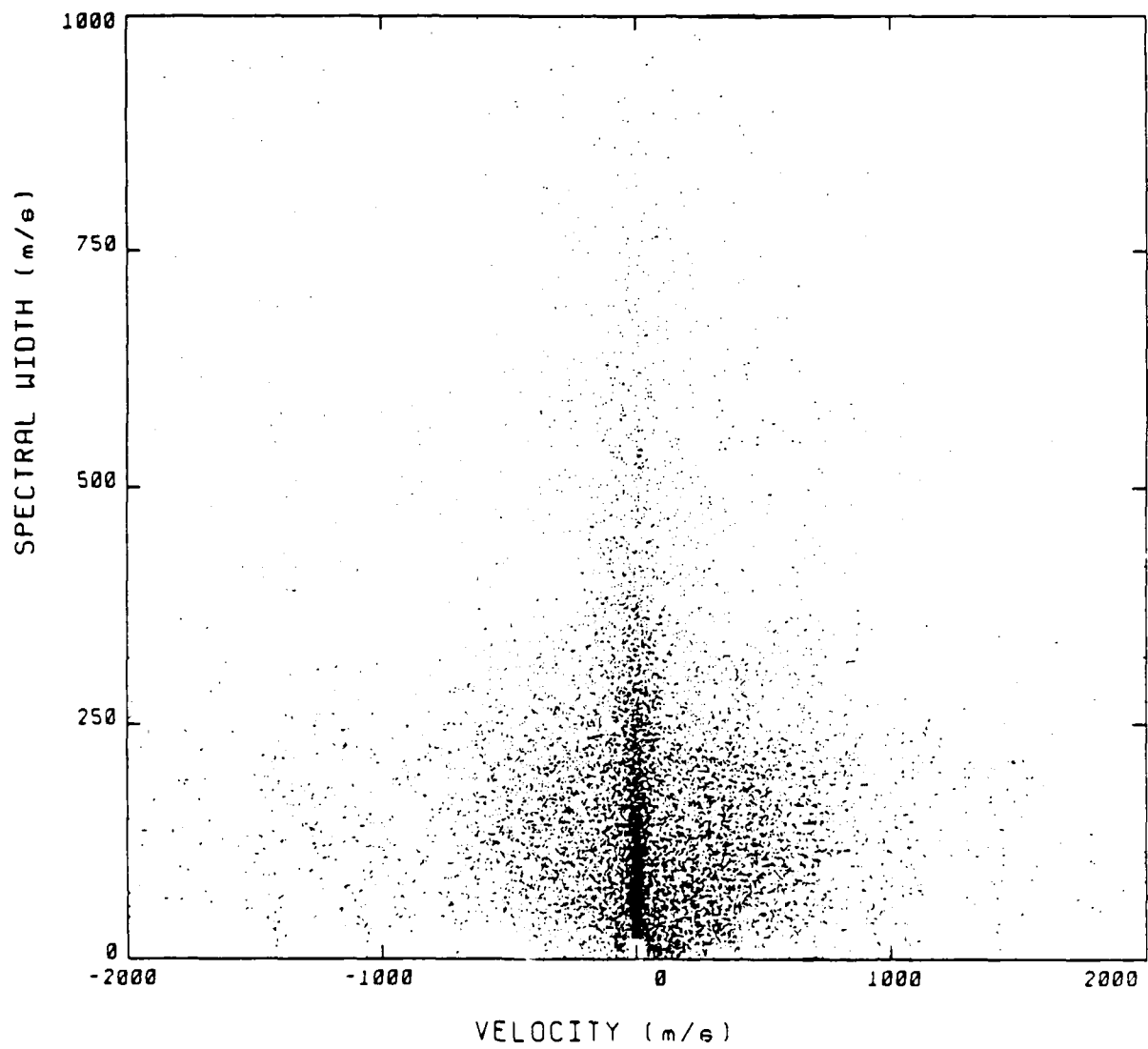
FIGURE 19b

SPECTRAL WIDTH VS RANGE
SNR > 6 dB. Verr<250 m/s. Kp < 2
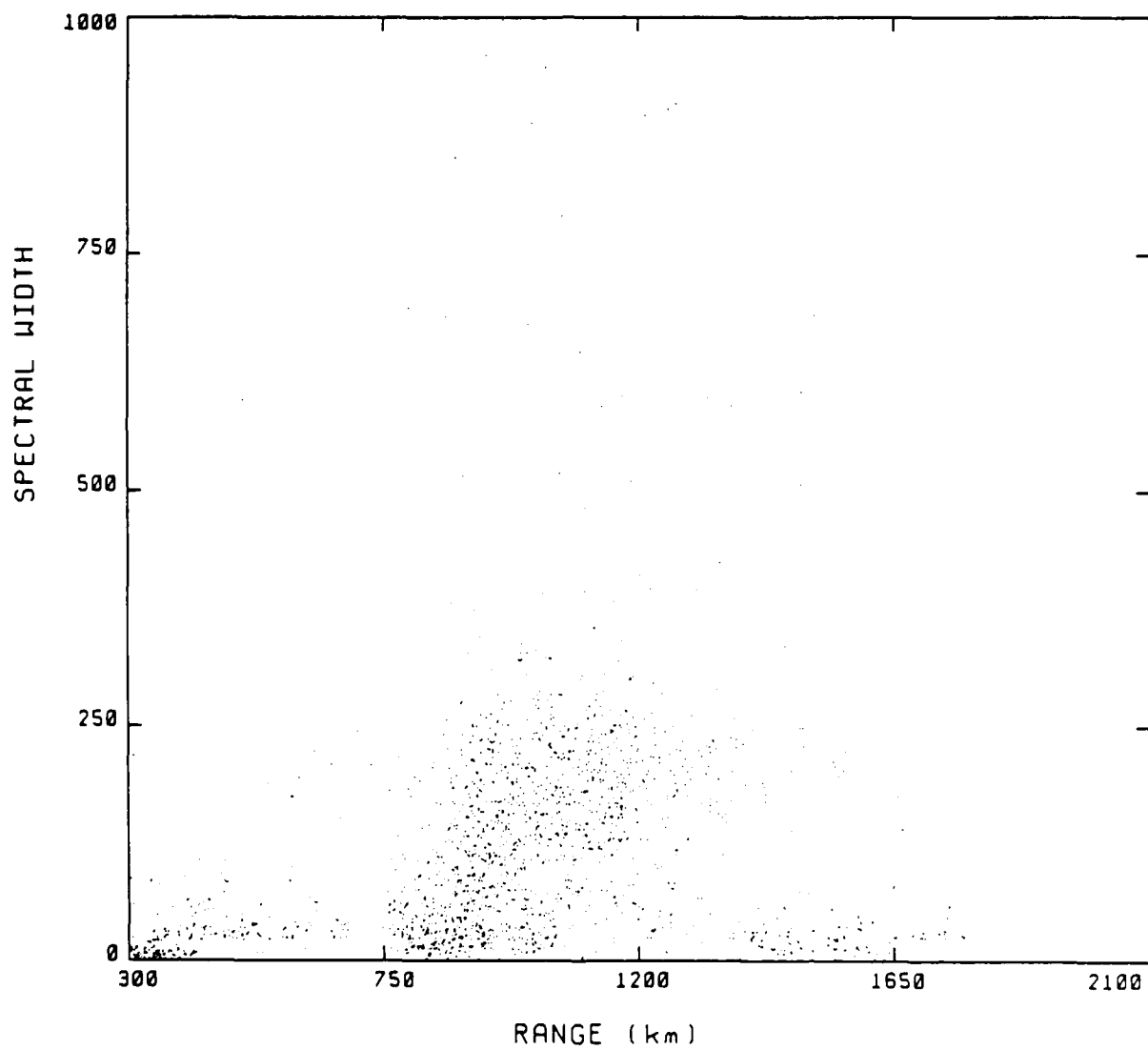
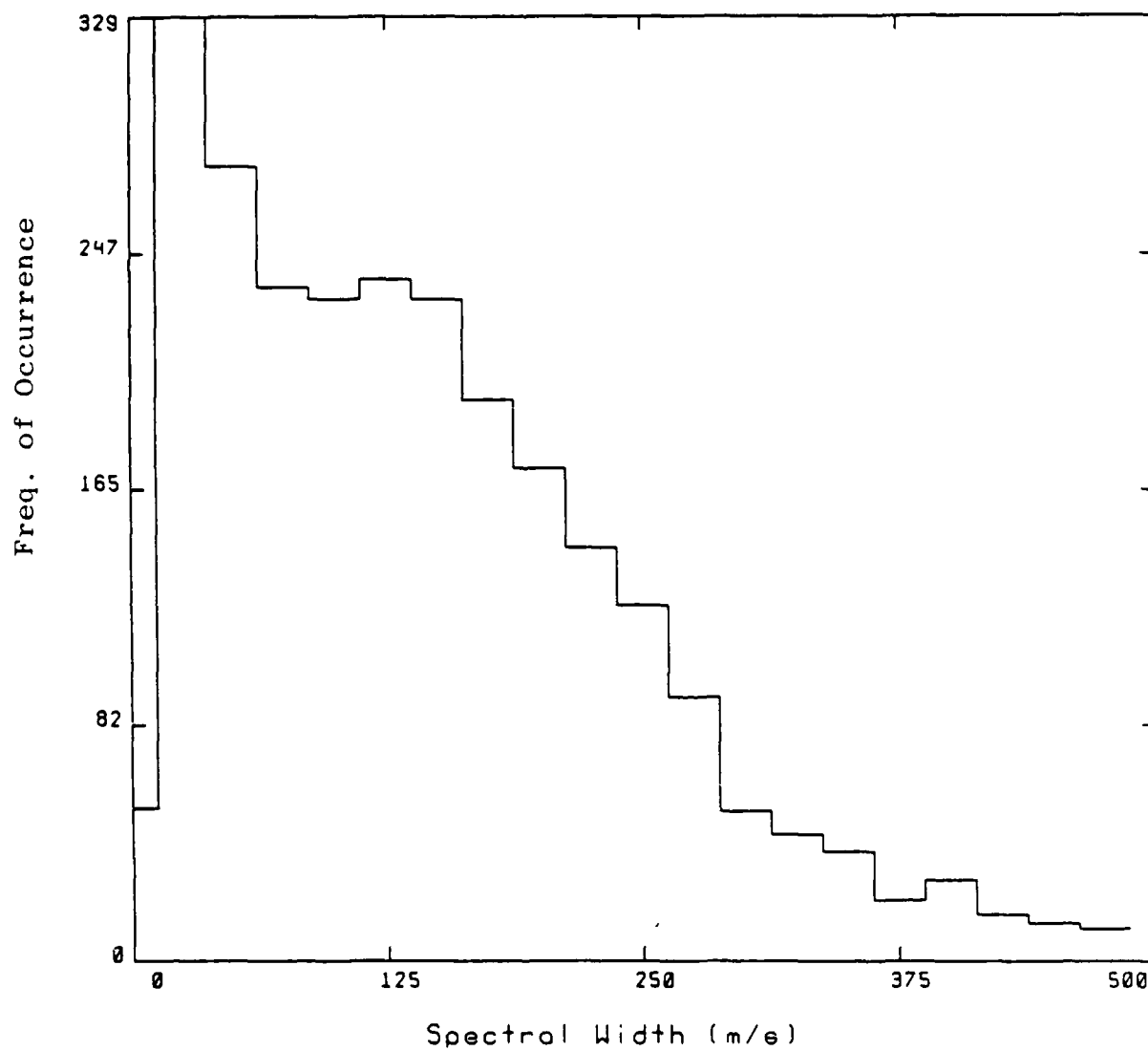FIGURE 20a

SPECTRAL WIDTH VS RANGE

SNR > 6 dB. Verr<250 m/s. Kp >- 4-
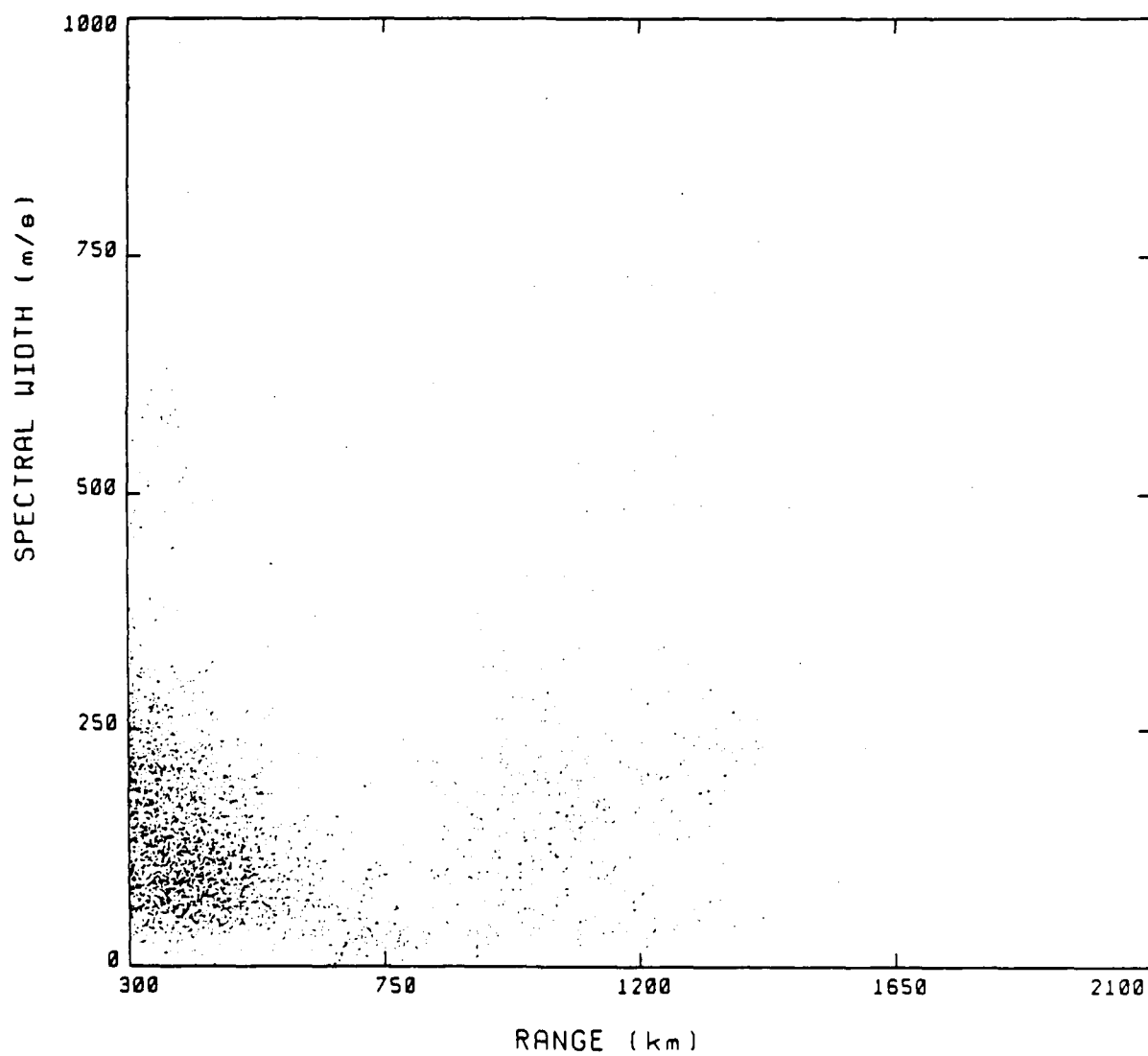
FIGURE 20b

SPECTRAL WIDTH DISTRIBUTION

SNR > 6 dB. Verr<250 m/s. Kp < 2-. 300-600 km
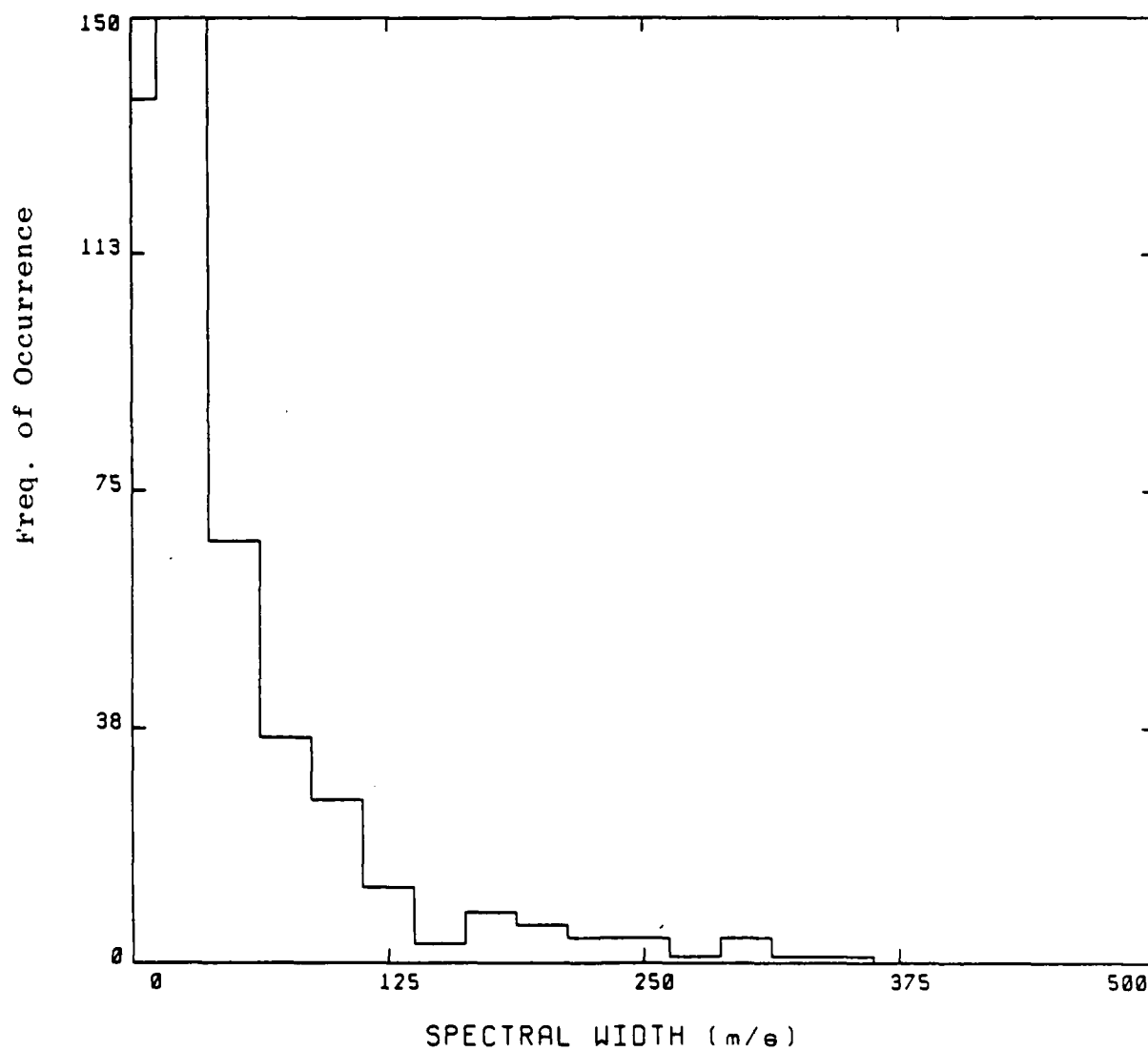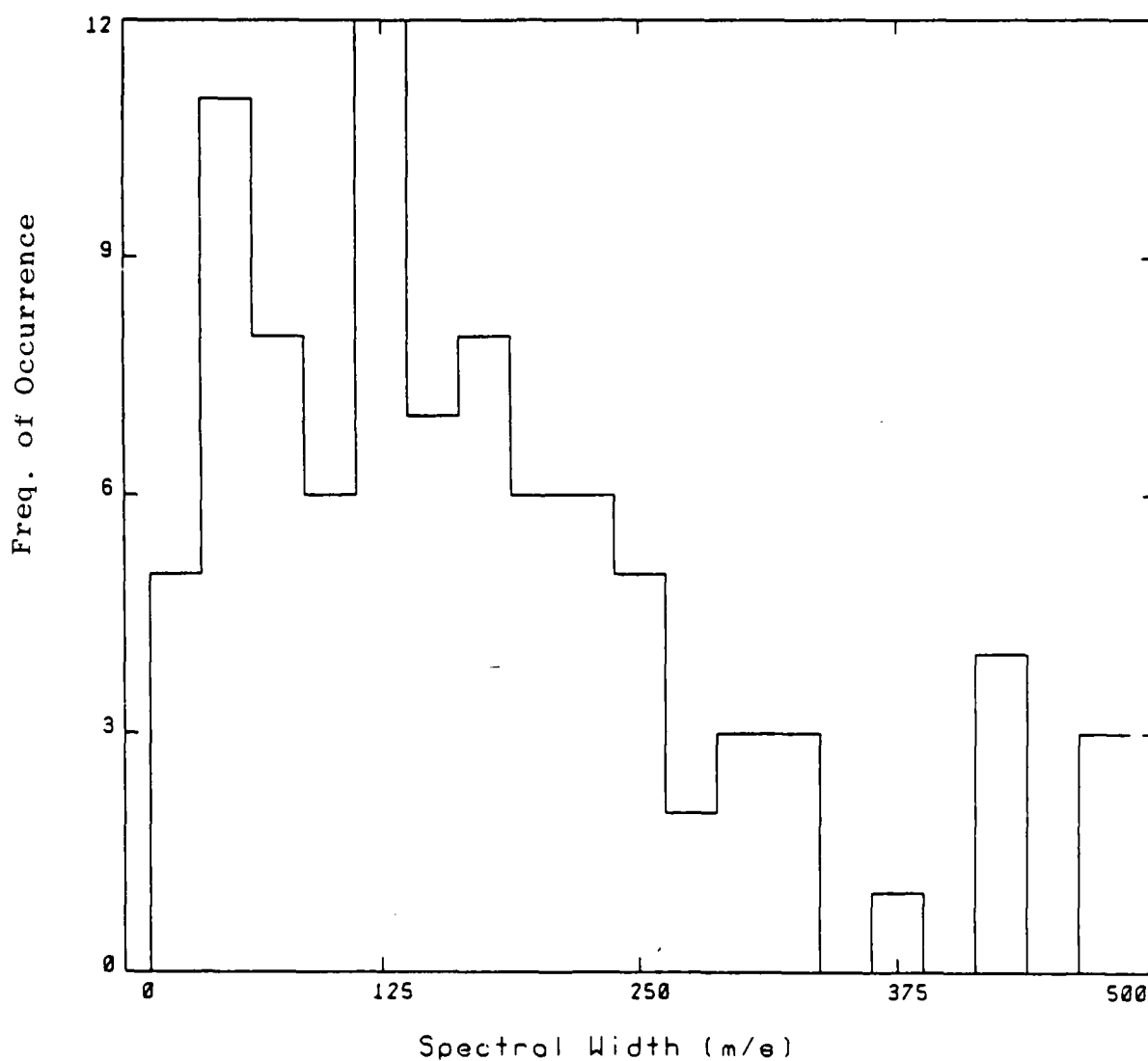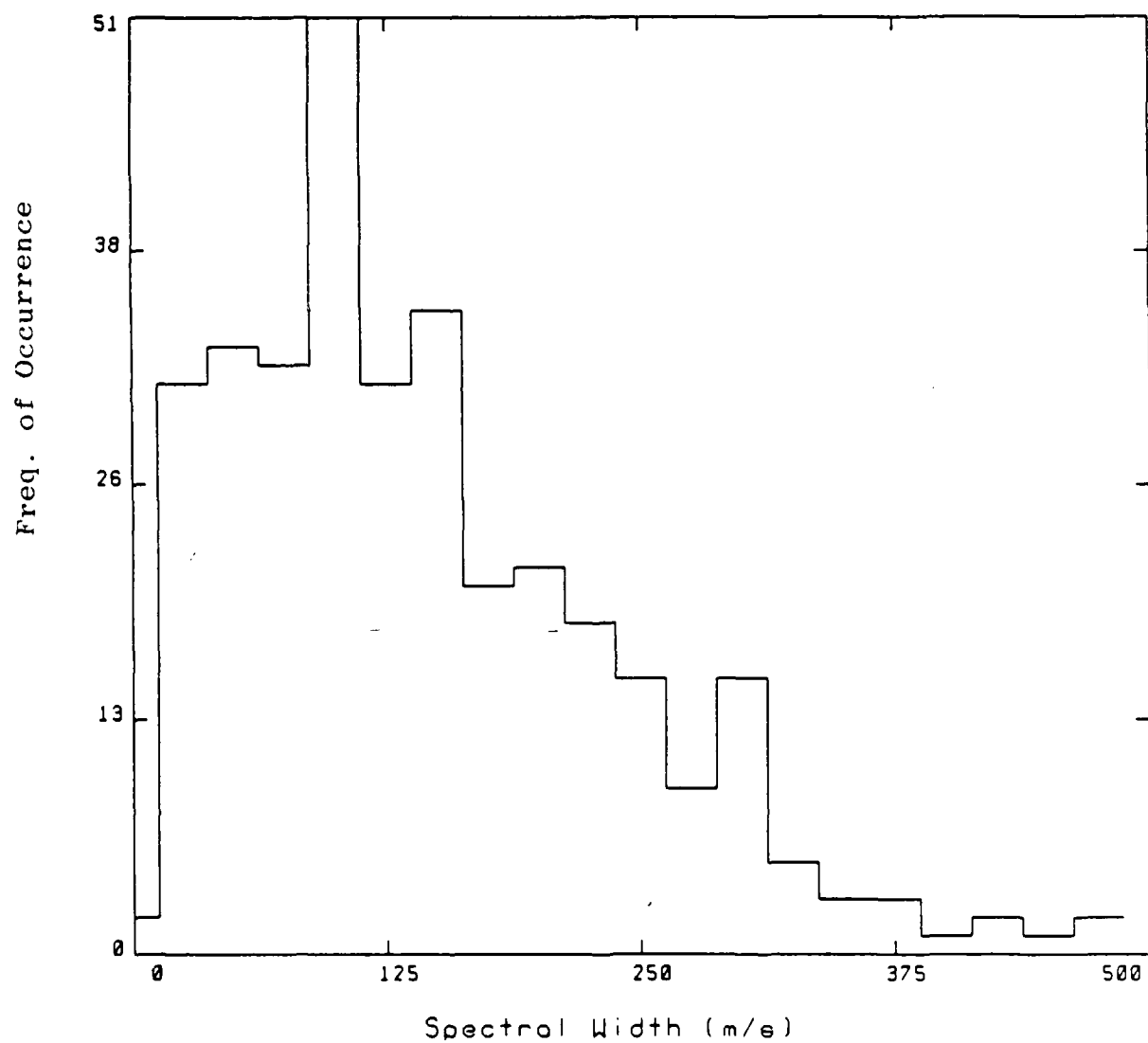

FIGURE 21a

SPECTRAL WIDTH DISTRIBUTION
SNR > 6 dB. Verr<250 m/s. Kp >= 4-. 300-600 km
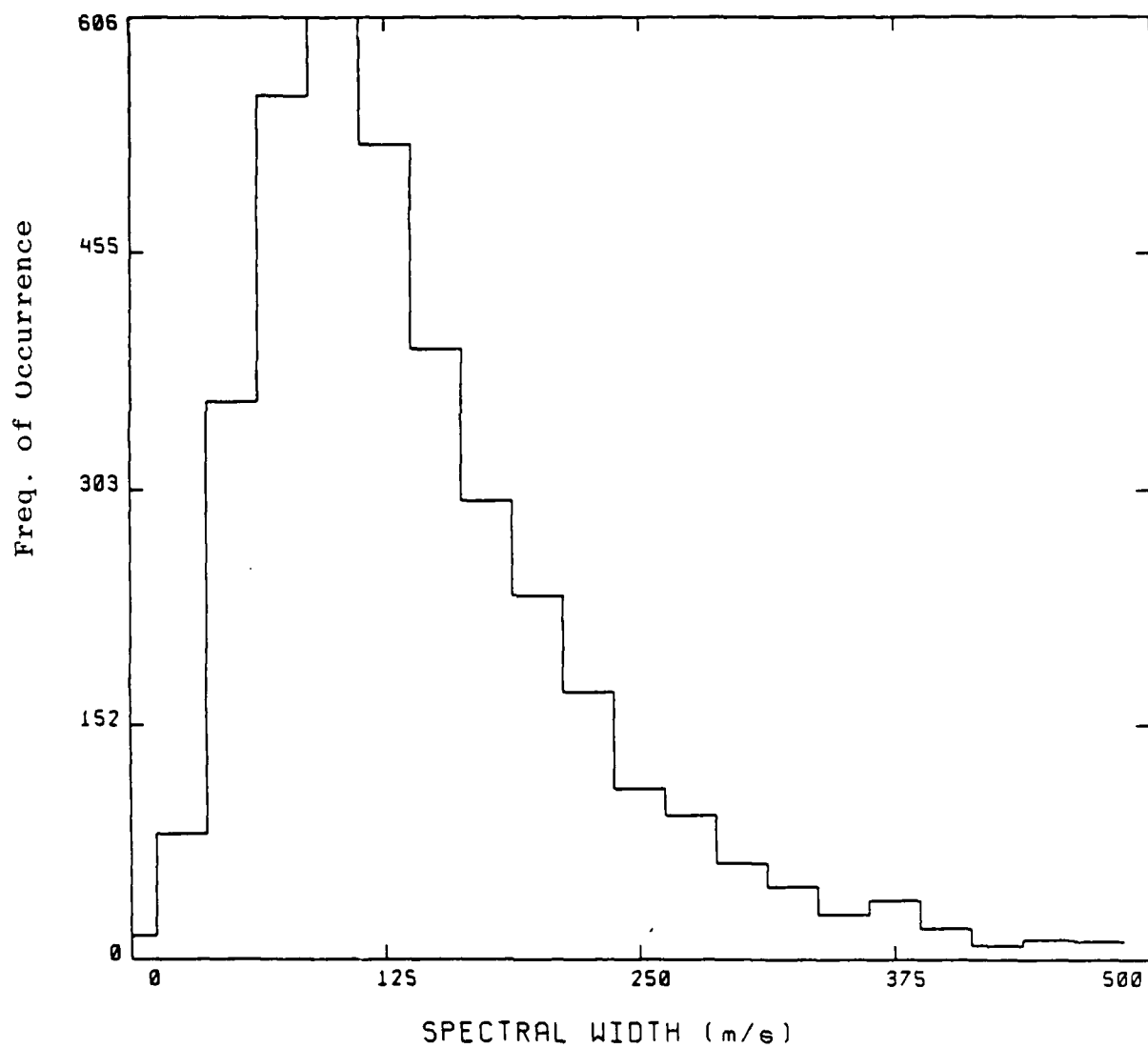
SPECTRAL WIDTH (m/s)

FIGURE 21b

SPECTRAL WIDTH DISTRIBUTION
SNR > 6 dB. Verr<250 m/s. Kp < 2-. 900-2100 km
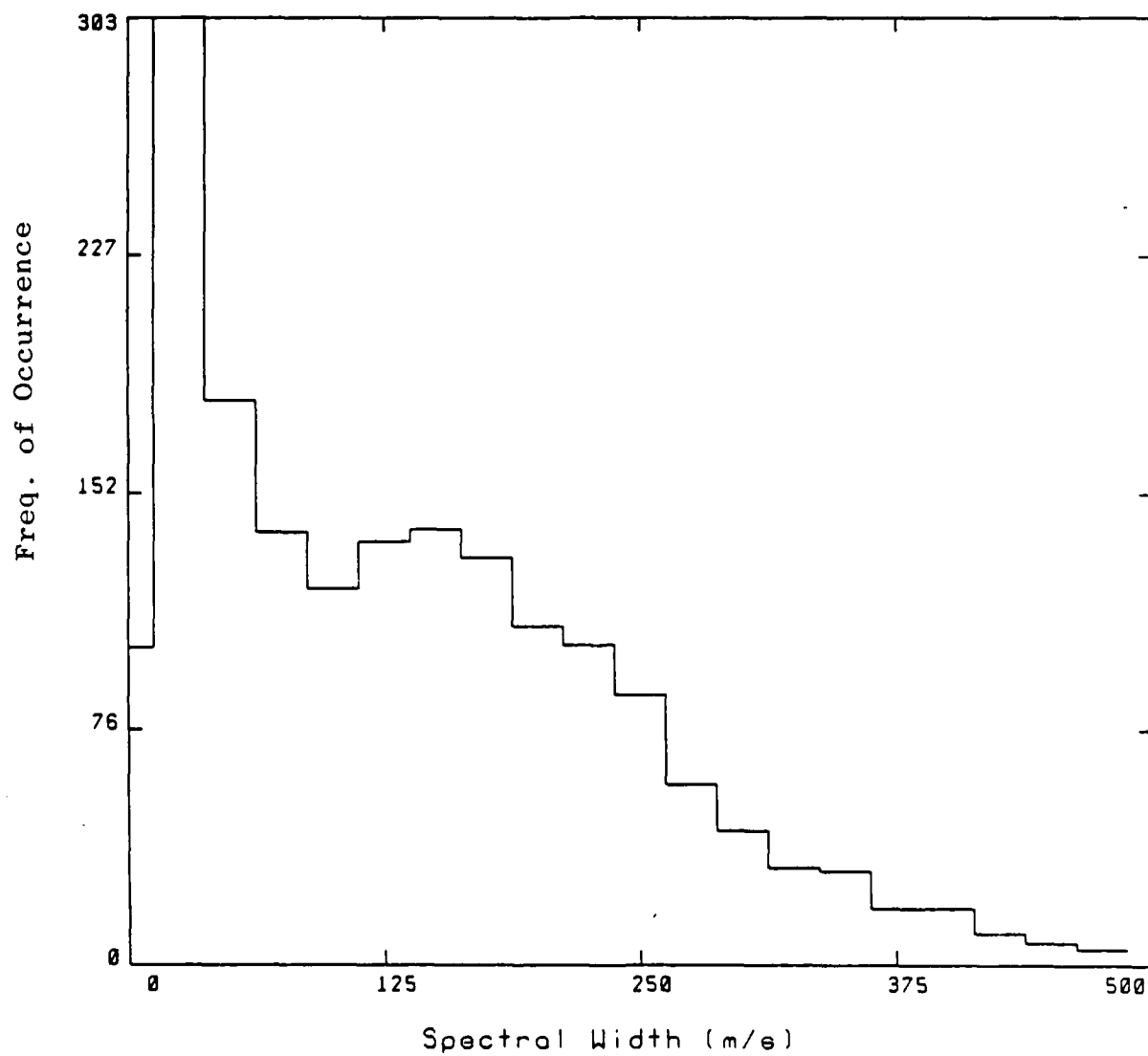
FIGURE 21c

SPECTRAL WIDTH DISTRIBUTION

SNR > 6 dB. Verr<250 m/s. Kp >= 4-. 900-2100 km
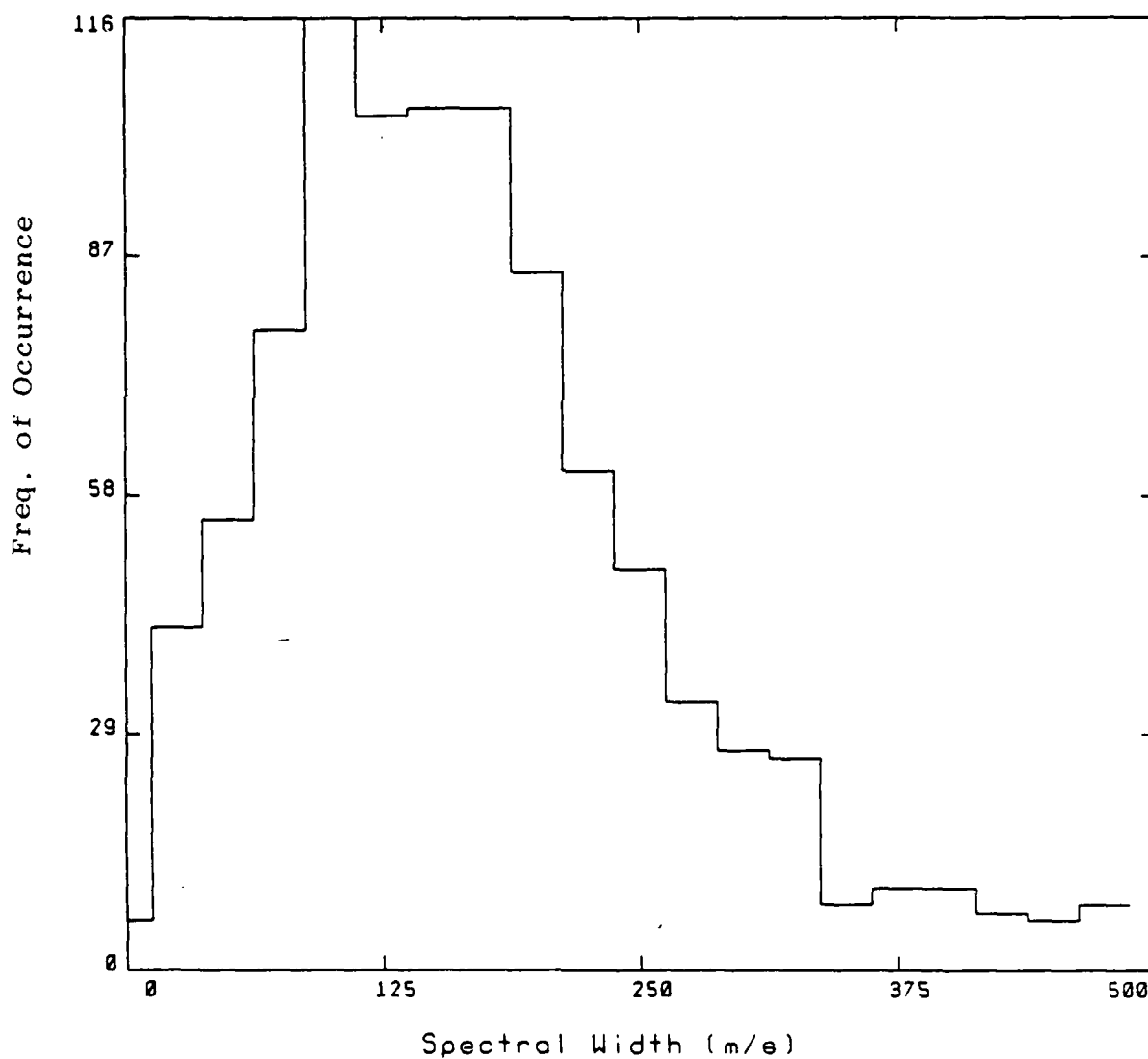
FIGURE 21d

SPECTRAL WIDTH DISTRIBUTION
SNR > 6 dB. Verr < 250 m/s. 300-600 km. 0-6 UT
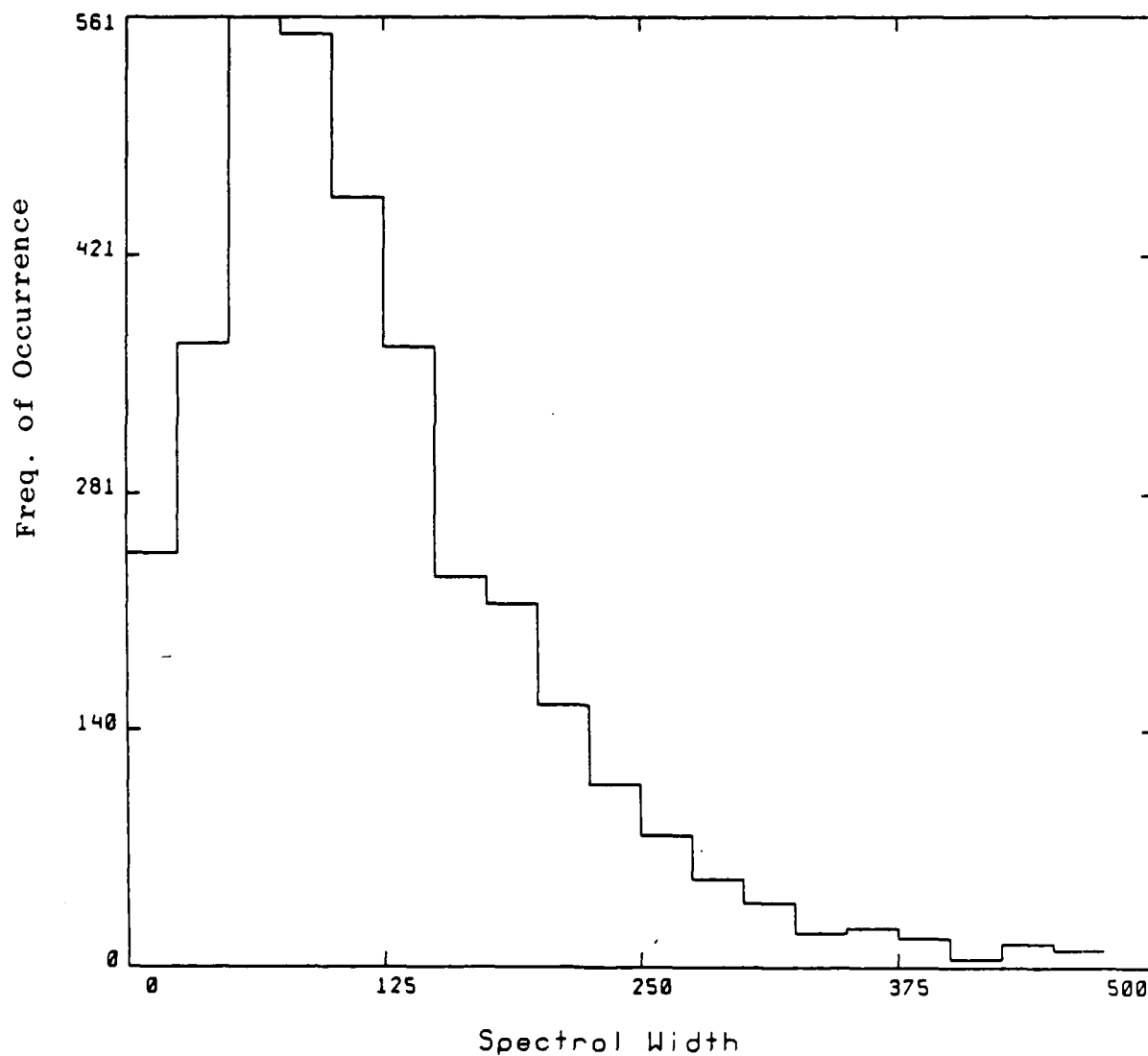
FIGURE 22a

SPECTRAL WIDTH DISTRIBUTION

SNR > 6 dB. Verr < 250 m/s. 300-600 km. 6-12 UT
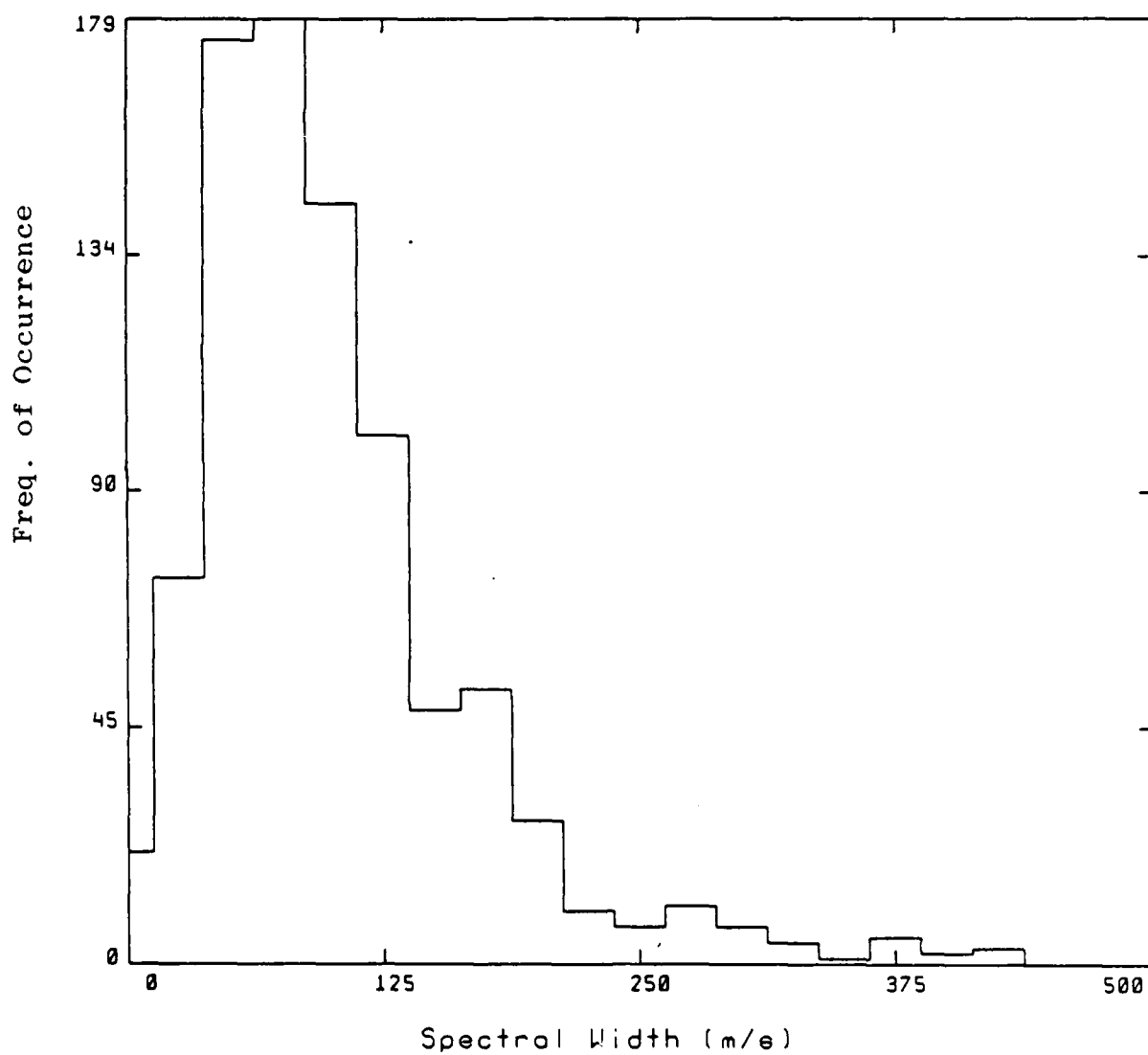
FIGURE 22b

SPECTRAL WIDTH DISTRIBUTION
SNR > 6 dB. Verr<250 m/s. 300-600 km. 12-18 UT
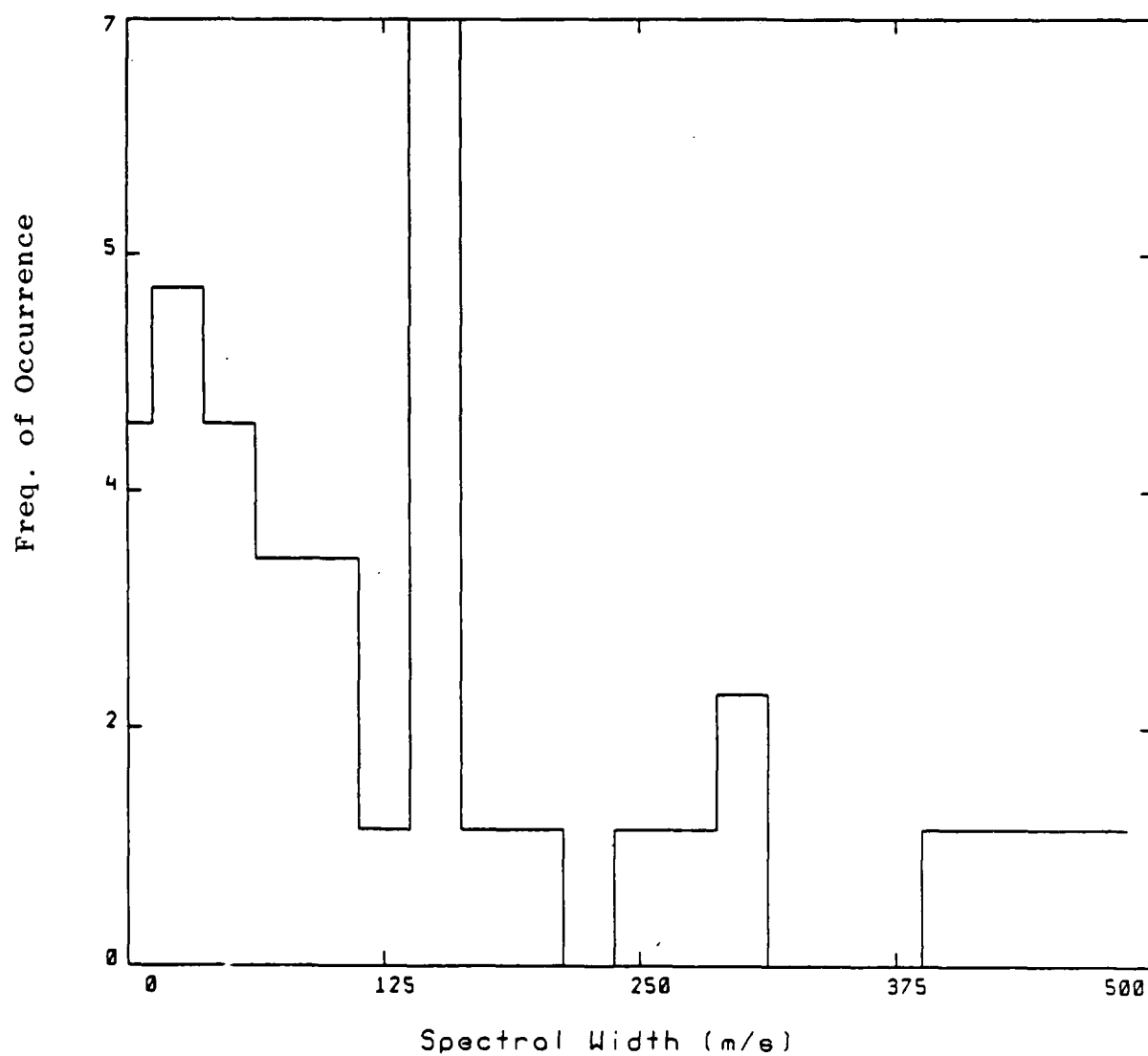
FIGURE 22c

SPECTRAL WIDTH DISTRIBUTION
SNR > 6 dB. Verr<250 m/s. 300-600 km. 18-24 UT
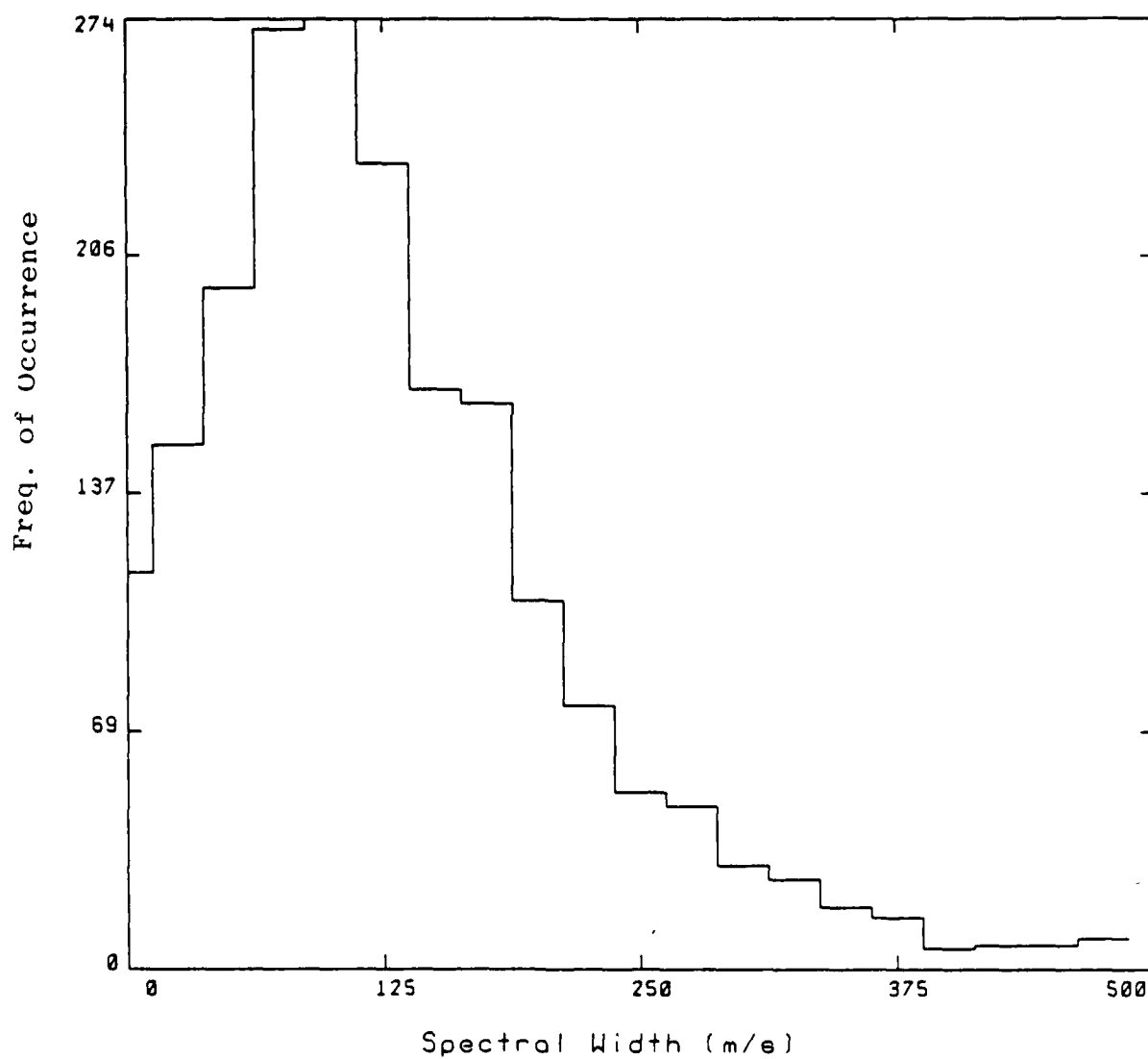
Spectral Width (m/s)

FIGURE 22d

SPECTRAL WIDTH DISTRIBUTION
SNR > 6 dB. Verr < 250 m/s. 900-2100 km. 0-6 UT

FIGURE 23a

SPECTRAL WIDTH DISTRIBUTION
SNR > 6 dB. Verr<250 m/s. 900-2100 km. 6-12 UT

FIGURE 23b

SPECTRAL WIDTH DISTRIBUTION
SNR > 6 dB. Verr<250 m/s. 900-2100 km. 12-18 UT

Spectral Width (m/s)
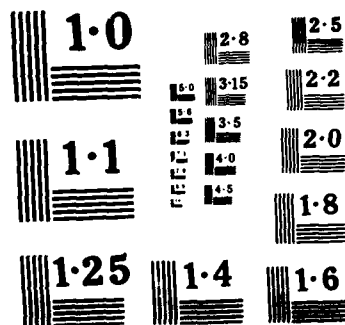
FIGURE 23c

SPECTRAL WIDTH DISTRIBUTION
SNR > 6 dB. Verr<250 m/s. 900-2100 km. 18-24 UT
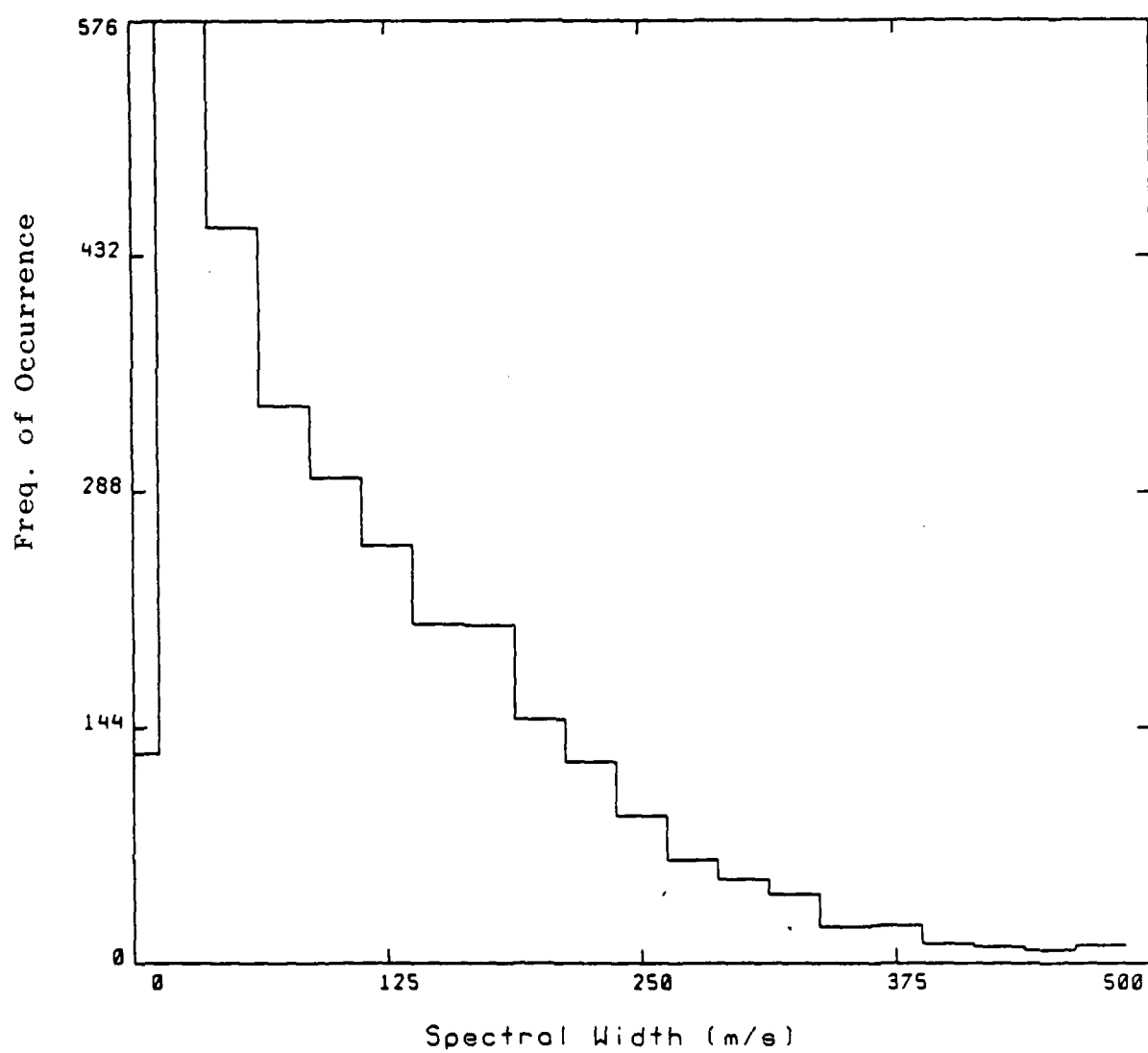
Spectral Width (m/s)

FIGURE 23d

SPECTRAL WIDTH DISTRIBUTION
SNR>6. Verr<250. Kp<2-. 900-2100 km. 18-24 UT
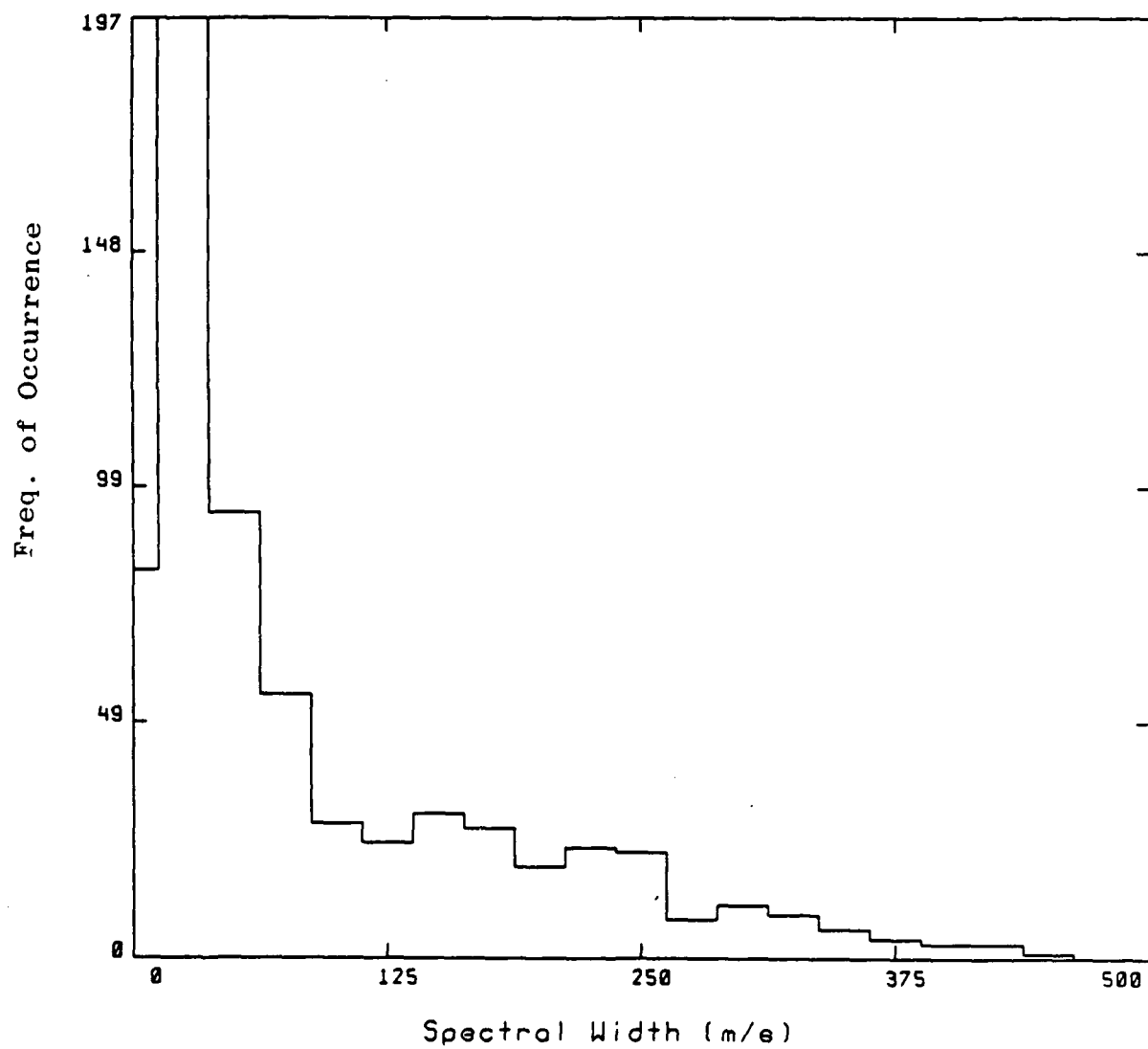
Spectral Width (m/s)

FIGURE 24a

SPECTRAL WIDTH DISTRIBUTION

SNR>6. Verr<250. Kp>=4-. 900-2100. 18-24 UT
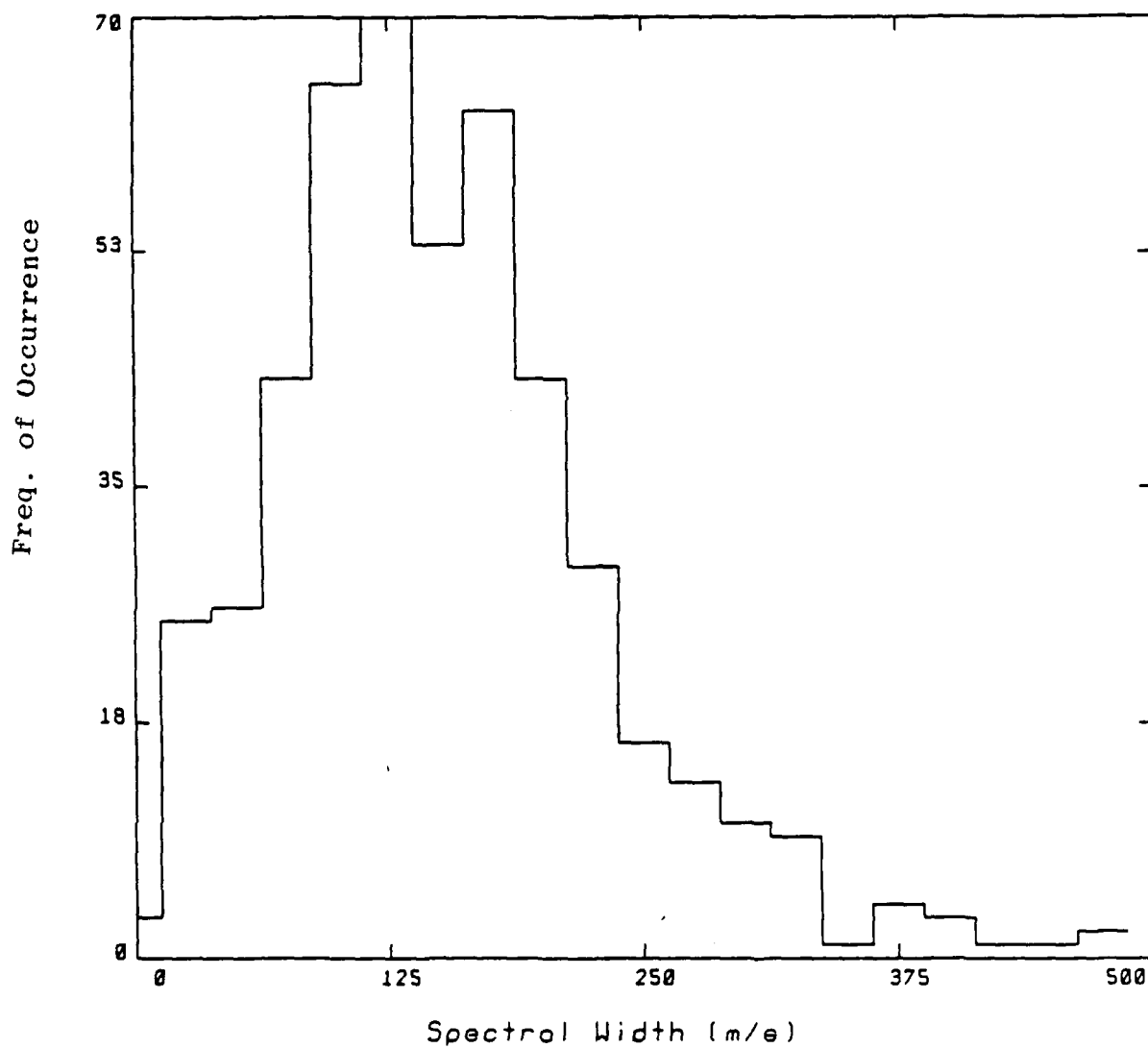

Spectral Width (m/e)

FIGURE 24b

MISSION
of
Rome Air Development Center

RADC plans and executes research, development, test and selected
acquisition programs in support of Command, Control, Communications
and Intelligence (C^3I) activities. Technical and engineering support within
areas of competence is provided to ESD Program Offices (POs) and other
ESD elements to perform effective acquisition of C^3I systems. The areas
of technical competence include communications, command and control,
battle management, information processing, surveillance sensors,
intelligence data collection and handling, solid state sciences,
electromagnetics, and propagation, and electronic, maintainability, and
compatibility.